



State of Wyoming
**Department of
Transportation**



U.S. Department
of Transportation
**Federal Highway
Administration**

FINAL REPORT

FHWA-WY-10/02F



REDUCTION OF WIND-INDUCED VIBRATIONS IN HIGH-MAST LIGHT POLES

By:

Emily B. Ahearn

Jay A. Puckett

Department of Civil and Architectural Engineering

University of Wyoming

1000 East University Avenue, Dept. 3295

Laramie, WY 82071

April 2010

NOTICE

This document is disseminated under the sponsorship of the U.S. Department of Transportation in the interest of information exchange. The U.S. Government assumes no liability for the use of the information contained in this document. The contents of this report reflect the views of the author(s) who are responsible for the facts and accuracy of the data presented herein. The contents do not necessarily reflect the official views or policies of the Wyoming Department of Transportation or the Federal Highway Administration. This report does not constitute a standard, specification, or regulation. The United States Government and the State of Wyoming do not endorse products or manufacturers. Trademarks or manufacturers' names appear in this report only because they are considered essential to the objectives of the document.

QUALITY ASSURANCE STATEMENT

The Federal Highway Administration (FHWA) provides high-quality information to serve Government, industry, and the public in a manner that promotes public understanding. Standards and policies are used to ensure and maximize the quality, objectivity, utility, and integrity of its information. FHWA periodically reviews quality issues and adjusts its programs and processes to ensure continuous quality improvement.

| | | | |
|---|--|---|------------------------------|
| Report No. FHWA-WY-10/02F | Government Accession No. | Recipients Catalog No. | |
| Title and Subtitle REDUCTION OF WIND-INDUCED VIBRATIONS IN HIGH-MAST LIGHT POLES | | Report Date April 2010 | Performing Organization Code |
| Author(s) Emily B. Ahearn; Jay Puckett | | Performing Organization Report No. | |
| Performing Organization Name and Address Department of Civil and Architectural Engineering University of Wyoming 1000 East University Avenue, Dept. 3295 Laramie, Wyoming 82071 | | Work Unit No. RS01(210) Job No. RS01210 | Contact or Grant No. |
| Sponsoring Agency Name and Address Wyoming Department of Transportation 5300 Bishop Blvd. Cheyenne, WY 82009-3340 Planning - Research Unit (307) 777-4182 | | Type of Report Final | Sponsoring Agency Code |
| Supplementary Notes WYDOT Technical Contact: Gregg Fredrick, P.E., Asst. Chief Engineer, Planning and Engineering | | | |
| <p>Abstract High-mast light poles are frequently used in areas where widespread illumination is required, such as along interstates and at major highway interchanges. The structures' heights are large relative to their cross-sectional dimensions, and, consequently, they are flexible and sensitive to wind loading. A number of failures of high-mast structures have occurred due to fatigue cracking. These failures have been linked to buffeting and vortex shedding loads.</p> <p>The primary study objective is to characterize the dynamic effects of wind-induced vibrations on high-mast structures in Laramie, WY, and to propose several retrofits that increase the aerodynamic damping, thereby reducing vibrations. A 120-ft tall high-mast pole was monitored to determine its dynamic characteristics. The pole was then retrofitted with helical strakes, ribbon dampers, a perforated shroud, and surface roughness, and the difference in the dynamic response of the retrofitted and unretrofitted pole under similar wind conditions was examined. The perforated shroud covering approximately 13% of the pole prevented lock-in under the wind conditions tested.</p> <p>A second pole was monitored and exhibited a drastically different response. It was observed that traffic vibrations exciting the pole at higher frequencies prevented lock-in from occurring. This phenomenon has not previously been observed as reported in the literature.</p> | | | |
| Key Words: Wyoming, vibrations, wind induced vibrations, high-mast poles, retrofit, buffeting, helical strakes, ribbon damper, perforated shroud. | | Distribution Statement Unlimited | |
| Security Classif. (of this report) Unclassified | Security Classif. (of this page) Unclassified | No. of Pages 118 | Price |

Form DOT F 1700.7 (8-72) Reproduction of form and completed page is authorized.

SI* (Modern Metric) Conversion Factors

| Approximate Conversions from SI Units | | | Approximate Conversions to SI Units | | |
|---------------------------------------|------------------------|-------------|-------------------------------------|-----------------------------|-------------------------|
| Symbol | When You Know | Multiply By | Symbol | When You Know | Multiply By |
| Length | | | | | |
| mm | millimeters | 0.039 | in | inches | 25.4 |
| m | meters | 3.28 | ft | feet | 0.305 |
| m | meters | 1.09 | yd | yards | 0.914 |
| km | kilometers | 0.621 | mi | miles | 1.61 |
| Area | | | | | |
| mm ² | square millimeters | 0.0016 | in ² | square inches | 645.2 |
| m ² | square meters | 10.764 | ft ² | square feet | 0.093 |
| m ² | square meters | 1.195 | yd ² | square yards | 0.836 |
| ha | hectares | 2.47 | ac | acres | 0.405 |
| km ² | square kilometers | 0.386 | mi ² | square miles | 2.59 |
| Volume | | | | | |
| ml | milliliters | 0.034 | fl oz | fluid ounces | 29.57 |
| l | liters | 0.264 | gal | gallons | 3.785 |
| m ³ | cubic meters | 35.71 | ft ³ | cubic feet | 0.028 |
| m ³ | cubic meters | 1.307 | yd ³ | cubic yards | 0.765 |
| Mass | | | | | |
| g | grams | 0.035 | oz | ounces | 28.35 |
| kg | kilograms | 2.202 | lb | pounds | 0.454 |
| Mg | megagrams | 1.103 | T | short tons (2000 lbs) | 0.907 |
| Temperature (exact) | | | | | |
| °C | Centigrade temperature | 1.8 C + 32 | °F | Fahrenheit temperature | 5(F-32)/9 or (F-32)/1.8 |
| Illumination | | | | | |
| lx | lux | 0.0929 | fc | foot-candles | 10.76 |
| cd/m ² | candela/m ² | 0.2919 | fl | foot-Lamberts | 3.426 |
| Force and Pressure or Stress | | | | | |
| N | newtons | 0.225 | lbf | pound-force | 4.45 |
| kPa | kilopascals | 0.145 | psi | pound-force per square inch | 6.89 |

ACKNOWLEDGMENTS

We would like to thank WYDOT and the Research Advisory Committee for providing the funding that allowed us to complete this project. Thanks also go to the WYDOT field crew, and especially Heath Sybert, for allowing us access to the poles and for their ongoing support with the installation of instrumentation and retrofits, without which this project would not have been possible.

This page is intentionally blank

EXECUTIVE SUMMARY

High-mast light poles are frequently used in areas where widespread illumination is required, such as along interstates and at major highway interchanges. The structures' heights are large relative to their cross-sectional dimensions, and, consequently, they are flexible and sensitive to wind loading. Fatigue cracking of high-mast structures has been reported, and a number of failures have occurred. Cracking has been linked to buffeting and vortex shedding loads.

Buffeting, or the effect of natural wind gusts, is the alongwind response of the structure. Buffeting is caused by velocity fluctuations that cause unsteady loading and is not self-induced. Loads due to natural wind gusts increase as the wind velocity increases.

Vortex shedding is the crosswind response of the high-mast. It occurs when the wind flows around the pole and separate vs, forming low pressure vortices on the leeward side. When a vortex forms, it reduces the pressure on one side and causes the structure to move towards it. As the flow continues, the vortices alternate sides causing the pole to move back and forth transverse to the wind direction. When this harmonic force and associated motion approaches the natural frequency of the structure, resonance may occur, which causes significant deflections and stresses. This phenomenon, referred to as "lock-in", only occurs in a small range of wind speeds.

The primary study objective is to characterize the dynamic effects of wind-induced vibrations on high-mast structures in Laramie, WY and to propose several retrofits that increase the aerodynamic damping, thereby reducing vibrations.

A 120-ft tall high-mast pole (Pole 3) was monitored to determine its dynamic characteristics. Accelerations, strains, and wind speed and direction were periodically collected. These data were used to determine the natural frequencies of the pole and the range of wind velocities that cause lock-in. The high-mast was also subjected to a pluck test to determine its damping. The pluck test data showed that Mode 3 is critical for the subject pole because it has the lowest damping ratio (0.1%). The pole data confirmed that Mode 3 is critical; out of 33 sets of data, twenty were found to contain one or more instances of Mode 3 lock-in at mean wind speeds of 10-19 mph. Lock-in in other modes was rarely observed, though data were collected over a large range of wind speeds.

A correlation between acceleration and stress range was developed for Pole 3. Where strain data are not available, the stress range (in ksi) at the base can be estimated by multiplying the peak acceleration at 56 ft (in g) by a factor of 7.3. According to this model, Mode 3 vibrations would cause the CAFL of 4.5 ksi to be reached when the acceleration at 56 ft was 0.6g and the maximum deflection (at 97 ft) was just 0.7 in.

The pole was then retrofitted with helical strakes, ribbon dampers, perforated shroud, and surface roughness, and the differences in the dynamic response of the retrofitted and unretrofitted pole under similar wind conditions were examined. Guidelines for designing each of the retrofits were used when available. The retrofits were selected for compatibility with the lowering device, ease of installation, and cost effectiveness.

While the other three retrofits were unsuccessful, the 16-ft long perforated shroud (covering 13% of the structure) prevented lock-in under the wind conditions tested. The shroud design could easily be modified to provide a practical retrofit by adding a short ramp section at

the top and bottom. The shroud itself is only separated from the pole by 1 in, and the lowering device would easily be able to pass over it with this simple modification.

A second pole (Pole 4) was monitored simultaneously and exhibited a drastically different response from the first, despite having identical geometry and similar surroundings, and being located only 550 ft away. While Pole 3 was locked in to Mode 3 and experiencing amplified accelerations up to 0.26g, Pole 4 was vibrating at frequencies characteristic of several different modes with a maximum acceleration of 0.05g. The only significant difference between the two structures is that Pole 3 is located in a field near a highway on-ramp, while Pole 4 is located 30 ft away from the westbound lane of I-80. It was hypothesized that traffic vibrations exciting Pole 4 at higher frequencies prevented lock-in from occurring. Additional data collected from the structure appeared to support the hypothesis. This phenomenon has not previously been observed as reported in the literature. It could inform future research on active damping devices for mitigating vortex-induced vibrations.

Further investigation is recommended to test the perforated shroud continuously in a larger range of wind speeds and to develop a shroud design that is compatible with the lowering device. Because surface roughness potentially offers a simple and elegant solution to the problem of vortex-induced vibration, further research is recommended to determine the amount of roughness required to eliminate vortex shedding.

TABLE OF CONTENTS

| | | |
|-------|--|----|
| 1 | Introduction | 1 |
| 1.1 | Background | 1 |
| 1.2 | Field Monitoring | 1 |
| 1.2.1 | Location | 1 |
| 1.2.2 | Instrumentation | 7 |
| 1.3 | Wind-Induced Vibrations | 17 |
| 1.3.1 | Buffeting | 18 |
| 1.3.2 | Vortex Shedding | 18 |
| 2 | Literature Review | 19 |
| 2.1 | Definitions | 19 |
| 2.1.1 | Bluff | 19 |
| 2.1.2 | Boundary Layer | 19 |
| 2.1.3 | Atmospheric Boundary Layer | 20 |
| 2.1.4 | Reynolds Number | 20 |
| 2.1.5 | Strouhal Number | 21 |
| 2.1.6 | Scruton Number | 22 |
| 2.1.7 | Critical Wind Velocity | 22 |
| 2.1.8 | Lock-in | 23 |
| 2.2 | Vortex-Induced Vibrations | 23 |
| 2.3 | Control of Vortex-Induced Vibrations | 24 |
| 2.4 | Traffic-Induced Vibrations | 25 |
| 2.5 | High-mast Lighting Structures | 25 |
| 2.5.1 | Iowa State University | 25 |
| 2.5.2 | Colorado State University | 27 |
| 2.6 | Damping Measurements | 27 |
| 2.7 | Aerodynamic Damping | 29 |
| 2.8 | Tuned-Mass Dampers (TMD) | 32 |
| 2.9 | Specifications | 33 |
| 2.9.1 | Vortex Shedding | 33 |
| 2.9.2 | Natural Wind Gusts | 35 |
| 3 | Theoretical Work | 36 |

| | | |
|-------|---|----|
| 3.1 | Modal Analysis | 36 |
| 3.1.1 | Mode Shapes | 36 |
| 3.1.2 | Natural Frequency | 37 |
| 3.2 | Critical Velocity | 37 |
| 3.3 | Important Dimensionless Variables | 38 |
| 3.3.1 | Reynolds Number | 38 |
| 3.3.2 | Strouhal Number | 39 |
| 3.3.3 | Scruton Number | 39 |
| 4 | Experimental Work | 40 |
| 4.1 | Data Analysis | 40 |
| 4.1.1 | Alongwind and Crosswind | 40 |
| 4.1.2 | Fast Fourier Transform | 40 |
| 4.1.3 | Prony Method | 41 |
| 4.2 | Deflection Calculations | 43 |
| 4.3 | Mode Shapes | 43 |
| 4.4 | Pluck Test | 44 |
| 4.5 | Traffic Vibrations | 45 |
| 4.5.1 | Ground Vibrations and Airborne Vibrations | 46 |
| 4.6 | Retrofits | 47 |
| 4.6.1 | Aerodynamic Dampers | 47 |
| 4.6.2 | Advantages and Disadvantages | 52 |
| 5 | Results | 53 |
| 5.1 | Dynamic Characteristics | 53 |
| 5.1.1 | Natural Frequencies | 53 |
| 5.1.2 | Damping Ratios | 54 |
| 5.2 | Unretrofitted Pole Behavior | 54 |
| 5.3 | Retrofits | 59 |
| 5.3.1 | Ribbons | 59 |
| 5.3.2 | Helical Strakes | 62 |
| 5.3.3 | Perforated Shroud | 67 |
| 5.3.4 | Surface Roughness | 72 |
| 5.4 | Summary | 76 |

| | | |
|-----|---|-----|
| 6 | Traffic Vibrations | 78 |
| 6.1 | Test 20 - Calm Conditions | 79 |
| 6.2 | Test 15 - Mode 2 | 84 |
| 6.3 | Test 27 - Mode 3 | 90 |
| 6.4 | Summary | 96 |
| 6.5 | Test 29 - Lateral Ground Vibrations | 96 |
| 6.6 | Sensor Event Driven Trigger..... | 100 |
| 7 | Conclusions | 101 |
| 7.1 | Findings..... | 101 |
| 7.2 | Suggested future work..... | 102 |
| 8 | References | 103 |

LIST OF FIGURES

| | |
|---|----|
| Figure 1. 120-ft, 16-sided high-mast light pole | 2 |
| Figure 2. High-mast light pole geometry from shop plans..... | 3 |
| Figure 3. High-mast structure locations | 4 |
| Figure 4. Two monitored high-mast light poles, (a) Pole 3 and (b) Pole 4 | 4 |
| Figure 5. Slip joint splice..... | 5 |
| Figure 6. Handhole detail | 5 |
| Figure 7. Lowering device..... | 6 |
| Figure 8. Ring assembly with centering system | 6 |
| Figure 9. Ring assembly and luminaire on pole | 7 |
| Figure 10. Instrumentation locations for preliminary testing..... | 8 |
| Figure 11. Orientation of G-Link accelerometers | 9 |
| Figure 12. Accelerometer locations relative to mode shapes | 9 |
| Figure 13. 7 dBi antenna (photo courtesy of L-com) | 10 |
| Figure 14. RF antenna patterns for 7 dBi antenna (diagram courtesy of L-com)..... | 10 |
| Figure 15. Micro-Measurements strain gauge..... | 11 |
| Figure 16. Detail of strain gauge locations..... | 11 |
| Figure 17. Propeller vane anemometer (photo courtesy of R.M. Young)..... | 12 |
| Figure 18. Anemometer mounted on high-mast pole..... | 12 |
| Figure 19. USB base station (photo courtesy of Microstrain)..... | 13 |
| Figure 20. 9 dBi antenna (diagram courtesy of L-com) | 13 |
| Figure 21. RF antenna patterns for 9 dBi antenna..... | 13 |
| Figure 22. Node Commander software..... | 14 |
| Figure 23. BDI mobile base station | 15 |
| Figure 24. BDI wireless transmitter and accelerometer | 15 |
| Figure 25. Locations of uniaxial BDI accelerometers for retrofit testing | 16 |
| Figure 26. WinSTS Data Acquisition Software | 16 |
| Figure 27. Instrumentation locations for retrofit testing..... | 17 |
| Figure 28. Photograph of a vortex street (Van Dyke, 1982) | 18 |
| Figure 29. Boundary layer with flow separation | 19 |
| Figure 30. A typical atmospheric boundary layer velocity profile..... | 20 |
| Figure 31. Regimes of fluid flow across smooth circular cylinders (Lienhard, 1966)..... | 21 |

| | |
|---|----|
| Figure 32. Evolution of vortex shedding frequency with wind velocity over elastic structure (Phares, Sarkar, Wipf, & Chang, 2007) | 23 |
| Figure 33. Disturbed airflow around a cylinder (Reid, 2008) | 24 |
| Figure 34. Pluck test scheme(Pagnini & Solari, 2001)..... | 28 |
| Figure 35. Helical strakes on stacks at the Mountain Cement Company in Laramie, WY | 29 |
| Figure 36. Perforated shroud (Kumar, Sohn, & Gowda, 2008)..... | 30 |
| Figure 37. Add-on devices: (a) helical strakes (b) spoiler plates (after Kumar, Sohn, & Gowda, 2008) | 30 |
| Figure 38. Smoothly curved protuberances (after Kumar, Sohn, & Gowda, 2008)..... | 31 |
| Figure 39. Ribbons (after Kumar, Sohn, & Gowda, 2008) | 32 |
| Figure 40. Mode shapes with luminaire mass | 37 |
| Figure 41. Transformation matrix equation..... | 40 |
| Figure 42. Transformation from NS, EW to AW, CW..... | 40 |
| Figure 43. FFT amplitude spectrum showing first four modal frequencies | 41 |
| Figure 44. FFT amplitude spectrum showing Mode 3 lock-in at 3.8 Hz | 41 |
| Figure 45. Sample Prony approximation of acceleration data..... | 43 |
| Figure 46. 41 ft Accelerations vs. 56 ft accelerations for Pole 3 in Mode 3 lock-in..... | 44 |
| Figure 47. Pluck test setup..... | 45 |
| Figure 48. Steel link..... | 45 |
| Figure 49. Truck traffic near Pole 4 | 46 |
| Figure 50. Ribbon retrofit on top 40 ft of high-mast pole | 48 |
| Figure 51. Helical strakes installed on high-mast pole..... | 49 |
| Figure 52. Perforated shroud installed on high-mast pole..... | 50 |
| Figure 53. Diamond-textured rubber material..... | 51 |
| Figure 54. Detail of surface roughness material..... | 51 |
| Figure 55. Surface roughness installed on high-mast pole..... | 52 |
| Figure 56. Pluck test acceleration data | 53 |
| Figure 57. Maximum acceleration vs. 30s mean wind speed..... | 55 |
| Figure 58. Average maximum crosswind acceleration vs. 30s mean wind speed..... | 55 |
| Figure 59. Wind speed vs. time | 57 |
| Figure 60. Wind direction vs. time | 57 |
| Figure 61. Acceleration vs. time at a mean wind speed of 18.7 mph (Node 464) | 58 |

| | |
|--|----|
| Figure 62. FFT of (a) crosswind and (b) alongwind accelerations at a mean wind speed of 18.7 mph | 59 |
| Figure 63. Wind speed vs. time | 60 |
| Figure 64. Wind direction vs. time | 60 |
| Figure 65. Acceleration vs. time at a mean wind speed of 11.9 mph (Node 467) | 61 |
| Figure 66. FFT of (a) crosswind and (b) alongwind accelerations at a mean wind speed of 11.9 mph | 62 |
| Figure 67. Maximum crosswind acceleration vs. 30s mean wind speed..... | 63 |
| Figure 68. Average maximum crosswind acceleration vs. 30s mean wind speed (helical strakes) | 63 |
| Figure 69. Wind speed vs. time | 64 |
| Figure 70. Wind direction vs. time | 64 |
| Figure 71. Acceleration vs. time at a mean wind speed of 12.8 mph (Node 464) | 65 |
| Figure 72. FFT of (a) crosswind and (b) alongwind accelerations at a mean wind speed of 12.8 mph | 66 |
| Figure 73. Stress vs. time at a mean wind speed of 12.8 mph..... | 66 |
| Figure 74. Maximum acceleration vs. stress range | 67 |
| Figure 75. Maximum crosswind acceleration vs. 30s mean wind speed..... | 68 |
| Figure 76. Wind speed vs. time | 69 |
| Figure 77. Wind direction vs. time | 69 |
| Figure 78. Acceleration vs. time at a mean wind speed of 18.7 mph (Node 464) | 70 |
| Figure 79. Comparison of wind speed records for unretrofitted pole and perforated shroud | 71 |
| Figure 80. Comparison of wind direction records for unretrofitted pole and perforated shroud .. | 71 |
| Figure 81. FFT of (a) crosswind and (b) alongwind accelerations at a mean wind speed of 18.7 mph | 72 |
| Figure 82. Maximum crosswind acceleration vs. 30s mean wind speed..... | 73 |
| Figure 83. Wind speed vs. time | 74 |
| Figure 84. Wind direction vs. time | 74 |
| Figure 85. Acceleration vs. time at a mean wind speed of 12.2 mph (Node 464) | 75 |
| Figure 86. FFT of (a) crosswind and (b) alongwind accelerations at a mean wind speed of 12.2 mph | 76 |
| Figure 87. Crosswind acceleration vs. time at 56 ft for Pole 3 and Pole 4..... | 78 |
| Figure 88. FFT analysis of (a) Pole 3 and (b) Pole 4 accelerations..... | 79 |
| Figure 91. Acceleration vs. time under calm conditions | 80 |
| Figure 92. FFT amplitude spectrum for NS accelerations under calm conditions | 80 |

| | |
|---|----|
| Figure 93. FFT amplitude spectrum for EW accelerations under calm conditions | 81 |
| Figure 94. FFT amplitude spectrum for vertical accelerations under calm conditions | 81 |
| Figure 95. Acceleration vs. time with natural wind (calm conditions) | 82 |
| Figure 96. FFT analysis of NS accelerations with natural wind (calm conditions) | 82 |
| Figure 97. FFT analysis of EW accelerations with natural wind (calm conditions) | 83 |
| Figure 98. Acceleration vs. time with traffic excitation | 83 |
| Figure 99. FFT analysis of NS accelerations with traffic excitation | 84 |
| Figure 100. FFT analysis of EW accelerations with traffic excitation | 84 |
| Figure 101. Acceleration vs. time at a mean wind speed of 7.1 mph | 85 |
| Figure 102. FFT amplitude spectrum for NS accelerations at a mean wind speed of 7.1 mph | 85 |
| Figure 103. FFT amplitude spectrum for EW accelerations at a mean wind speed of 7.1 mph | 86 |
| Figure 104. FFT amplitude spectrum for vertical accelerations at a mean wind speed of 7.1 mph | 86 |
| Figure 105. Acceleration vs. time at near-constant wind speed close to Mode 2 critical velocity | 87 |
| Figure 106. Acceleration vs. time with natural wind (near Mode 2 critical velocity) | 88 |
| Figure 107. FFT analysis of NS accelerations with natural wind (near Mode 2 critical velocity) | 88 |
| Figure 108. FFT analysis of EW accelerations with natural wind (near Mode 2 critical velocity) | 89 |
| Figure 109. Acceleration vs. time with traffic excitation | 89 |
| Figure 110. FFT analysis of NS accelerations with traffic excitation | 90 |
| Figure 111. FFT analysis of EW accelerations with traffic excitation | 90 |
| Figure 112. Acceleration vs. time at a mean wind speed of 12.1 mph | 91 |
| Figure 113. FFT amplitude spectrum for NS accelerations at a mean wind speed of 12.1 mph | 91 |
| Figure 114. FFT amplitude spectrum for EW accelerations at a mean wind speed of 12.1 mph | 92 |
| Figure 115. FFT amplitude spectrum for vertical accelerations at a mean wind speed of 12.1 mph | 92 |
| Figure 116. Acceleration vs. time at constant wind speed close to Mode 3 critical velocity | 93 |
| Figure 117. Acceleration vs. time with natural wind (near Mode 3 critical velocity) | 93 |
| Figure 118. FFT analysis of NS accelerations with natural wind (near Mode 3 critical velocity) | 94 |
| Figure 119. FFT analysis of EW accelerations with natural wind (near Mode 3 critical velocity) | 94 |
| Figure 120. Acceleration vs. time with traffic excitation | 95 |
| Figure 121. FFT analysis of NS accelerations with traffic excitation | 95 |
| Figure 122. FFT analysis of EW accelerations with traffic excitation | 96 |
| Figure 123. Acceleration vs. time | 97 |
| Figure 124. Acceleration vs. time (Truck 1) | 98 |

| | |
|--|-----|
| Figure 125. FFT analysis of NS accelerations (Truck 1) | 98 |
| Figure 126. FFT analysis of ground accelerations (Truck 1) | 99 |
| Figure 127. Acceleration vs. time (Truck 2) | 99 |
| Figure 128. FFT analysis of NS accelerations (Truck 2) | 100 |
| Figure 129. FFT analysis of ground accelerations (Truck 2) | 100 |

LIST OF TABLES

| | |
|--|----|
| Table 1. Pole geometry from shop plans | 3 |
| Table 2. Drilled shaft specifications | 7 |
| Table 3. Iowa pole response data..... | 26 |
| Table 4. Iowa pole damping data..... | 26 |
| Table 5. Genova pole response data | 28 |
| Table 6. Importance factors for fatigue design (Dexter & Ricker, 2002) | 34 |
| Table 7. Values from SAP2000 | 37 |
| Table 8. Critical velocities..... | 38 |
| Table 9. Reynolds numbers for high-mast poles at critical diameter | 38 |
| Table 10. Retrofit costs..... | 47 |
| Table 11. Perforated shroud specifications..... | 50 |
| Table 12. Natural frequencies..... | 53 |
| Table 13. Damping ratios | 54 |
| Table 14 Maximum accelerations and deflections | 76 |

1 INTRODUCTION

1.1 Background

High-mast light poles are used in areas where widespread illumination is required. They are most commonly located at major highway interchanges. The structures are typically 100 ft high or taller, with light fixtures mounted at the top. In addition, the top of a pole houses a lowering device that allows the luminaire to be serviced on the ground without the use of a bucket truck or boom lift. The luminaire and lowering device together constitute a mass concentrated at the top of the relatively light and flexible cantilever.

In recent years, several of these structures have failed, most likely due to fatigue. On November 12, 2003, a high-mast light pole fell along I-29, near Sioux City, Iowa (Chang, Phares, Sarkar, & Wipf, 2009). Fortunately, the structure collapsed in an open area beside the interstate and injured no one. On April 11, 2004, two high-mast structures failed near Denver International Airport as a result of the same wind event but fell away from the roadway (Goode & van de Lindt, 2007). Cracking and failures of high-mast structures have also been reported across the West and Midwest, including in Wyoming, Illinois, Wisconsin, and Missouri (Phares, Sarkar, Wipf, & Chang, 2007). These failures have not received significant media attention because no deaths or injuries resulted. However, due to their location near highways, failures of high-mast structures have the potential to disrupt travel on major roadways, as well as to cause serious injuries or even death.

In addition, high-mast towers are expensive to replace. WYDOT estimates the price of a new high-mast pole and foundation to be \$45,000, excluding the luminaire and lowering device (Fredrick, 2009).

The fatigue failures of high-mast poles have been attributed to wind-induced vibrations and, in particular, the phenomenon of vortex shedding (Chang, Phares, Sarkar, & Wipf, 2009). The primary research objective is to characterize the dynamic effects of wind-induced vibrations on two high-mast structures in Laramie, WY, and to propose several retrofits that increase the aerodynamic damping of the poles, thereby reducing vibrations and associated fatigue damage.

1.2 Field Monitoring

1.2.1 Location

Two high-mast light poles (Figure 1, Figure 2) located in Laramie, WY at the I-80/US287 interchange (Figure 3) were monitored periodically to collect structural response data and record wind speed and direction. The location was selected for its relatively open terrain. The area is level with exception of an approximately 24-ft high highway overpass located about 650 ft (200 m) to the west of the two poles. ASCE 7-05 categorizes the area as Exposure C: “Open terrain with scattered obstructions having heights generally less than 30 ft for most wind directions” (Minimum Design Loads for Buildings and Other Structures, 2005). Laramie is located at an approximate elevation of 7200 ft with an air density of 0.058 pcf.

According to data provided by the Department of Atmospheric Science at the University of Wyoming, the mean yearly wind speed for Laramie is 12.5 mph (based on hourly observations) (Parish, 2009).



Figure 1. 120-ft, 16-sided high-mast light pole

The northern structure is referred to as Pole 3 (Figure 4a), and the pole located approximately 550 ft (170 m) to the south-southeast is referred to as Pole 4 (Figure 4b) in accordance with WYDOT. Poles 3 and 4 were both installed in 2000. Both poles have the same geometry, with a 0.14 in/ft taper and a hexadecagonal (16-sided) tubular steel cross section with a galvanized finish. Each high-mast pole consists of three discrete sections, each with a different constant thickness. The pole geometry is summarized in Table 1 and shown in Figure 2. The three sections connect with slip joints (Figure 5). Currently the minimum overlap required by WYDOT high-mast lighting standards is 28” between Sections A and B, and 19” between Sections B and C. The exact overlap amount was not provided by the manufacturer, however, based on the poles’ geometry, the actual overlap length must be approximately 39.5 in between Sections A and B (Joint 1) and 32 in between Sections B and C (Joint 2). Given the geometry of the pole, its weight is estimated to be approximately 5 kips.

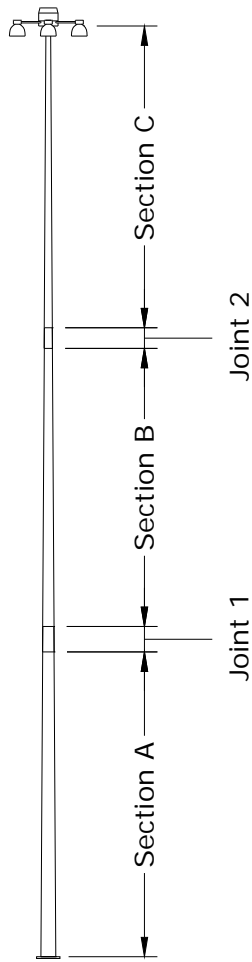


Figure 2. High-mast light pole geometry from shop plans

Table 1. Pole geometry from shop plans

| Section | Base Diameter | Top Diameter | Section Length | Wall Thickness |
|---------|---------------|--------------|----------------|----------------|
| A | 23.00" | 17.04" | 42.59' | 0.3125" |
| B | 18.00" | 12.15" | 41.80' | 0.2500" |
| C | 13.00" | 7.18" | 41.57' | 0.2391" |

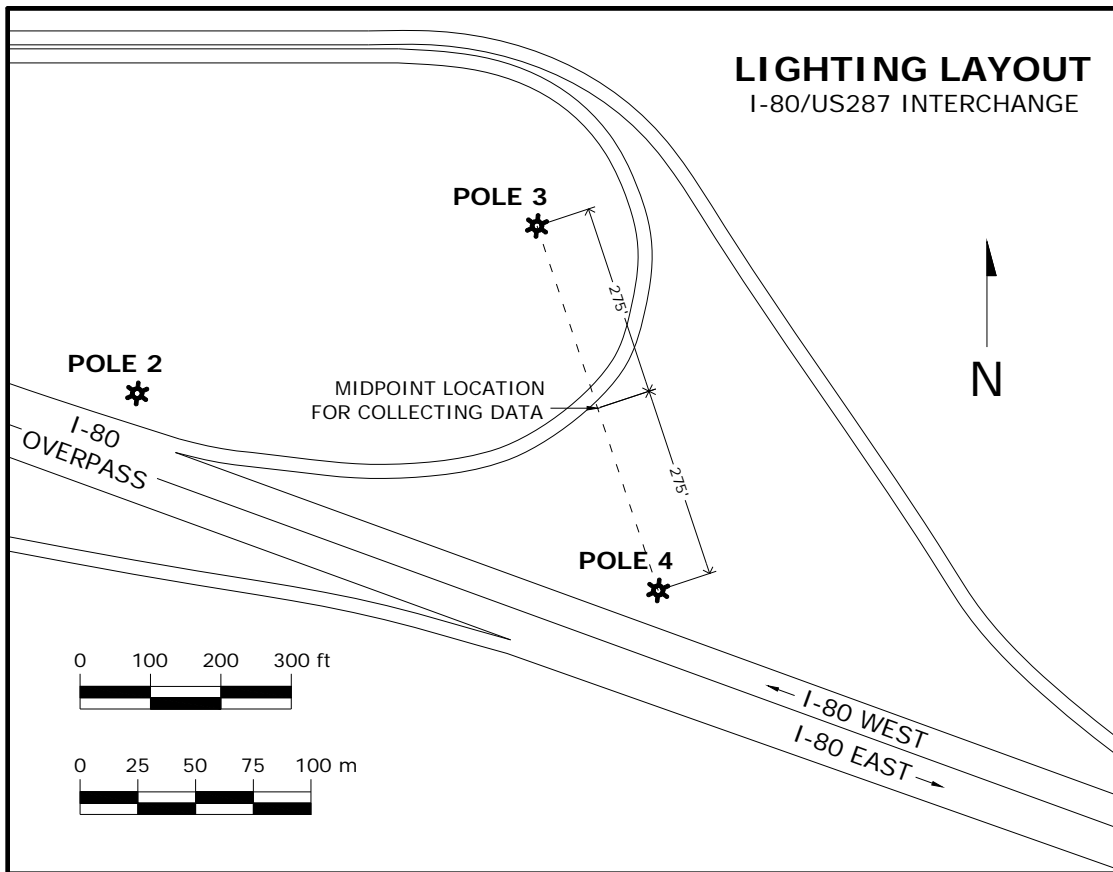


Figure 3. High-mast structure locations



(a)



(b)

Figure 4. Two monitored high-mast light poles, (a) Pole 3 and (b) Pole 4

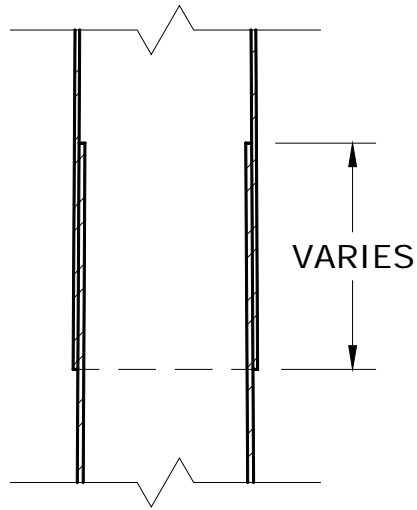


Figure 5. Slip joint splice

In addition, both poles have 0.25" thick backing rings at their respective bases. Each high-mast pole is fixed to a concrete pad with eight 1.75" diameter bolts and a 2" thick base plate with an outer diameter of 35" and a bolt circle diameter of 29". The poles are connected to their respective base plates with full penetration welds and, therefore, AASHTO classifies them as Stress Category E, with a constant amplitude fatigue limit (CAFL) of 4.5 ksi.

An 11" wide, 30" high lockable hinged handhole (Figure 6) is located 15" above the base of the pole. The handhole provides access to the internal drive motor and winch assembly for the lowering device.

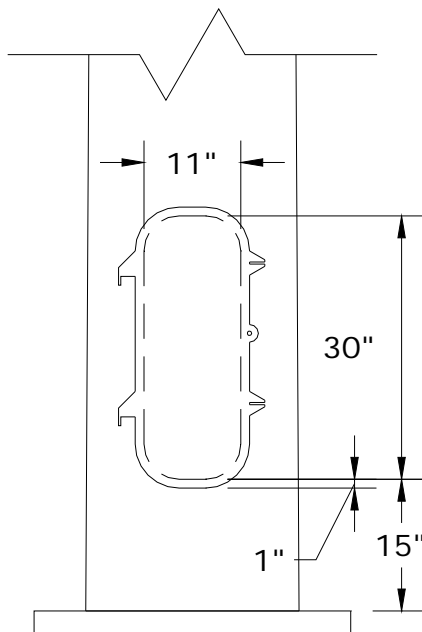


Figure 6. Handhole detail

Each pole also has an HMSC High Mast Cutoff Series Luminaire with six light fixtures and a lowering device at the top. The lowering device is a bottom latching, centering system with internal winch and drive motor (Figure 7). The ring assembly has three wheels intended to keep the luminaire centered (Figure 8). Lowering the luminaire is somewhat erratic, and it may rotate while being lowered. The luminaire ring on Pole 3 rotated by greater than 90° on both lowering and raising, while the luminaire on Pole 4 appeared to travel straight up and down. When the luminaire rotates on the way down, it rotates in the reverse direction on the way back up because it is drawn back to the starting position by the cables, so the lower-raise behavior is not entirely unpredictable.

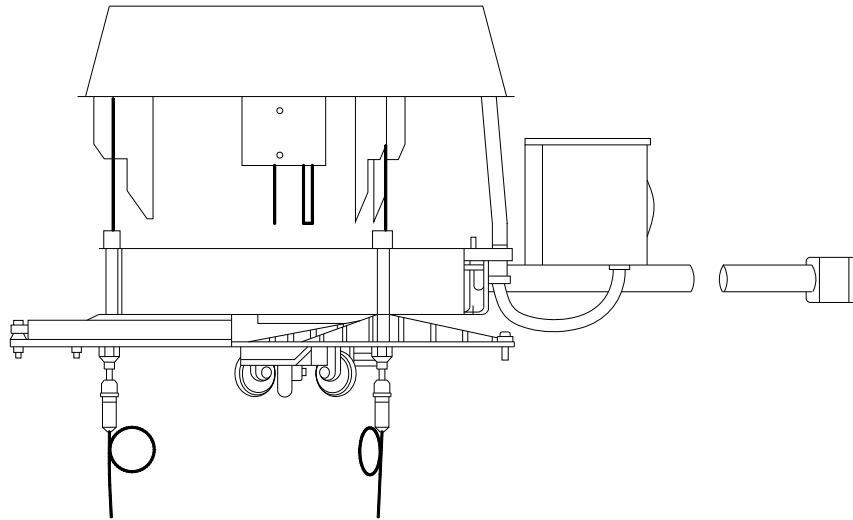


Figure 7. Lowering device

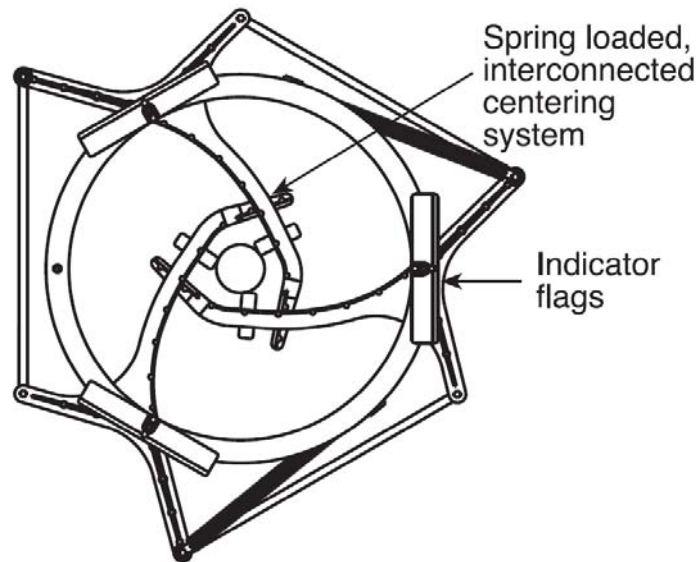


Figure 8. Ring assembly with centering system



Figure 9. Ring assembly and luminaire on pole

Both high-mast light poles are bolted to 4-ft diameter concrete drilled shaft foundations. Each drilled shaft is reinforced with 18 No. 9 steel reinforcing bars and a No. 4 steel spiral. The depth and approximate weight of each foundation is given in Table 2.

Table 2. Drilled shaft specifications

| Pole | Depth (ft) | Weight (kips) |
|-------------|-------------------|----------------------|
| 3 | 19.7 | 37 |
| 4 | 24.6 | 47 |

Pole 3 is described to be “founded in very hard interbedded shale, siltstone, and sandstone”. Pole 4 is “founded in compact to very hard siltstone and sandstone” (Wyoming Department of Transportation, 1997).

1.2.2 Instrumentation

1.2.2.1 Preliminary Testing

The locations of the sensors installed on the two high-mast poles are shown in Figure 10. In all, the wireless nodes on Pole 3 collected twelve channels of data, and the devices on Pole 4 recorded ten channels. All wireless nodes are housed in weather-proof polycarbonate enclosures that seal with rubber gaskets. The enclosures also each contain three D cell batteries that recharge the internal batteries in each node.

Poles 3 and 4 were each initially outfitted with two MicroStrain G-Link wireless triaxial accelerometers (Figure 11), each of which output three channels giving accelerations in the x, y,

and z directions. The accelerometers have a range of $\pm 10g$. All accelerometers have integrated data acquisition devices that log data that can be later retrieved wirelessly.

Each pole had one accelerometer located at 56 ft to record excitation due to Mode 2 (Figure 12). The second accelerometer on each HMLP was located at 41 ft from the base, which corresponds to the lower maximum displacement due to Mode 3. (See Section 3.1 for the modal analysis.) The accelerometers were oriented vertically for ease of mounting, as shown in Figure 11. Consequently, Channels 1, 2, and 3 correspond to the y, x, and z directions respectively.

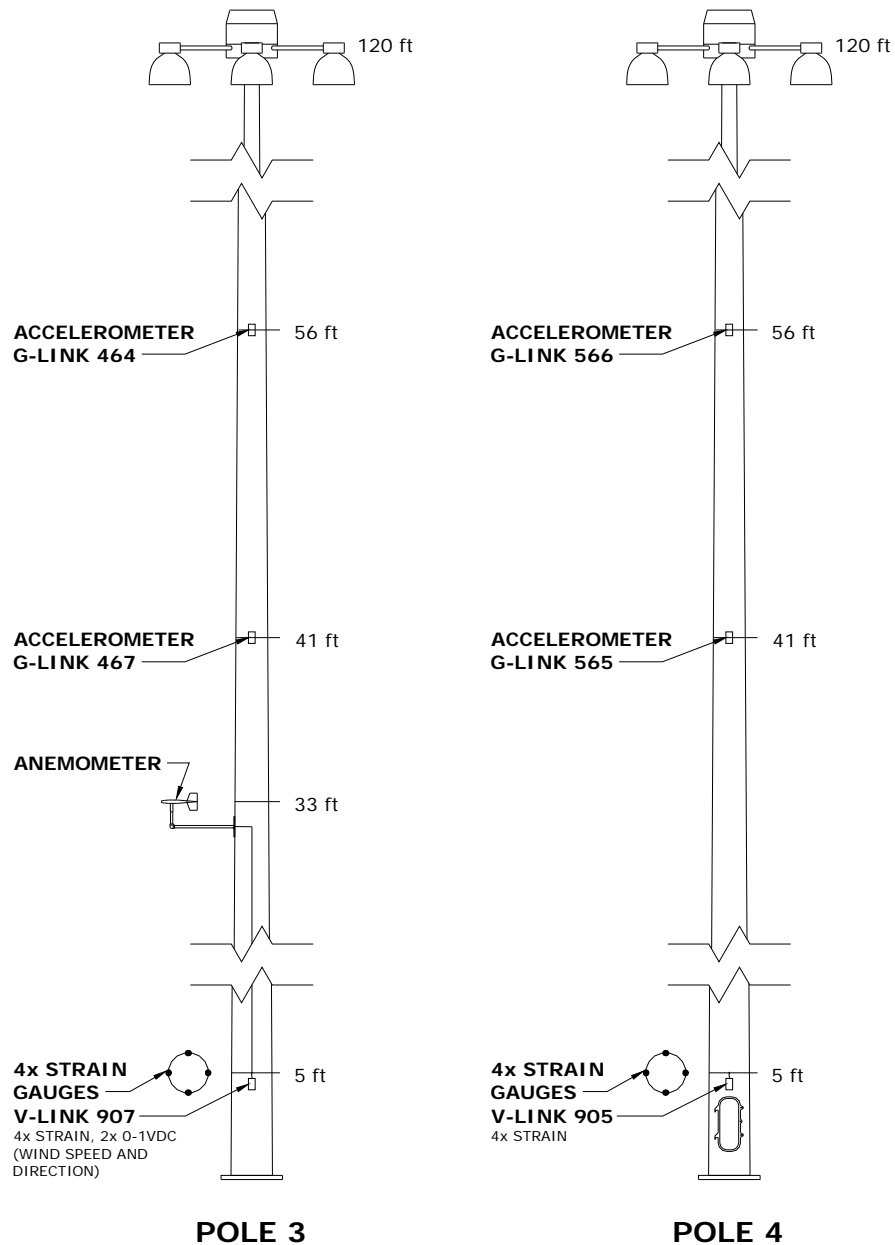


Figure 10. Instrumentation locations for preliminary testing

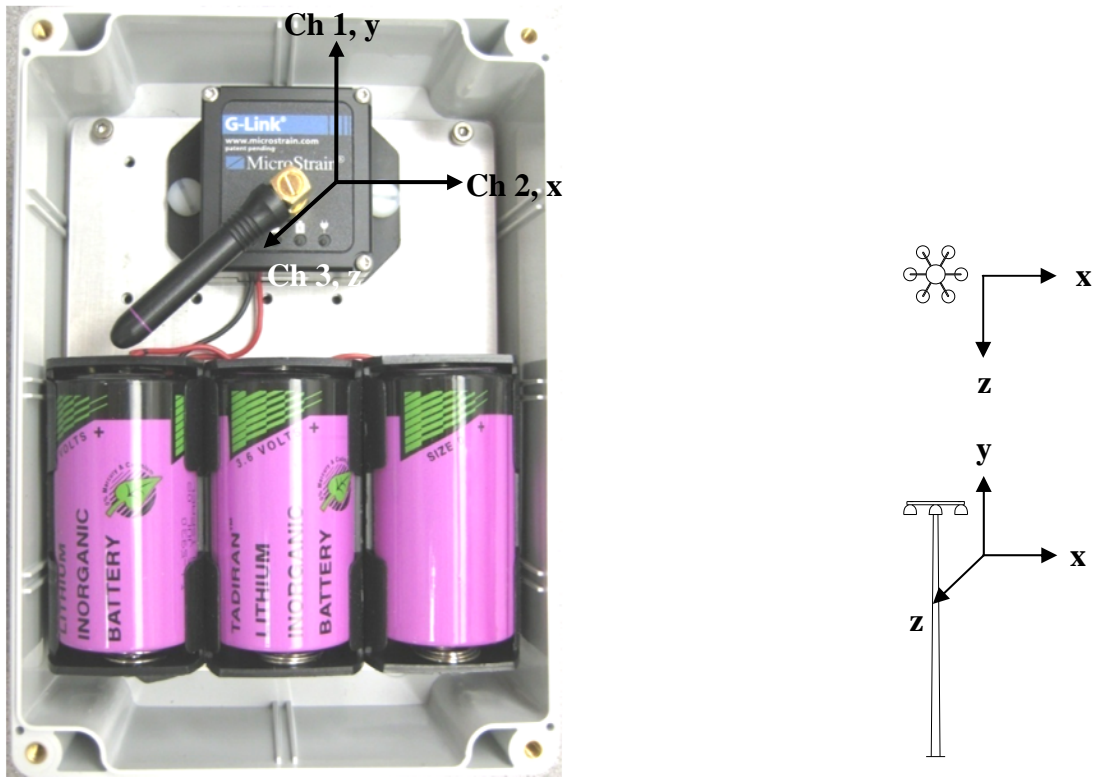


Figure 11. Orientation of G-Link accelerometers

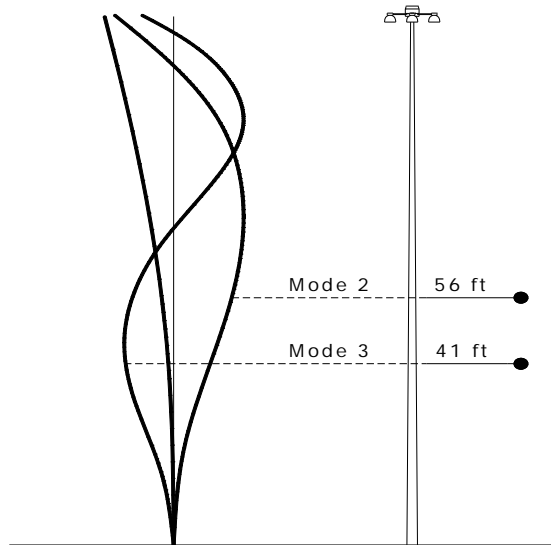


Figure 12. Accelerometer locations relative to mode shapes

Each accelerometer is fitted with an L-com 7 dBi (decibels relative to isotropic) omnidirectional, external antenna, as shown in Figure 13. Figure 14 shows the vertical and horizontal

antenna patterns. These antennas enable a strong, reliable signal for two-way communication between the nodes and the base station.

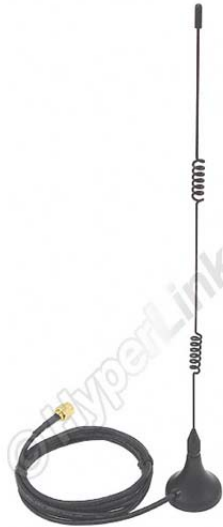


Figure 13. 7 dBi antenna (photo courtesy of L-com)

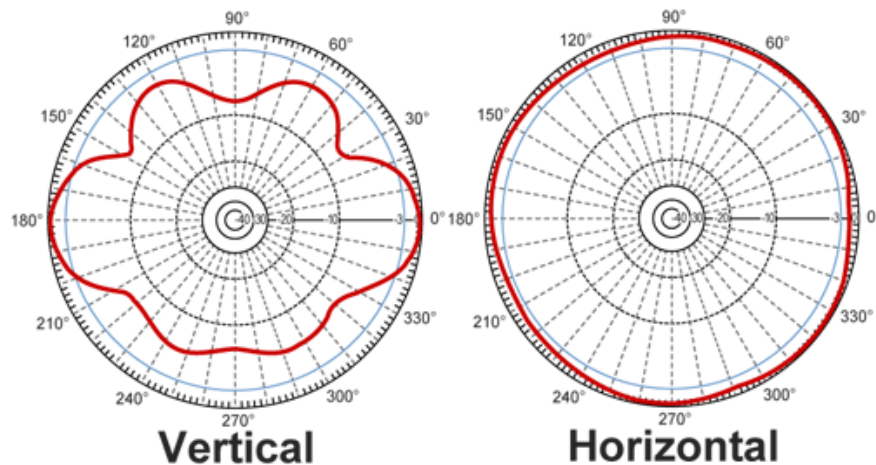


Figure 14. RF antenna patterns for 7 dBi antenna (diagram courtesy of L-com)

Both poles had four Vishay Micro-Measurements 350 Ω bondable foil strain gauges (C2A-06-250LW-350, Figure 15) located 60” from the base, and 15” above the handhole opening. All strain gauges are uniaxial with a gauge length of 0.25” and a gauge factor of 2.095 \pm 0.5%.

Figure 16 shows the locations of the strain gauges. The gauges were located at quarter points along the perimeter of the pole. Strain gauges on each pole were wired to a MicroStrain V-Link wireless voltage node that logs data and transmits to the base station. Each V-Link was also fitted with a 7 dBi, omni-directional antenna. The strains from gauges 180° opposite each

other were averaged, and a transformation was performed to determine alongwind and crosswind strains.



Figure 15. Micro-Measurements strain gauge

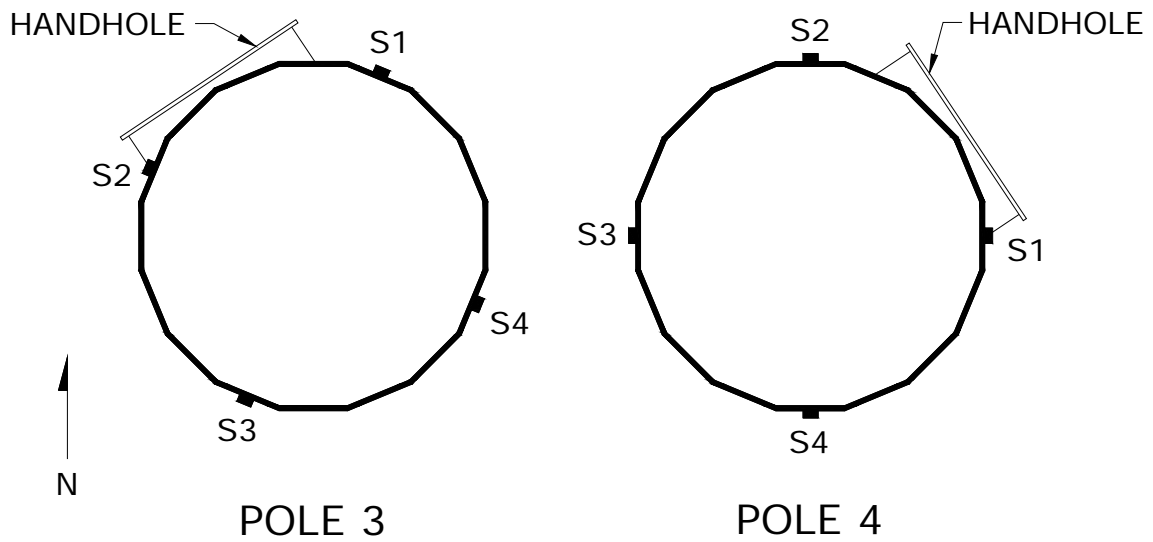


Figure 16. Detail of strain gauge locations

Pole 3 was additionally outfitted with an R.M. Young propeller vane anemometer (Model 05103VP, Figure 17) that measures wind speed and direction. The anemometer was located at 33 ft (10 m) from the base of the pole. It was mounted on an L-shaped bracket consisting of two 1” pipes connected with an elbow and welded to a steel plate that is affixed to the pole with two hose clamps (Figure 18). A cable connected the anemometer to Pole 3’s wireless node delivering two channels of data (wind speed and direction) to the data logging device. In addition, it was connected to a 9V battery that provided the output voltage for the anemometer. The output for wind speed is 0 to 1 VDC which corresponds to 0 to 100 mph. The wind direction output is 0 to 1 VDC, corresponding to 0 to 360 degrees of rotation. Calibration data for the anemometer were provided by the manufacturer.



Figure 17. Propeller vane anemometer (photo courtesy of R.M. Young)



Figure 18. Anemometer mounted on high-mast pole

An Agile-Link 2.4 GHz USB base station (Figure 19) was used to trigger the wireless nodes to log data and to retrieve data from the nodes. The base station was fitted with an L-com 9 dBi omni-directional range extending “rubber duck” antenna (Model HG2409RD-RSP, Figure 20). The omni-directional characteristic was required in order to simultaneously trigger wireless nodes on both poles. Figure 21 shows the vertical and horizontal antenna patterns. The antenna was mounted on an 8 ft telescoping pole, giving it a total elevation of approximately 12 ft.



Figure 19. USB base station (photo courtesy of Microstrain)

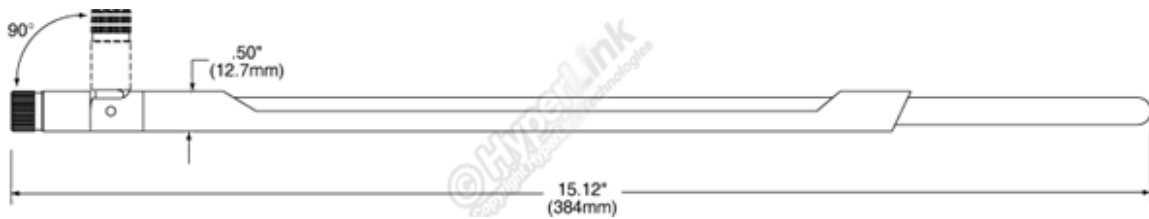


Figure 20. 9 dBi antenna (diagram courtesy of L-com)

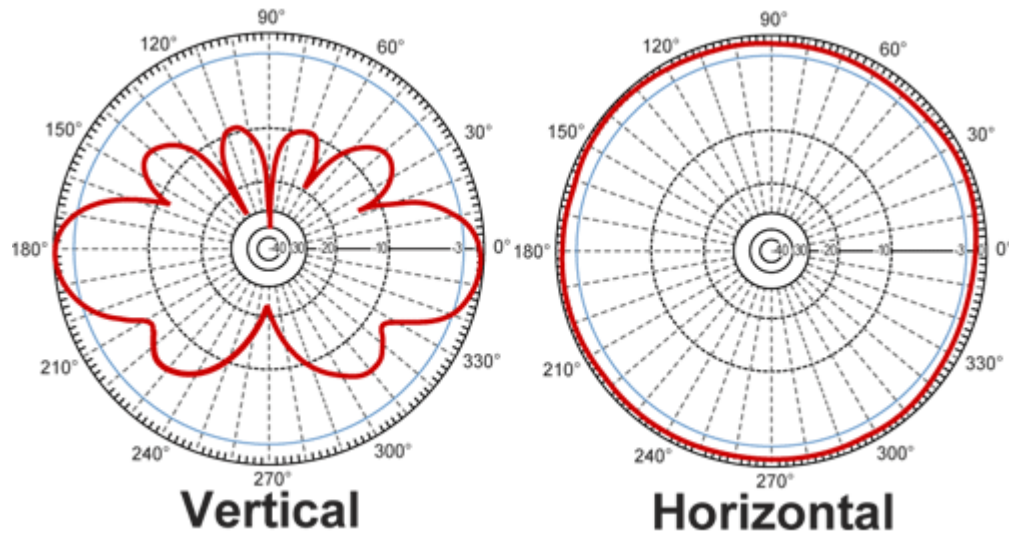


Figure 21. RF antenna patterns for 9 dBi antenna

Strain and acceleration data were recorded when the wind speed was within a predetermined range around one of the critical velocities for the pole. The critical velocities were

calculated using the AASHTO *Specifications*, NCHRP Report 469 Appendix B, and the fundamental frequencies of the pole determined with SAP2000 (Section 3.2). Wind speed and direction were recorded during the same intervals.

All data acquisition devices are 12-bit, and a sampling rate of 128 Hz was used. The V-Link takes an input of 3VDC, and the output from both anemometer channels is only 1 VDC. Therefore, only one-third of the 12-bit capacity is utilized, and the maximum output from the anemometer is $1365 \text{ bits} = 2^{12}/3$, rather than $4096 \text{ bits} = 2^{12}$.

The wireless devices use IEEE 802.15.4 open communication architecture, also known as ZigBee. They are configured and triggered to log data using the MicroStrain Node Commander software (Figure 22).

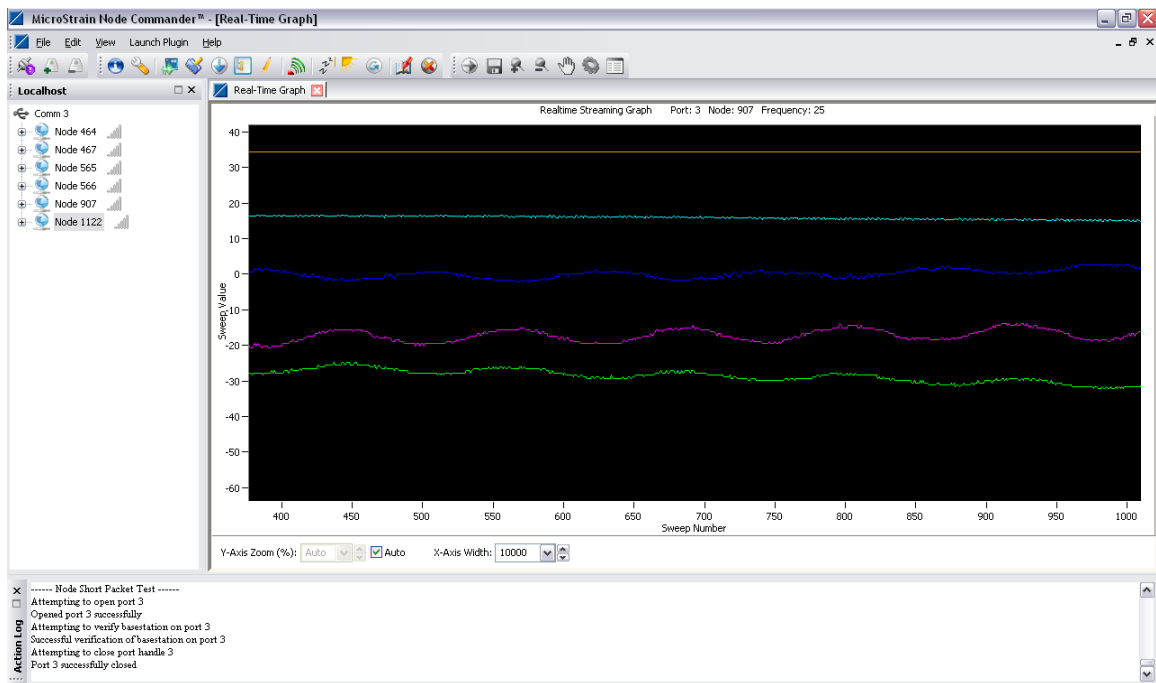


Figure 22. Node Commander software

1.2.2.2 Traffic Vibration Testing

Bridge Diagnostics, Inc. (BDI) equipment was used to measure pole vibrations induced by vehicle traffic. The system used a wifi base station (Figure 23) and transmitter (Figure 24). Two accelerometers (Figure 24) were mounted on Pole 4 at 18 ft in north-south and east-west orientations. A third accelerometer was initially mounted on the base plate of Pole 4 to record any vertical vibrations. Figure 25 shows this arrangement. The third accelerometer was later mounted on a nearby 24" x 36" x 3" concrete slab to measure lateral ground vibrations. The accelerometers were connected to the transmitter which wirelessly transmitted data to the base

station which was connected to a laptop. BDI WinSTS Data Acquisition Software (Figure 26) installed on the laptop was used to collect acceleration data in real time.



Figure 23. BDI mobile base station

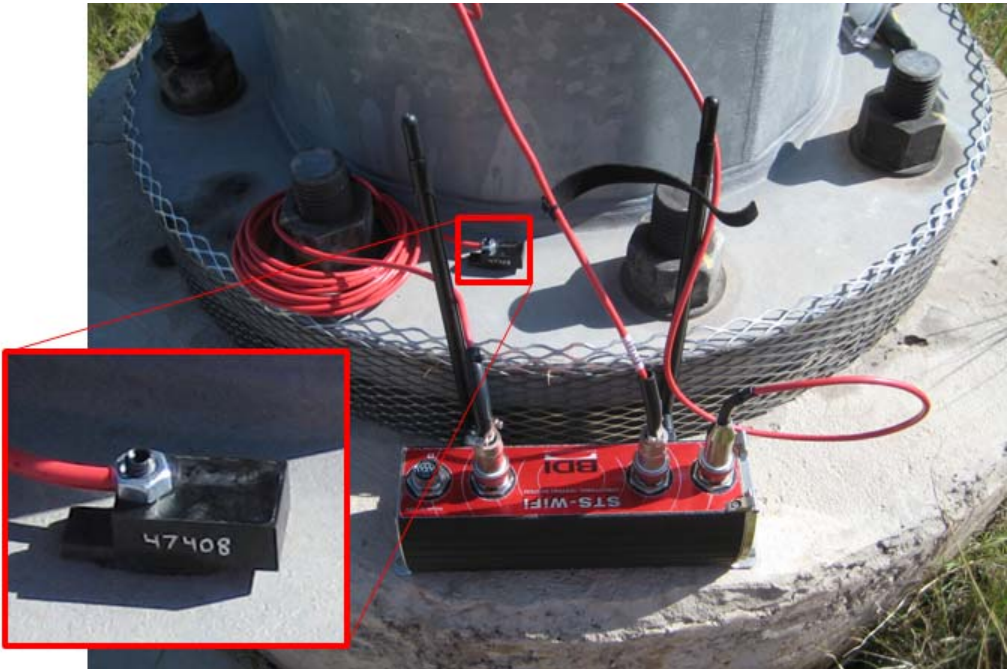


Figure 24. BDI wireless transmitter and accelerometer

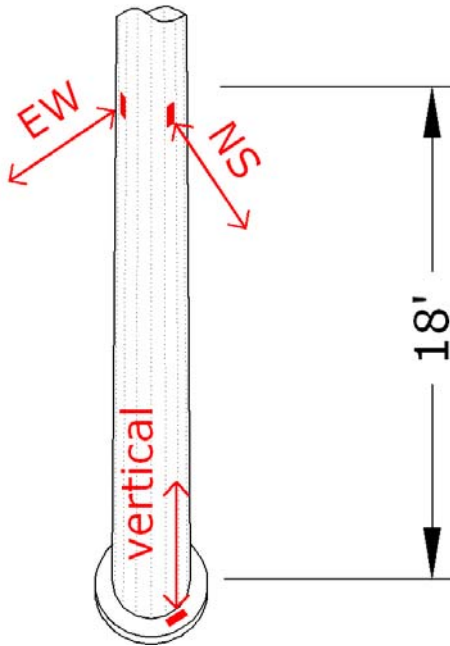


Figure 25. Locations of uniaxial BDI accelerometers for retrofit testing

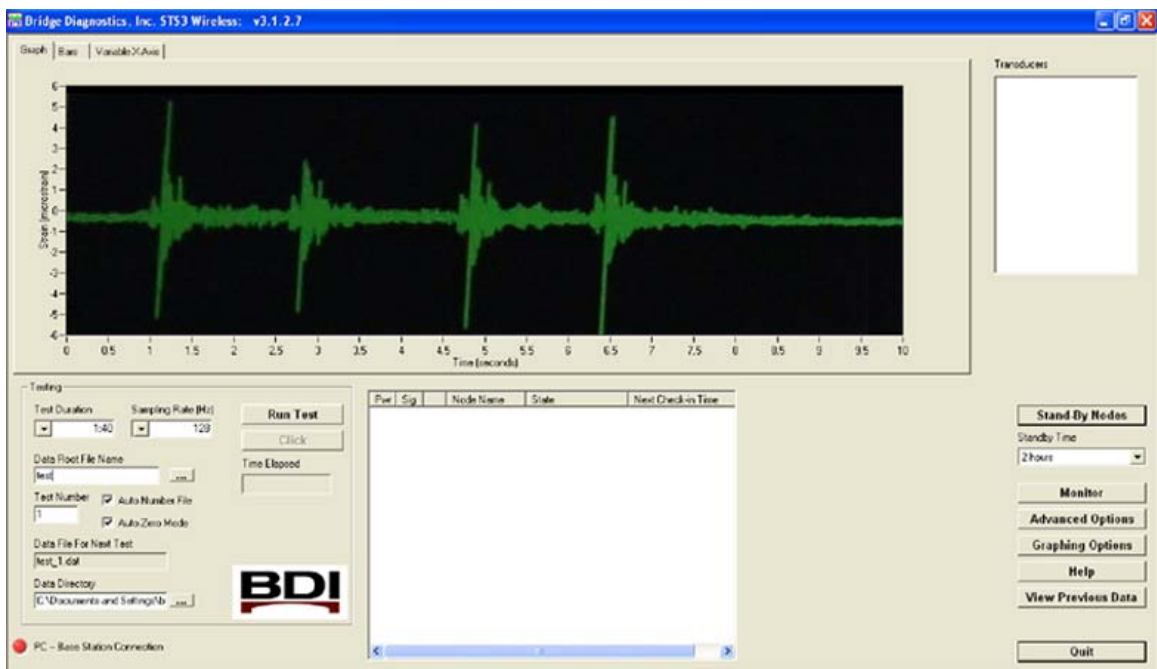


Figure 26. WinSTS Data Acquisition Software

1.2.2.3 Retrofit Testing

The experimental setup for retrofit testing was the same as that used for preliminary testing, except that only Pole 3 was utilized. Figure 27 shows the instrumentation locations.

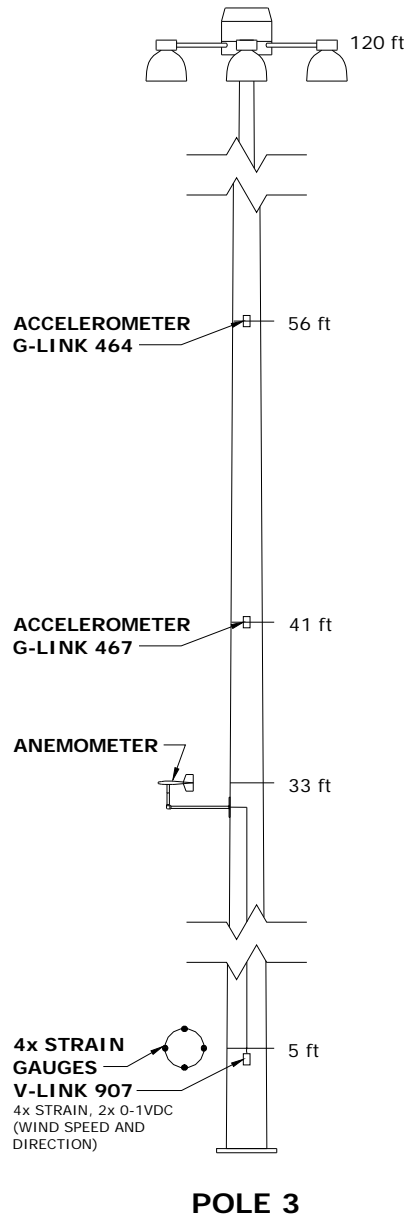


Figure 27. Instrumentation locations for retrofit testing

1.3 Wind-Induced Vibrations

High-mast poles are susceptible to vibrations due to natural wind gusts and vortex shedding.

1.3.1 Buffeting

Buffeting, or the effect of natural wind gusts, is the along-wind response of the structure. Buffeting is caused by velocity fluctuations that cause unsteady loading of the structure and is not self-induced. This unsteady flow is the result of turbulence (Reid, 2008). Unlike vortex shedding, which occurs at specific frequencies and causes amplified oscillations at frequencies near the structure's natural frequencies, buffeting includes frequencies of eddies naturally occurring in the wind, in addition to those caused by the interaction between the wind and the structure. The excitation due to buffeting can be significant if the average wind velocity is high, the natural frequencies of the structure are below 1 Hz, the wind is highly turbulent, or the mechanical damping is low. Also, unlike vortex shedding, where maximum excitation occurs in a small range of wind speeds, loads due to natural wind gusts increase as the wind velocity increases (Phares, Sarkar, Wipf, & Chang, 2007).

1.3.2 Vortex Shedding

Vortex shedding causes vibrations transverse to the direction of the wind. Vortex shedding occurs when a fluid, in this case air, flows around a bluff body. When the flow separates, low pressure vortices are formed on the leeward side of the object (Figure 28). When a vortex forms, it reduces the pressure on one side of the object and causes the object to move in that direction. As the flow continues, the vortices alternate sides causing the body to move back and forth transverse to the wind direction. When this harmonic motion approaches the natural frequency of the structure, the vortex shedding frequency can couple with the structure's natural frequency and cause significant deflections and stresses to occur. This phenomenon is referred to as "lock-in". Over time these vortex-induced vibrations can fatigue a structure and eventually cause it to fail. Fatigue due to vortex shedding can be identified given knowledge of the prevailing wind direction and the orientation of cracking (Chang, Phares, Sarkar, & Wipf, 2009).

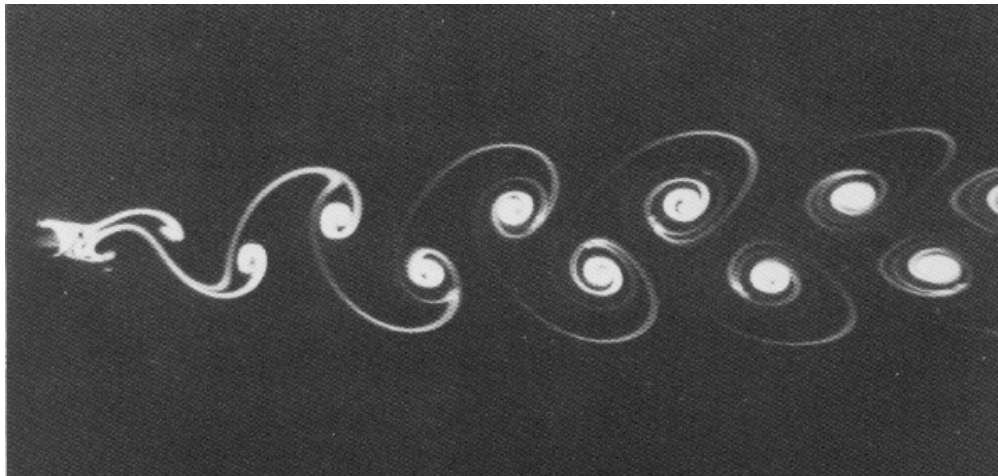


Figure 28. Photograph of a vortex street (Van Dyke, 1982)

2 LITERATURE REVIEW

2.1 Definitions

2.1.1 Bluff

Bluff structures include any structures that are not aerodynamically streamlined at the design phase, such as bridges, buildings, heat exchanger tubes, and cooling towers (Kumar, Sohn, & Gowda, 2008).

2.1.2 Boundary Layer

The term boundary layer refers to the thin layer of fluid flowing around a body that is affected by the friction between the fluid and the body. The fluid's velocity ranges from zero at the surface of the body to the maximum free-stream velocity at the outer edge of the boundary layer. Outside of the boundary layer the flow is laminar. The boundary layer comprises the viscous region while the area outside of it is referred to as the inviscid region.

Because of inertia, the fluid flow may separate from the surface of the body. Flow separation causes vortices to be shed on alternating sides of the body resulting in a turbulent wake behind the body.

Figure 29 shows the flow around a cylinder. The location of the flow separation varies with the Reynolds number, which is dependent upon fluid characteristics, the flow velocity, and the shape and diameter of the cylinder. Below a certain critical Reynolds number, flow is laminar and separation does not occur.

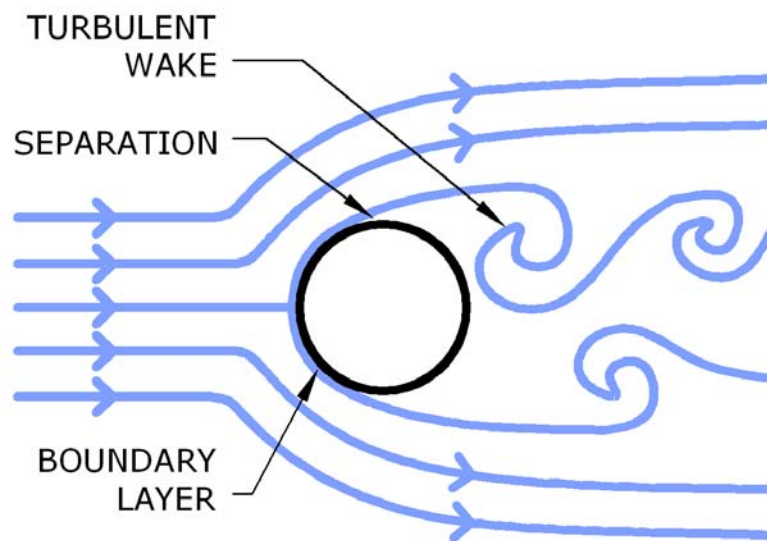


Figure 29. Boundary layer with flow separation

2.1.3 Atmospheric Boundary Layer

The term boundary layer may also refer to the region of frictional influence above the Earth's surface (Holmes, *Wind Loading of Structures*, 2001). The Earth exerts a horizontal drag force on air moving across its surface, which acts to retard the air flow. The drag force decreases as the height above the ground increases and becomes negligible above a height δ , that is, the height of the boundary layer. Air velocity within the boundary layer varies from zero at the surface to its full free flow rate, which corresponds to the external flow (Simiu & Scanlon, 1986). Figure 30 shows a typical boundary layer velocity profile.

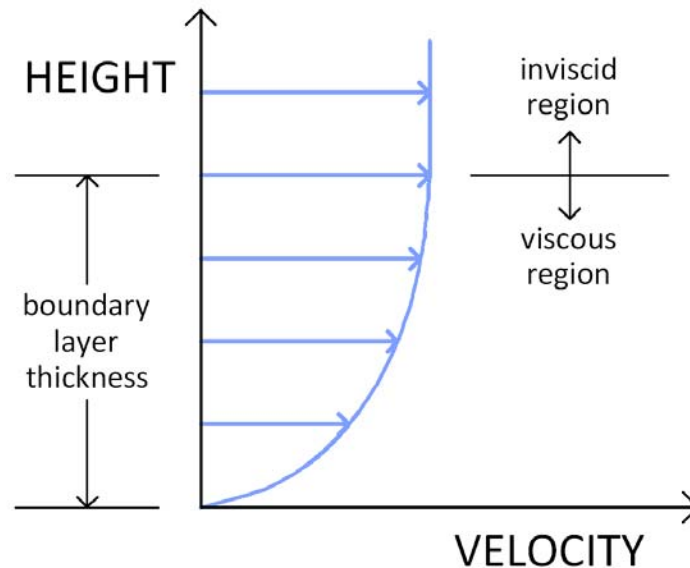


Figure 30. A typical atmospheric boundary layer velocity profile

2.1.4 Reynolds Number

The Reynolds Number, Re , is a non-dimensional parameter that expresses the ratio of inertial to viscous forces acting on a body (Simiu & Scanlon, 1986). Inertial forces control the fluid force when the ratio is large, and viscous forces control when the ratio is small. It is an index of the type of flow characteristics or phenomena that may be expected to occur.

The Reynolds Number can be used to evaluate the tendency of vortex shedding to occur on a generic body (Phares, Sarkar, Wipf, & Chang, 2007). It is given by:

$$Re = \frac{\rho U D}{\mu} = \frac{U D}{\nu}$$

where, ρ = the flow density,

U = the wind velocity,

D = the cross-wind dimension of the body,

μ = the coefficient of fluid viscosity, and

ν = the coefficient of kinematic fluid viscosity.

At low Reynolds numbers, where viscous forces dominate, the flow is laminar. At high Reynolds numbers, where inertial forces dominate, the flow is turbulent and is characterized by vortices, random eddies, and other fluctuations (Reid, 2008).

It is commonly acknowledged that vortex shedding is strong and periodic when the Reynolds Number is between 300 and 3.5×10^5 (Phares, Sarkar, Wipf, & Chang, 2007). Figure 31 shows how flow around a circular cylinder varies with the Reynolds Number.

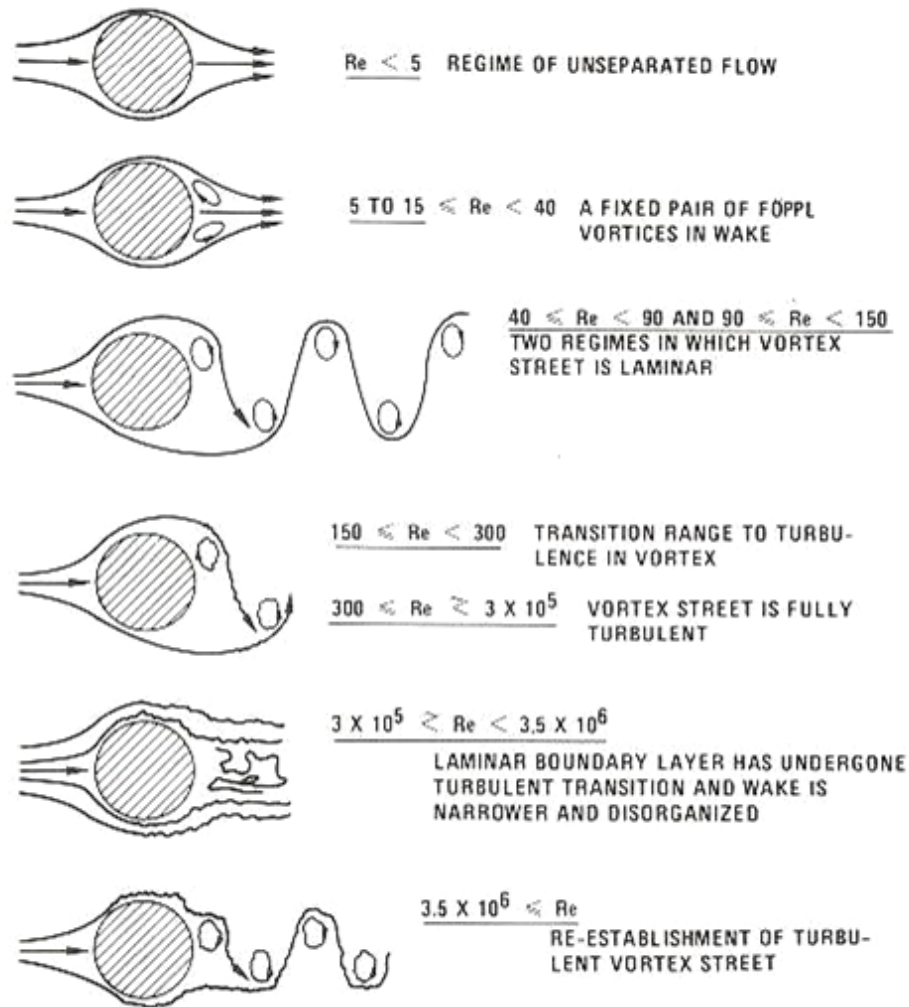


Figure 31. Regimes of fluid flow across smooth circular cylinders (Lienhard, 1966)

2.1.5 Strouhal Number

The Strouhal number, S , is the ratio of the product of the predominant frequency of vortex shedding and the cross-wind dimension of the body to the free stream velocity (Blevins, 1990). It is given by:

$$S = \frac{f_s D}{U}$$

where: f_s = the vortex shedding frequency (Hz),

U = the wind velocity, and

D = the cross-wind dimension of the body.

It is suggested that the value of the Strouhal number be taken as 0.18 for circular sections and 0.15 for multi-sided sections (American Association of State Highway and Transportation Officials, 2009).

2.1.6 Scruton Number

The Scruton number, S_c , is given by:

$$S_c = \frac{4\pi m \zeta}{\rho D^2}$$

where, m = average mass per unit length,

ρ = the flow density,

D = the cross-wind dimension of the body, and

ζ = the critical damping ratio.

The Scruton number can be used to help predict whether a structure is susceptible to vortex-induced vibrations. The Scruton number is inversely proportional to the amplitude of oscillation. The amplitude of oscillation can therefore be decreased by increasing either mass or damping and consequently increasing the Scruton number (Reid, 2008). For circular cylindrical structures, $S_c > 10$ usually indicates low amplitudes of vortex-induced vibrations (Holmes, Towers, chimneys, and masts).

2.1.7 Critical Wind Velocity

The critical wind velocity, V_c , is the wind velocity at which lock-in occurs (American Association of State Highway and Transportation Officials, 2009). For multi-sided sections, it is given by:

$$V_c = 0.68 \frac{f_n D}{S}$$

where, f_n = a natural frequency of the structure (Hz),

D = cross-wind dimension of the body (ft), and

S = the Strouhal number.

V_c is in miles per hour. This relationship is the same as the Strouhal relationship.

The critical wind velocity is also known as the lock-in velocity (Phares, Sarkar, Wipf, & Chang, 2007).

2.1.8 Lock-in

Lock-in is a phenomenon that occurs when the vortex shedding frequency approaches one of the natural frequencies of a structure. When lock-in occurs, significant amplitudes of vibration are caused (American Association of State Highway and Transportation Officials, 2009).

Figure 32 shows the effect of lock-in on the vortex shedding frequency. The Strouhal relationship expresses the vortex shedding frequency as a linear function of the wind velocity. In the lock-in region, however, the vortex shedding frequency is constant and very near to the structure's natural frequency (Phares, Sarkar, Wipf, & Chang, 2007).

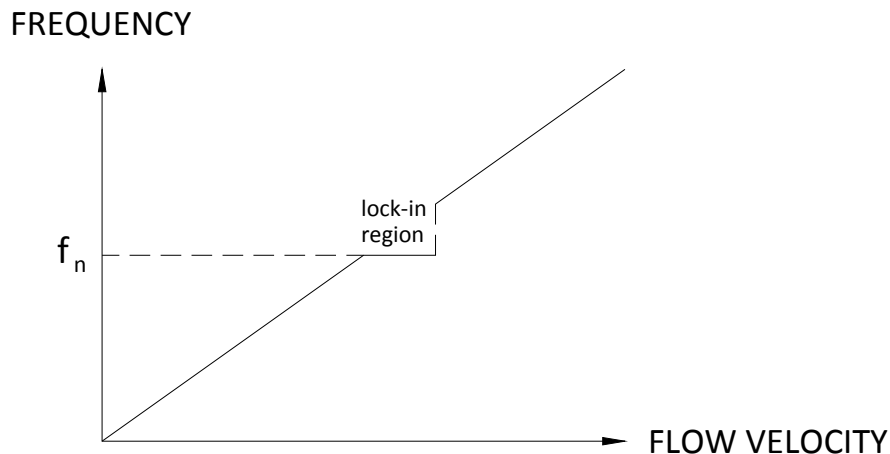


Figure 32. Evolution of vortex shedding frequency with wind velocity over elastic structure (Phares, Sarkar, Wipf, & Chang, 2007)

2.2 Vortex-Induced Vibrations

Vortex-induced vibration (VIV) is a phenomenon that results from the interaction of a bluff body and a moving fluid. Vortex-induced vibrations have the potential to subject a structure to large transverse oscillations which can cause fatigue cracking leading to possible failure. Thus, control of vortex-induced vibrations is important for prolonging the service lives of structures. Light and flexible structures are particularly susceptible to vortex-induced vibrations (Kumar, Sohn, & Gowda, 2008).

A bluff body interacting with a fluid flow at a sufficiently high Reynolds number causes flow to separate, resulting in periodic vortex shedding from alternate sides of the body (Figure 33). At some critical Reynolds numbers, the boundary layers separate from the surface near the widest part of the body and form two shear layers that trail in the flow and bound the wake. The insides of the shear layers are in contact with the object and therefore move much more slowly than the outer portions, which are in contact with the freely flowing fluid. This difference in velocity causes the shear layers to roll into the near wake and form discrete vortices (Blevins, 1990). The vortices cause alternating pressure fluctuations on the sides of the body giving rise to

vibrations. The body and the flow field are coupled – that is, the body’s oscillations influence the flow field and the flow field influences the body. Together they form a non-linear oscillatory system (Kumar, Sohn, & Gowda, 2008).

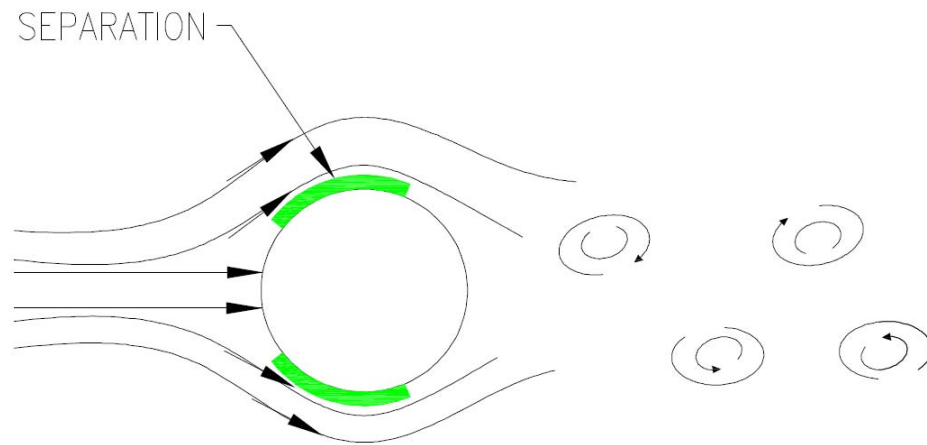


Figure 33. Disturbed airflow around a cylinder (Reid, 2008)

The flow velocity, fluid and flow properties, the dimensions and geometry of the body, damping, and the orientation of the body relative to the direction of flow control the amplitude of the body excitation. Passive control of VIV requires a thorough understanding of the mechanism underlying the process of vortex formation and shedding (Kumar, Sohn, & Gowda, 2008).

The vortex shedding process consists of an upper vortex growing due to the vorticity of the upper shear layer and then drawing the lower shear layer across the wake. The lower shear layer then forms a lower vortex and carries fluid with opposite vorticity and cuts the vorticity supply to the upper vortex causing it to be shed. The lower vortex grows and pulls the upper shear layer across the wake, an upper vortex forms and causes the lower to be shed (Kumar, Sohn, & Gowda, 2008).

2.3 Control of Vortex-Induced Vibrations

“Passive control of Vortex-Induced Vibrations: An Overview” discusses a number of means of passive control of VIV (Kumar, Sohn, & Gowda, 2008). The first is to increase the reduced damping which is given by the Scruton number, S_c . Reduced damping could be increased by varying any of the parameters involved, such as increasing the mass or damping. Damping can be increased through the introduction of a tuned liquid sloshing damper (TLSD). This allows for energy dissipation by means of internal fluid friction and wave breaking action. VIV can also be controlled by avoiding resonance which could be achieved by stiffening the structure. Streamlining structural geometry, that is reducing “bluffness,” is another option for controlling vortex-induced vibrations.

2.4 Traffic-Induced Vibrations

Traffic-induced vibrations are primarily due to heavy vehicles, such as buses and trucks, traveling at relatively high speeds on uneven road surfaces. Irregularities in the road surface (e.g. cracks and potholes) subject the vehicle to vertical oscillations that induce dynamic axle loads (Hunaidi, 2000). Dynamic axle loads are controlled by the vehicle's dynamic characteristics and the road's unevenness and flexibility. The vehicle's wheels interact with the road surface causing a dynamic excitation, which produces waves that propagate in the soil surrounding the roadway (Lombaert, Degrande, & Clouteau, 2000).

Traffic-induced ground vibrations are primarily composed of surface waves, and body waves reflected off deep soil layers are typically negligible. The vibrations have horizontal and vertical components with similar characteristics. However, the effect of vertical motion on a structure is usually neglected because most structures (including high-mast poles) have a large axial stiffness, meaning that the vertical motion is not likely to excite the structure vertically (Hao, Ang, & Shen, 2001).

Researchers in Singapore found that most traffic-induced vibrations are between 10 and 20 Hz. These vibrations are mainly due to vehicle wheel-hopping as wheel-hopping frequencies for most vehicles are in the 10 to 20 Hz range (Hao, Ang, & Shen, 2001). According to the National Research Council Canada, traffic-induced vibrations have a wider range of frequencies and can be between 5 and 25 Hz with amplitudes between 0.0005 and 0.2 g. There are many factors that influence the dominant frequencies and amplitude of traffic vibrations: road conditions, vehicle weight and speed, vehicle suspension, soil conditions, time of year (whether the ground is wet, frozen, etc.), and distance from the road. The effects of these factors are mutually dependent, and it is difficult to define simple relationships between them (Hunaidi, 2000).

2.5 High-mast Lighting Structures

2.5.1 Iowa State University

Researchers at Iowa State University conducted a study of two dodecagonal high-mast light poles located in open terrain in a high-wind region in Northern Iowa. Two 148-ft weathering steel poles with an approximate taper of 0.14 in/ft (referred to as Pole 1 and Pole 2) were monitored between October 2004 and January 2006. Pole 2 was retrofitted with a 1.5-in thick, 5.25-ft high steel splice jacket at the base.

Pole 1 was used to collect dynamic response data using 14 strain gauges and four accelerometers. Pole 2 was used to collect wind profile data using three anemometers. In addition, wind speed and direction were recorded using a propeller vane anemometer at the top of a 33 ft pole directly adjacent to Pole 1. All data were transmitted from the poles via a satellite internet connection (Phares, Sarkar, Wipf, & Chang, 2007).

A pluck test was used to determine the pole's natural frequencies and damping ratios. A cable attached to the pole shaft and a stationary object was pulled and released to excite the pole. The findings are summarized in Table 3 and Table 4.

Table 3. Iowa pole response data

| Mode | 1 | 2 | 3 | 4 |
|-------------------------------|----------|----------|----------|----------|
| Period (s) | 3.3 | 0.77 | 0.30 | 0.16 |
| Natural Frequency (Hz) | 0.30 | 1.3 | 3.3 | 6.4 |

Table 4. Iowa pole damping data

| Mode | 1 | 2 | 3 | 4 |
|--------------------------|----------|----------|----------|----------|
| Damping Ratio (%) | 0.60 | 0.17 | 0.27 | 0.30 |

The research group at Iowa performed long-term monitoring and used the results to formulate a mathematical model for predicting aerodynamic loads. Wind gust and vortex shedding data were extracted from the long-term data for in-depth analysis. At each pole, average wind data were recorded continuously. At Pole 1 the data logger recorded on a three minute interval, and at Pole 2 it recorded at a one minute interval. For each interval, average and maximum wind speed and average wind direction were logged. The researchers obtained the dominant wind speed and direction from these data.

Strain and acceleration data were logged in one minute intervals when the wind speed was within a specific range. Stresses were compared to wind speed and direction data. When the average wind speed exceeded 10 mph, it was observed that stress ranges in the across-wind and along-wind directions were of similar magnitude. This indicates that the pole vibrated in both directions. Strain data also indicated that when wind speeds were approximately 6.0 mph at 33 ft, the pole's motion was transverse to the wind direction. This suggests that the excitation was due to vortex shedding, likely in the second mode as the critical velocity for second mode was predicted to be 5.11 mph.

The Iowa team found that the highest stress ranges resulted from wind gusts over 20 mph. Gust induced vibration was found to be mainly in the first mode of vibration, and the maximum stress range was observed to be 12.4 ksi at 5.75 ft above the base of the pole. Wind speeds above 20 mph occurred less than 5% of the time, so it was concluded that buffeting did not significantly contribute to fatigue damage.

During the long-term monitoring, vortex shedding was observed primarily in the second mode of vibration. It was frequently observed at low wind speeds of 3 to 8 mph. Third mode excitation was occasionally observed but was not stable enough to cause significant stresses. The maximum stress range caused by second mode vortex shedding vibrations was determined to exceed the CAFL of 2.6 ksi (Category E'). They concluded that second mode response should be considered in the fatigue design of high-mast structures.

The second mode damping ratio calculated from the pluck test was found to be 0.17%. AASHTO recommends using a damping ratio of 0.5% for vortex shedding fatigue design when the actual damping is unknown. Based on the Iowa study, this value appears to be unconservative. Therefore, for fatigue design due to vortex shedding for poles similar to these, a

conservative value of the damping ratio should be less than 0.5%. Note that the load effect is inversely proportional to damping for harmonic loading. Therefore, the difference between 0.17% and 0.5% is significant.

The Iowa research group recommends that, to increase the fatigue life of high-mast light poles, they be retrofitted like Pole 2. They also suggest that vortex suppression devices such as a perforated shroud or other damping device be used to reduce vortex-induced vibrations (Phares, Sarkar, Wipf, & Chang, 2007).

2.5.2 *Colorado State University*

Researchers in Colorado conducted an investigation of high-mast structures following the failure of two light towers near Denver International Airport in 2004 (Goode & van de Lindt, 2007). The preliminary findings indicated that the failures were due to fatigue cracks that were initiated and that propagated under high stress cycles. Visual inspection of the collapsed pole revealed little to no corrosion on the crack surface suggesting a high crack propagation rate. Thus, the collapse of the pole was likely due to a single wind event.

In addition, the wall thickness of the pole was found to be 0.235 in (5.97 mm), or 6% less than the specified wall thickness of 0.25 in (6.35 mm). Though this may seem insignificant, the fatigue life of a structure is quite sensitive to wall thickness, base plate thickness, and weld details.

The Colorado study goes on to develop a method for determining the reliability index for the desired fatigue life of a high-mast structure by prescribing the surface area of the luminaires, pole height, diameter, and wall thickness.

2.6 **Damping Measurements**

A study was conducted at the University of Genova, Italy to determine the damping characteristics of steel poles and tubular towers (Pagnini & Solari, 2001). Four structures were investigated, and the logarithmic damping decrement as a function of motion amplitude was obtained for each of them.

Steel poles and towers are structurally simple; however, their flexibility and slenderness may cause extreme dynamic responses when subjected to wind-induced vibrations. Lumped masses present on lighting structures may further exacerbate a pole's response. The authors studied wind actions and effects on tubular structures and formulated a response model that takes into account buffeting, galloping, and vortex shedding. They determined that mechanical damping plays a vital role in the dynamic response.

Numerical evaluations of a variety of steel columns and tubular towers showed that foundations are typically very stiff compared to the structures. Consequently, even when ground conditions are quite soft, soil-structure interaction has little effect on energy dissipation in the first fundamental mode of vibration. At higher modes, the stiffnesses of the structure and foundation are comparable, so the soil contributes more to damping.

Aerodynamic damping results from the energy exchange between a fluid flow and a structure. When a structure is slender and light, its aerodynamic damping is high.

In order to obtain damping estimates for poles and tubular structures, the researchers undertook a full-scale investigation of four structures. They obtained damping estimates based on both ambient vibrations and oscillations induced by pluck tests. The pluck tests involved attaching a cable to the column shaft and pulling it to induce a large deformation state. The cable was spliced with nylon wires that were calibrated to break at the stress required to impose a predetermined displacement. Linear accelerometers were located along the pole to obtain the response for each of the first three modes of vibration, as shown in Figure 34.

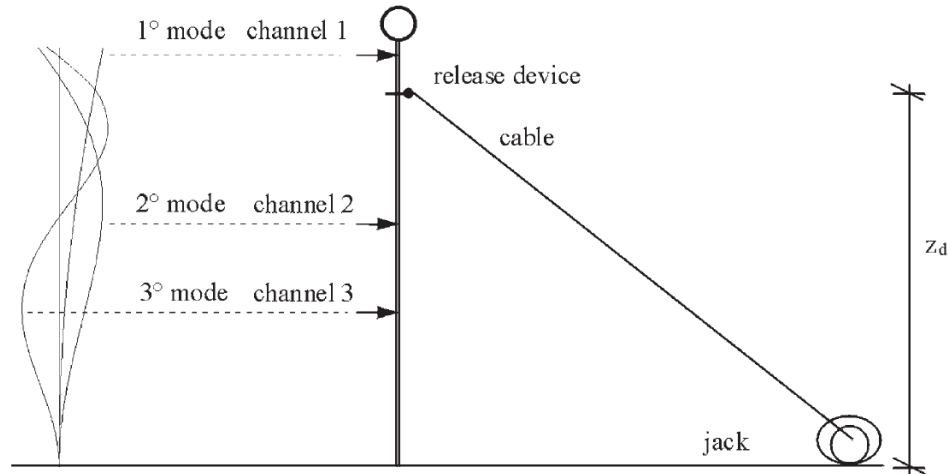


Figure 34. Pluck test scheme(Pagnini & Solari, 2001)

Displacement values were determined from frequency domain analyses of the acceleration data, and harmonic filters allowed the oscillation decay for specific modes to be obtained. Structural damping coefficients were determined using the logarithmic decrement method.

The four structures were a 30-m (98-ft) high Geo Tower that supports an 800-kg (1760-lb) light fixture, a 10-m (33-ft) high conical column with an 11-kg (24-lb) luminaire, a 12-m (39-ft) high light support comprised of five segments of decreasing diameter also with an 11-kg luminaire, and a 14-m (46-ft) high urban light pole supporting 145-kg (320-lb) of lighting equipment. The 10 and 12-m structures were erected specifically for the tests.

Table 5. Genova pole response data

| Natural Frequency (Hz) | 1 | 2 | 3 |
|------------------------|------|------|-------|
| 98 ft Geo Tower | 0.33 | 1.95 | 5.70 |
| 33 ft Conical Column | 1.15 | 4.70 | 11.80 |
| 39 ft Segmented Pole | 1.27 | 5.60 | -- |
| 46 ft Urban Light Pole | 0.57 | -- | -- |

The first modal damping ratio computed for the Geo Tower is 4.5% at small vibration amplitudes. For the other structures, the small amplitude damping ratios are between 2 and 6%.

Results are compared by plotting the measured damping coefficients versus tip displacement and base stress. The plots of experimental values initially show an increase in damping corresponding to an increase in displacement amplitude followed by nearly constant damping. When the displacement is between 0.5 to 1% of the height of the pole, damping increases with the amplitude of vibration. It crests when the displacement is approximately 2.5 to 3% of the height of the structure.

2.7 Aerodynamic Damping

Add-on devices and body surface modifications provide a large number of options for the suppression of vortex-induced oscillations. These work by changing the geometry and, therefore, the aerodynamic properties of a structure (Kumar, Sohn, & Gowda, 2008).

Helical strakes (Figure 35, Figure 37a) have been proven to significantly reduce VIV and are widely used in industrial and offshore applications. These consist of metal or flexible elastomer ribs spirally wound on a member in a definite fashion. Research has shown that round stacks and chimneys do not require strakes with a height greater than $D/8$ (D = crosswind dimension). Typically three equiangularly spaced ribs with $h = 0.1D$ and a pitch of $15D$ are sufficient. Additionally, helical strakes can be effective when only applied to approximately half of the body. They function by adversely affecting shear layer roll up and disrupt vortex formation and shedding. One drawback is that strakes increase the drag coefficient of a member (Kumar, Sohn, & Gowda, 2008).



Figure 35. Helical strakes on stacks at the Mountain Cement Company in Laramie, WY

A perforated shroud is a thin metal cylinder that surrounds a cylindrical member. A shroud typically has an outer diameter of $1.25D$, and covers 45-55% of a cylinder. Its perforated area is 30-40% of its total area, and perforations are approximately 0.5 in. The perforated shroud curtails VIV by affecting the entrainment layers. In addition, it lowers drag (Kumar, Sohn, & Gowda, 2008).



Figure 36. Perforated shroud (Kumar, Sohn, & Gowda, 2008)

Axial slats are essentially a shroud consisting of individual slats. The outer diameter of a slat shroud is usually $1.3D$ with 40% open area. Axial slats are expensive but generally perform better than strakes or perforated shrouds (Kumar, Sohn, & Gowda, 2008).

Spoiler plates are rectangular blades attached normal to the surface of a cylindrical member (Figure 37b). They have been found to reduce vortex excitation by nearly 70%. Spoiler plates increase forces due to drag, and, consequently, a structure with spoilers has to be designed to bear higher in-line forces (Kumar, Sohn, & Gowda, 2008).



Figure 37. Add-on devices: (a) helical strakes (b) spoiler plates (after Kumar, Sohn, & Gowda, 2008)

Another body modification that reduces VIV is a system of hemispherical bumps applied in a spiral pattern (Figure 38). The height of each protuberance ranges from 0.25 to $0.5D$, and they are radially distributed 30 to 90 degrees apart. Practical applications for bumps include chimneys in wind flow. They reduce VIV by up to 47% and reduce drag by up to 25% (Kumar, Sohn, & Gowda, 2008).

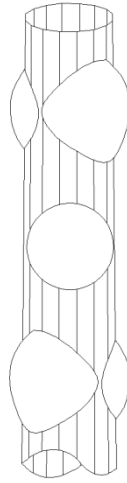


Figure 38. Smoothly curved protuberances (after Kumar, Sohn, & Gowda, 2008)

Another method for reducing vortex-induced oscillations is to attach ribbons to a member (Figure 39). Generally the ribbons have a width of 1 to $2D$, a length of 6 to $10D$, a thickness of $0.05D$, and spacing of 1 to $3D$. They are attached to a cylindrical member, 120 degrees apart, and self-adjust to the incoming flow direction. In addition to suppressing VIV, they reduce aerodynamic drag (Kumar, Sohn, & Gowda, 2008).

The authors of “The effects of drag due to ribbons attached to cylindrical pipes” propose a drag reduction and vortex suppression device that consists of three ribbons attached to a vertical pipe and spaced 120 degrees apart (Kwon, Cho, Park, & Choi, 2002). The ribbons have several advantages over helical strakes, including a simple design, ease of fabrication, low maintenance, and cost reduction. The study was conducted using a circulating water channel to test how ribbon length affects flow.

The experimental model used was a 600 mm long circular cylinder with a 50-mm diameter. Three ribbons were attached to the cylinder 120 degrees apart so that they could self-adjust to flow from any direction. Tests were performed with ribbons 75, 100, and 150 mm long. Ribbons were 500 and 600 mm wide (along the cylinder axis). The optimal ribbon length for drag reduction was 100 mm, or twice the cylinder’s diameter. Results demonstrate that a ribboned cylinder can be effective at suppressing vortex-induced vibrations when the length of ribbons is properly adjusted but also indicate that optimal ribbon size can only be determined experimentally (Kwon, Cho, Park, & Choi, 2002).

The reduction in drag is due to the fact that optimally sized ribbons suppress the formation of an organized vortex street. The ribbon add-ons are efficient, regardless of the flow direction (Kwon, Cho, Park, & Choi, 2002).

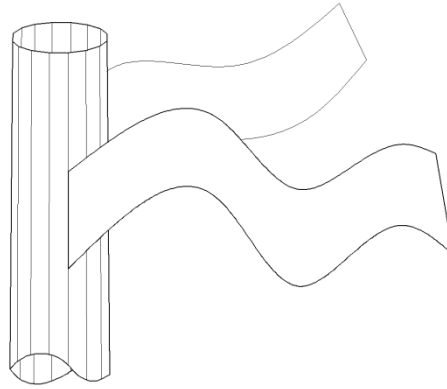


Figure 39. Ribbons (after Kumar, Sohn, & Gowda, 2008)

Vortex shedding can also be weakened and drag can be reduced by the application of surface roughness. Researchers at the University of Wyoming examined a wedge model with surface roughness conditions previously shown to reduce drag (Durgesh, 2006). The focus of the study was on identifying changes in the wake structure associated with the reduction in base drag.

The wedge model was comprised of three sections: an elliptical leading edge, a ramp section, and a base section. The surface roughness applied was sand with 2.2-mm diameter grains. The Reynolds number for the model, both with and without surface roughness, was estimated to be on the order of 500,000.

It was determined that the surface roughness caused a more organized and periodic structure in the wake, as compared with a smooth model. The more structured wake was weaker and consequently vortex-induced vibrations were lessened in the rough surfaced model (Naughton, 2009).

2.8 Tuned-Mass Dampers (TMD)

The tuned-mass damper is comprised of a small vibratory system (mass, spring, and dashpot) attached to a structure, located near its top. The system is “tuned” to the frequencies of vibration of the given structure and is designed to diminish vibrations at the natural frequencies. TMDs have been used in wind-sensitive structures such as skyscrapers and are also effective for slender towers and stacks with circular cross-section. When the tuned-mass damper is excited by harmonic (or quasi-harmonic) motions of the structure, it will vibrate in opposition to these oscillations and thus reduce the amplitude of the structure’s dynamic response (Simiu & Scanlon, 1986).

According to NCHRP Report 469, luminaire manufacturers have extensive knowledge of damping devices that lessen vibrations in light support structures (Dexter & Ricker, 2002). There are several types of mitigation devices that have been used on high-mast light poles, mounted either on the interior or exterior of the structure.

Dampers can be as simple as a rod hung inside of the pole that is free to collide with it. The factory-installed version of this damper is typically mounted at two-thirds of the height of the pole and fitted with a Teflon ring to reduce noise. It costs approximately \$10 to manufacture.

A similarly inexpensive retrofit consists of two aluminum cables placed inside a plastic tube 80 percent of the total pole height. This damper is installed by inserting the tube into the pole through the handhole and also works by impacting the inside of the pole (Dexter & Ricker, 2002).

Ball-and-chain dampers consist of a metal weight attached to a chain suspended inside the pole. The weight swings freely and impacts the inside wall of the pole and has found to be successful at damping out vibrations (Dexter & Ricker, 2002).

Stockbridge dampers (dogbone dampers) consist of a flexible shaft with a weight at each end. They are typically designed to have a frequency close to the second natural frequency of the structure. Stockbridge dampers can be mounted inside or outside the pole, which makes them a convenient retrofit (Dexter & Ricker, 2002).

Numerous tapered aluminum light poles in New Jersey were found to have significant cracking, and some of them were outfitted with dogbone dampers. Pluck tests revealed that the dampers were totally ineffective in first mode. The cracking, however, was suspected to have occurred due to the third mode of vibration, in which the dampers were probably also ineffective (Dexter & Ricker, 2002).

Despite a few cases where structures retrofitted with these damping devices have cracked or failed, in general, they are very effective.

2.9 Specifications

2.9.1 Vortex Shedding

The AASHTO *Standard Specifications for Structural Supports for Highway Signs, Luminaires and Traffic Signals* provide a method for calculating the critical wind velocity at which vortex shedding occurs for a given structure and the equivalent static pressure range for loads due to vortex shedding.

The *Specifications* recommend that vortex shedding loads be applied only to structures with less than 0.14 in/ft of taper. This suggestion was based upon the belief that most tapered structures have critical wind velocities less than 11 mph. 11 mph is the threshold velocity for vortex shedding excitation; lesser wind speeds do not provide enough energy to excite a structure. In addition, for a tapered pole, a particular wind velocity can only cause lock-in to occur over a small range of member dimensions, so vortex shedding loads are only applied to a portion of a tapered member. Therefore, the stress ranges due to vortex shedding loads on tapered structures were incorrectly thought to be insignificant (Dexter & Ricker, 2002).

Because of the criticisms of these methods cited in several publications, including *NCHRP Report 469*, the *Specifications* have recently been updated. Changes to the 2001 *Specifications* include considering higher modes of vibration of a structure than just the first natural frequency and recognizing that structures with a taper of 0.14 in/ft or greater can experience vortex induced vibrations. The critical wind velocity is directly proportional to the natural frequency of a structure, so higher modes of vibration yield higher velocities. Second and third mode vibrations have been observed to occur in tapered poles, so it is certainly valid to consider the loads caused by them. In addition, the equivalent static pressure range is

proportional to the square of the critical wind velocity. Thus, vortex shedding loads for higher modes can be significantly larger than those for first mode.

The critical wind velocity may be calculated using the equation cited in Section 2.1.7. For a tapered pole, a particular wind velocity can only cause lock-in to occur over a small range of member dimensions. Consequently, the Ontario Highway Bridge Design Code suggests that, for tapered structures, vortex shedding pressures should only be applied over the length of the member for which the cross-sectional dimension is within 10% of the critical dimension. Even so, the higher mode vortex shedding loads can be large enough to cause fatigue problems (Dexter & Ricker, 2002).

According to AASHTO, the equivalent static pressure range, P_{vs} , in psf may be calculated using the following equation:

$$P_{vs} = \frac{0.00256V_c^2 C_d I_F}{2\beta}$$

where, V_c = the critical wind velocity in mph,

C_d = the drag coefficient based on the critical wind velocity,

I_F = the importance factor (Table 6), and

β = the damping ratio (estimated at 0.005).

The $\frac{1}{2\beta}$ factor accounts for dynamic amplification at resonance, that is, when $r = \frac{\bar{\omega}}{\omega} = 1$ (i.e. when the forcing frequency is equal to the natural frequency). It is derived from the equation for the dynamic amplification factor:

$$D = \frac{1}{\sqrt{(1 - r^2)^2 + (2r\beta)^2}} = \frac{1}{2\beta}$$

Therefore, the vortex shedding loads specified by AASHTO assume a worst case scenario where the vortex shedding frequency exactly matches the natural frequency of the pole.

Table 6. Importance factors for fatigue design (Dexter & Ricker, 2002)

| Category | | Importance Factor, I_F | | | |
|----------|-----------|--------------------------|-----------------|--------------------|---------------------|
| | | Galloping | Vortex Shedding | Natural Wind Gusts | Truck-Induced Gusts |
| I | Sign | 1.0 | x | 1.0 | 1.0 |
| | Signal | 1.0 | x | 1.0 | 1.0 |
| | Luminaire | x | 1.0 | 1.0 | x |
| II | Sign | 0.72 | x | 0.85 | 0.90 |
| | Signal | 0.64 | x | 0.77 | 0.84 |
| | Luminaire | x | 0.66 | 0.74 | x |
| III | Sign | 0.43 | x | 0.69 | 0.79 |
| | Signal | 0.28 | x | 0.53 | 0.67 |
| | Luminaire | x | 0.31 | 0.48 | x |

Note: x - Structure is not susceptible to this type of loading.

The three importance categories in Table 6 are defined as follows:

Category I - Cantilever structures with a span in excess of 50 ft or high-mast towers in excess of 100 ft or structures located in areas known to have wind conditions conducive to vibrations

Category II - All structures not explicitly meeting the requirements of Categories I or III

Category III - Structures located on roads with speed limits of 35 mph or less or located such that a failure will not affect traffic

The high-mast structures considered herein are Category I as they are 120 ft tall and located in an area with wind conditions conducive to vibrations. The applicable importance factors are highlighted in Table 6.

The calculated equivalent static pressure range shall be applied transversely to the pole. For tapered poles, it is assumed to act over the length where lock-in can occur. Multiplying the pressure by the critical dimension $\pm 10\%$ yields the upper and lower values of the triangularly distributed load to be applied. When this load is resolved into point loads, the base moment and the moment at other important locations such as at weldments (such as the handhole) can be calculated.

2.9.2 Natural Wind Gusts

The AASHTO *Specifications* also provide a method for calculating equivalent static pressure range due to natural wind gusts. Since the yearly mean wind velocity for Laramie, WY is greater than 11.2 mph (Parish, 2009), the modified equation for natural wind gust pressure must be used:

$$P_{NW} = 5.2C_d \left(\frac{V_{mean}}{11.2} \right)^2 I_F$$

where, P_{NW} = equivalent static natural wind gust pressure range in psf, and

V_{mean} = the mean yearly wind velocity in mph.

The *Specifications* do not take into account the atmospheric boundary layer effect for fatigue loading; a uniform pressure is applied to the entire structure, regardless of height.

The natural wind gust pressure range shall be applied to the exposed area of all members and attachments in the horizontal direction. Designs shall consider natural wind gusts from any direction. The wind gust pressure range for design was formulated using data from an analytical report on the response of cantilevered support structures subject to random wind gust loads. The study used 11.2 mph as the upper bound of the yearly mean wind velocity, thus, the equation needs to be modified for locations where the yearly mean wind velocity is larger (American Association of State Highway and Transportation Officials, 2009).

3 THEORETICAL WORK

3.1 Modal Analysis

Modal analyses of the pole were performed using both a model built in SAP2000 and hand calculation methods.

In SAP2000, the pole was modeled in three sections (each 40 ft long) using a nonprismatic section to model the taper of each segment. A disk 8 ft in diameter (the actual diameter of the luminaire) of appropriate thickness was used to model the luminaire mass. The weight of the luminaire and lowering device was estimated to be 600 lb based on manufacturer's information. (The luminaire mass was later applied as a nodal mass and as a nodal mass with inertia, and the results were all identical.) For simplicity, a circular section was used to approximate the actual hexadecagonal cross-section of the pole. The overlap occurring at the slip joints was neglected. The base was fully fixed from rotations and translations in all directions. Each segment of the pole was divided into 4-ft sections, and deflections were obtained at 4-ft increments. A modal analysis was performed and yielded the natural frequency for each mode.

For the hand calculations, the pole was modeled in 24 5-ft segments. The hexadecagonal cross-section was considered, but the overlap at the slip joints was again neglected. In addition, the radius at the sixteen vertices was neglected since its exact value was unknown. The mass and average moment of inertia of each section were calculated using the actual dimensions of the pole and used to build mass and stiffness matrices. The mass of the luminaire was added to the top segment. These values were used to calculate the mode shapes and modal frequencies for the system.

3.1.1 Mode Shapes

The mode shapes for Modes 1-4 were determined using both methods. They agreed well with each other, and the SAP mode shapes are shown in Figure 40.

The information from the modes shapes was used to determine where to locate the accelerometers. Since Mode 1 vibrations should be apparent at any location along the length of the pole, the accelerometers were situated to pick up Mode 2 and 3 oscillations. The maximum deflection for Mode 2 occurs at approximately 75 ft, however, due to logistical considerations, an accelerometer could not initially be placed at this location. Instead, the accelerometer was placed as high as possible at 56 ft, a location where Mode 2 and Mode 3 vibrations are both significant. The lower antinode for Mode 3 occurs at approximately 46 ft, so the second accelerometer was mounted near this location (41 ft).

When comparing the mode shapes from SAP2000 and the hand calculations, deflections were normalized so that the maximum value for each mode was 1.

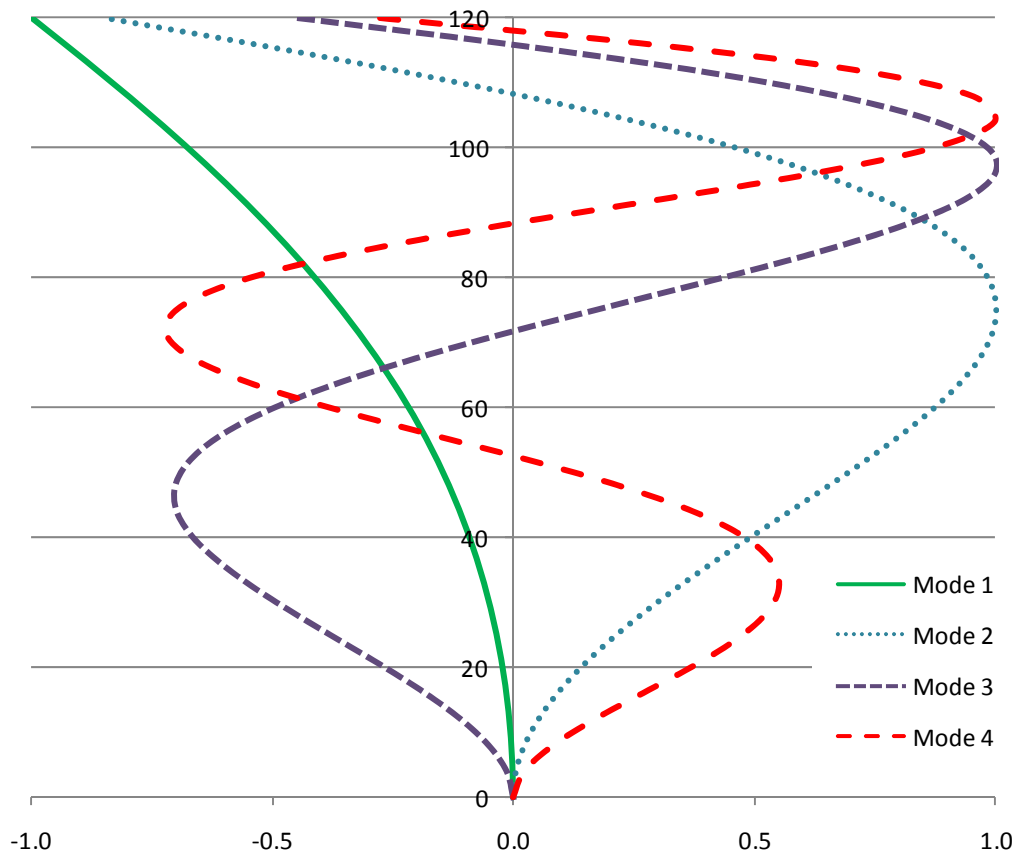


Figure 40. Mode shapes with luminaire mass

3.1.2 Natural Frequency

The natural periods and frequencies for the first four modes were calculated using the SAP2000 model previously described. These values are shown in Table 7. The sampling rate required for data acquisition was determined using the first four modal frequencies. A minimum sampling rate of ten times the highest modal frequency was required to avoid aliasing. The data acquisition system allows for sampling rates that are powers of two starting at 32 Hz. Consequently, a sampling rate of 128 Hz was chosen to capture the first four modes of vibration.

Table 7. Values from SAP2000

| Mode | 1 | 2 | 3 | 4 |
|------------------------|-------|-------|-------|-------|
| Period (s) | 2.60 | 0.609 | 0.237 | 0.121 |
| Natural Frequency (Hz) | 0.385 | 1.64 | 4.22 | 8.27 |

3.2 Critical Velocity

Critical velocities for Modes 1, 2, 3, and 4 were calculated according to the AASHTO *Specifications*. Since the pole is tapered, a critical dimension needed to be determined to

calculate the critical velocity. The antinode locations were taken to be the critical diameters for each mode since maximum displacements occur at these locations.

Table 8. Critical velocities

| Location | | Height | Critical Diameter | | Critical Velocity at 33 ft (mph) | | | |
|----------|---------------------|--------|-------------------|------|----------------------------------|--------|--------|--------|
| | | ft | ft | in | Mode 1 | Mode 2 | Mode 3 | Mode 4 |
| 1 | Mode 4 - Antinode 1 | 32 | 1.57 | 18.8 | | | | 53.5 |
| 2 | Mode 3 - Antinode 1 | 46 | 1.41 | 16.9 | | | 22.9 | |
| 3 | Mode 4 - Antinode 2 | 72 | 1.13 | 13.5 | | | | 32.4 |
| 4 | Mode 2 - Antinode 1 | 75 | 1.09 | 13.1 | | 6.2 | | |
| 5 | Mode 3 - Antinode 2 | 97 | 0.85 | 10.2 | | | 11.8 | |
| 6 | Mode 4 - Antinode 3 | 104 | 0.77 | 9.3 | | | | 20.6 |
| 7 | Mode 1 - Antinode 1 | 120 | 0.60 | 7.18 | 0.72 | | | |

3.3 Important Dimensionless Variables

3.3.1 Reynolds Number

The Reynolds number varies with both the wind velocity and the diameter of the object in consideration. Since the pole is tapered, the Reynolds number varies along its length. The values in Table 9 are given for the Mode 3 critical diameter of the pole, 0.85 ft (the flat-to-flat distance at the location of the upper antinode for Mode 3). The highlighted value is the Reynolds number for the critical diameter and critical velocity.

Laramie’s elevation was considered in the calculation, so the density of air was taken to be 0.058 pcf, approximately 24% less than the density at sea level. This, in turn, reduced the Reynolds number by the same percentage.

Table 9. Reynolds numbers for high-mast poles at critical diameter

| U (mph) | 5 | 10 | 12 | 15 | 20 | 25 | 30 |
|---------|--------|--------|--------|--------|---------|---------|---------|
| Re | 30,000 | 61,000 | 73,000 | 91,000 | 120,000 | 150,000 | 180,000 |

For all wind speeds between 1 and 25 mph at all diameters of the pole, the Reynolds number is between 300 and 3.5×10^5 , the range in which vortex shedding is strong and periodic (Phares, Sarkar, Wipf, & Chang, 2007). At higher wind speeds, the upper portion of the pole is still susceptible to vortex shedding.

3.3.2 Strouhal Number

The Strouhal number may be calculated using the natural frequency of the critical mode, the critical diameter, and the observed critical velocity. Since Mode 3 has the lowest damping ratio, it is the critical mode, and the critical diameter has been assumed to be the flat-to-flat distance at the upper Mode 3 antinode. Once the pole has locked in, the velocity can fluctuate between 10 and 19 mph with amplified accelerations, but the critical velocity has been found to be approximately 12 mph.

$$S = \frac{f_s D}{U} = \frac{3.8 \text{ Hz} * 0.85 \text{ ft}}{12 \text{ mph}} = 0.18$$

According to AASHTO, the Strouhal number for circular sections is 0.18 and for multi-sided sections is 0.15. AASHTO, however, groups all “multi-sided” sections together, making no distinction between shapes with different numbers of sides and not considering the corner radius. From the data, it is apparent that the 16-sided high-mast pole with a significant radius at each corner is closer to a circular section than it is to a generic “multi-sided” section.

3.3.3 Scruton Number

The Scruton number is dependent upon the mass per unit length of the body, the critical damping ratio, the flow density, and the crosswind dimension of the body. Since the subject high-mast pole is tapered, the average mass per unit length and average cross-section of the pole are used for the calculation. The critical damping ratio is that of Mode 3 and was determined to be 0.1% for the structure. The flow density is adjusted for the elevation and is taken to be 0.058 pcf. Using these values, the Scruton number can be calculated as follows.

$$S_c = \frac{4\pi m \zeta}{\rho D^2} = \frac{4\pi * 43.73 \frac{\text{lb}}{\text{ft}} * 0.001}{0.058 \frac{\text{lb}}{\text{ft}^3} * (1.26 \text{ ft})^2} = 6.0$$

Since $S_c < 10$, it is likely that the structure is susceptible to high amplitude vibrations due to vortex shedding.

4 EXPERIMENTAL WORK

4.1 Data Analysis

Matlab scripts were written for all data analysis operations.

4.1.1 Alongwind and Crosswind

The wind direction, θ , was used to transform north-south (NS) and east-west (EW) acceleration and strain data into alongwind (AW) and crosswind (CW) measurements for analysis (Figure 41, Figure 42). The equation below was used to rotate values θ degrees clockwise.

$$\begin{bmatrix} \varepsilon_{AW} \\ \varepsilon_{CW} \end{bmatrix} = \begin{bmatrix} \cos \theta & \sin \theta \\ -\sin \theta & \cos \theta \end{bmatrix} \begin{bmatrix} \varepsilon_{NS} \\ \varepsilon_{EW} \end{bmatrix}$$

Figure 41. Transformation matrix equation

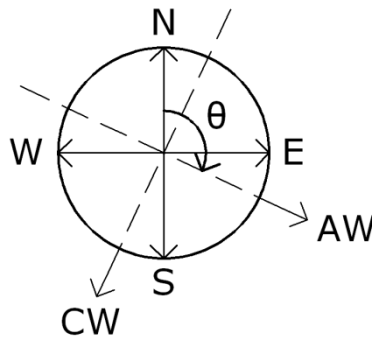


Figure 42. Transformation from NS, EW to AW, CW

4.1.2 Fast Fourier Transform

The Fast Fourier Transform (FFT) was used to transform data from the time domain into the frequency domain. This analysis allowed for the determination of the natural frequencies of the structure. Figure 43 shows an example of an FFT analysis of ambient wind data, where the first four natural frequencies are apparent.

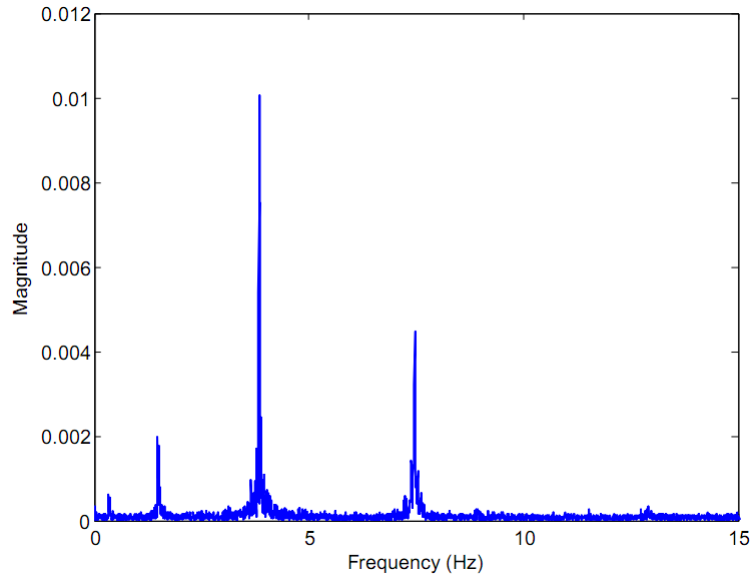


Figure 43. FFT amplitude spectrum showing first four modal frequencies

An FFT analysis also provides the magnitude of vibration at each frequency, which allows for determination of the dominant frequency (or frequencies) of vibration. Figure 44 demonstrates an instance of Mode 3 lock-in. For the purpose of our analysis, “lock-in” was defined to be when the amplitude of acceleration at a particular modal frequency was at least ten times greater than the amplitude at any other frequency.

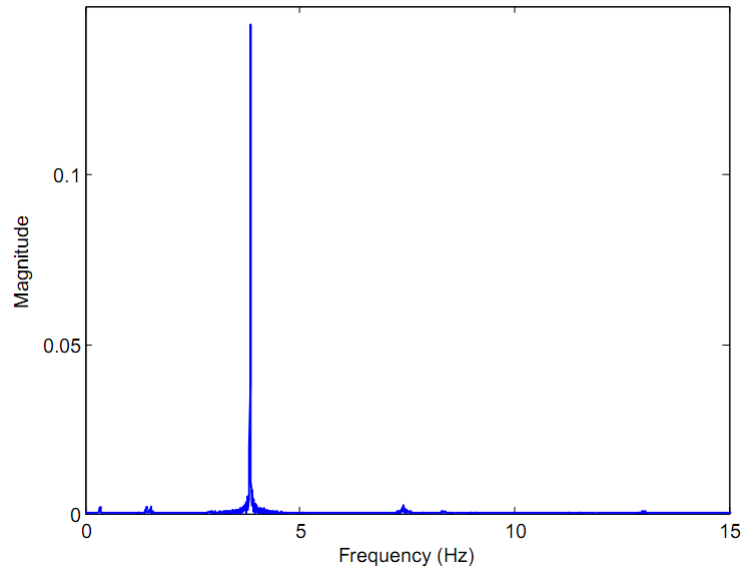


Figure 44. FFT amplitude spectrum showing Mode 3 lock-in at 3.8 Hz

4.1.3 Prony Method

Prony analysis uses a sum of damped sinusoids to approximate real data from a uniformly sampled signal (Pierre, 2009).

For example, if there is a single damped sinusoid, $f(t) = Ae^{\sigma t} \cos(\omega t + \theta)$, using Euler's Equation, it may be rewritten as $f(t) = \frac{A}{2} e^{j\theta} e^{(\sigma+j\omega)t} + \frac{A}{2} e^{-j\theta} e^{(\sigma-j\omega)t}$.

By letting $s_1 = \sigma + j\omega$ and $s_2 = \sigma - j\omega$, and $C_1 = \frac{A}{2} e^{j\theta}$ and $C_2 = \frac{A}{2} e^{-j\theta}$, and $\mu_i = e^{s_i T}$ where T is the sampling period, then:

$$f(k) = C_1 \mu_1^k + C_2 \mu_2^k$$

Prony analysis provides an estimate of the frequency, amplitude, phase, and damping of each component of the signal. There are three primary steps to the Prony Method to solve for estimates of the C 's and μ 's:

1. Step one: Solve the least squares problem

$$\begin{bmatrix} f(2) \\ f(3) \\ \vdots \\ f(N-1) \end{bmatrix} = \begin{bmatrix} f(1) & f(0) \\ f(2) & f(1) \\ \vdots & \vdots \\ f(N-2) & f(N-3) \end{bmatrix} \begin{bmatrix} a_1 \\ a_2 \end{bmatrix}$$

2. Step two: Root the characteristic polynomial

$$\mu^2 - a_1 \mu - a_2 = (\mu - \mu_1)(\mu - \mu_2)$$

3. Step three: Solve the least squares problem

$$\begin{bmatrix} f(0) \\ f(1) \\ f(2) \\ \vdots \\ f(N-1) \end{bmatrix} = \begin{bmatrix} 1 & 1 \\ \mu_1 & \mu_2 \\ \mu_1^2 & \mu_2^2 \\ \vdots & \vdots \\ \mu_1^{(N-1)} & \mu_2^{(N-1)} \end{bmatrix} \begin{bmatrix} C_1 \\ C_2 \end{bmatrix}$$

From the estimates of the C 's and μ 's, estimates can be found for A , σ , ω , and θ as:

$$A = 2|C_1|,$$

$$s = \frac{1}{T} \ln(\mu),$$

$$\sigma = \text{real}\{s\},$$

$$\omega = \text{imag}\{s\},$$

$$f = \frac{\omega}{2\pi}, \text{ and}$$

$$\theta = \text{angle}(C_1).$$

The damping ratio is:

$$\zeta = -\sigma / \sqrt{\sigma^2 + \omega^2}$$

For more than one damped sinusoid, increase the dimensions of the matrices in Steps 1-3 above. To help compensate for noise, over estimate the number of components, then estimate the components of interest as the appropriate subset.

The Prony Method was used to extract damping ratios from the pluck test data, as well as to confirm the natural frequencies determined using FFT. Figure 45 shows measured acceleration data logged during a pluck test, and the Prony approximation reconstructed using only the components of interest.

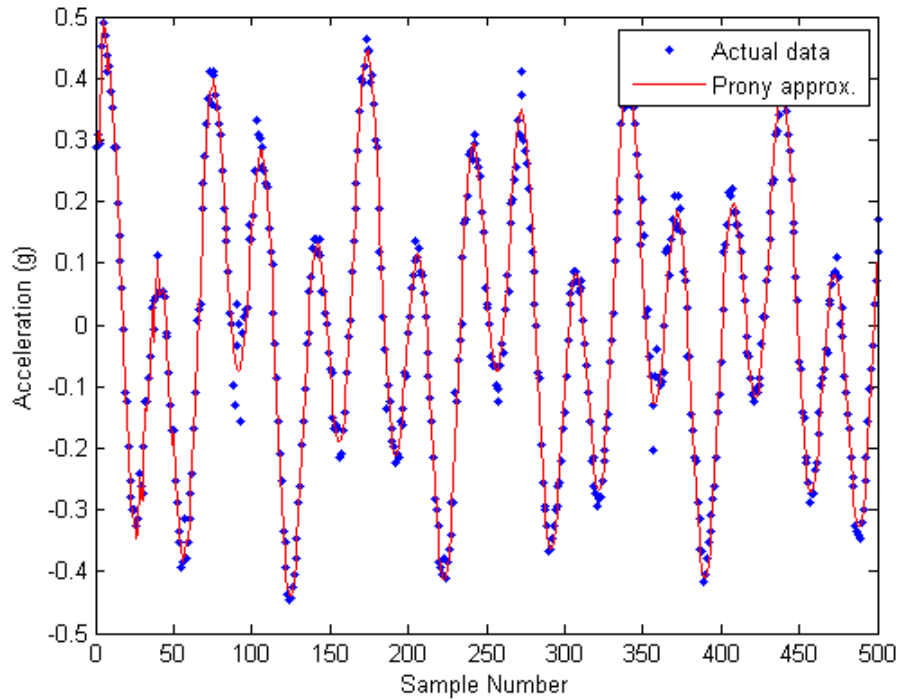


Figure 45. Sample Prony approximation of acceleration data

4.2 Deflection Calculations

Maximum deflections at the height of the accelerometers were calculated using maximum accelerations, a_{max} , (in g) and modal frequencies, f_n , (in Hz) when the pole was in lock-in. The following equation was used:

$$d_{max} = \frac{a_{max}}{(2\pi f_n)^2}$$

The mode shapes were then used to calculate maximum deflections for the pole. For Mode 3, maximum deflections occurred at a height of 97 ft. To determine deflections at 97 ft from the deflections at 41 ft, the following equation was used:

$$d_{97ft} = \frac{d_{41ft}}{0.68}$$

To determine deflections at 97 ft from the deflections at 56 ft, the following equation was used:

$$d_{97ft} = \frac{d_{56ft}}{0.6}$$

4.3 Mode Shapes

The mode shape for Mode 3 was verified using acceleration data from Pole 3. According to the mode shapes determined using SAP2000 and hand calculations, for Mode 3: $\frac{d_{56ft}}{0.6} = \frac{d_{41ft}}{0.68}$.

Therefore, $\frac{0.68}{0.6} = \frac{d_{41ft}}{d_{56ft}} = 1.13$ and $\frac{a_{41ft}}{a_{56ft}} = 1.13$. Figure 46 plots crosswind acceleration data from Pole 3 taken from accelerometers located at 41 versus crosswind accelerations at 56 ft. The data are from when the pole was in Mode 3 lock-in. According to the plot, $\frac{a_{41ft}}{a_{56ft}} = 1.1679$. The ratio of accelerations at the two heights given by the data is 3% higher than that given by the SAP2000 analysis. Therefore, it can be assumed that the SAP2000 model gives a good approximation of the Mode 3 shape.

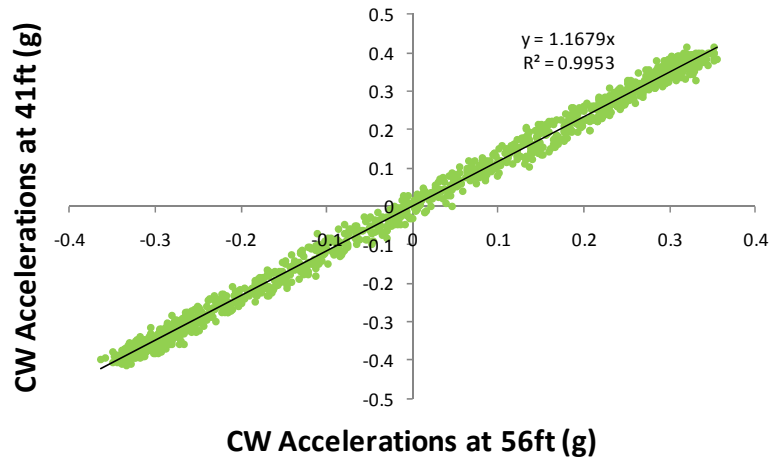


Figure 46. 41 ft Accelerations vs. 56 ft accelerations for Pole 3 in Mode 3 lock-in

4.4 Pluck Test

The natural frequencies and damping ratios for the high-mast light poles were determined using several pluck tests performed on Pole 3 (Figure 47). Oscillations were induced by attaching a steel cable rated at 2000 lb to the structure at a predetermined height and pulling it with a vehicle so that large (yet elastic) deformation states were achieved. The numerical model created with SAP2000 was used to determine where to attach the cable to the pole in order to suitably excite it. A steel link (Figure 48) was used to connect the cable to another short length of cable attached to the vehicle. The cable was released when the link broke, and acceleration and strain data were logged with two triaxial accelerometers and four uniaxial strain gauges.

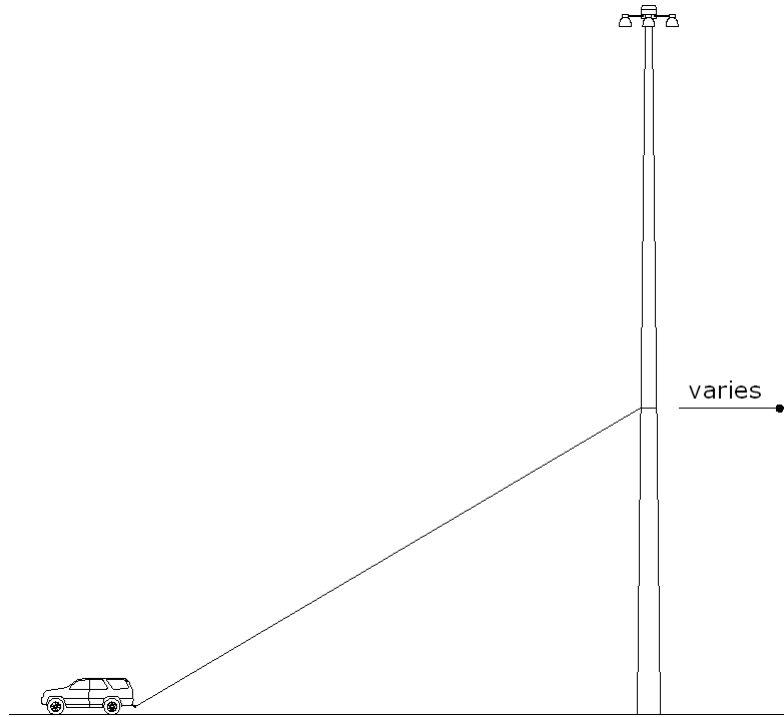


Figure 47. Pluck test setup



Figure 48. Steel link

4.5 Traffic Vibrations

The initial assumption for this project was that two high-mast poles with identical geometry and located less than 600 ft apart in similarly open terrain would be subjected to approximately the same wind conditions and consequently would have similar dynamic responses. Preliminary acceleration measurements proved this assumption to be false. While

Pole 3 achieved Mode 3 (the critical mode) lock-in on twenty occasions (out of thirty-three sets of data recorded), Pole 4 was never observed to lock-in.

The only significant difference between the locations of the two poles is the proximity to the interstate highway. Pole 3 is located in a grassy field along the on-ramp, while Pole 4 is situated approximately 30 ft from the westbound travel lane of the highway (Figure 3, Figure 49). I-80 has heavy truck traffic traveling at 75 mph day and night. According to WYDOT figures, on an average day an estimated 7000 trucks cross Wyoming on I-80 (Parsons Brinckerhoff in association with PB Consult, 2008).

It was hypothesized that vibrations from passing vehicles were exciting the structure at frequencies different from the vortex shedding frequencies and preventing it from locking in.

Three uniaxial BDI accelerometers were installed on Pole 4 to determine the effect of traffic-induced vibrations. Two accelerometers were located at 18 ft high and oriented in north-south and east-west directions. The third accelerometer was mounted on the pole's base plate to record any vertical acceleration. Data were recorded under three wind conditions: calm, a mean wind speed of 7.1 mph (near Mode 2 critical velocity), and a mean wind speed of 12.1 mph (near Mode 3 critical velocity).



Figure 49. Truck traffic near Pole 4

4.5.1 Ground Vibrations and Airborne Vibrations

Further work was done to determine whether the vibrations were transmitted through the ground, the air, or both. Initially, an accelerometer located at 18 ft in a north-south orientation and a second mounted on the concrete foundation (also with a north-south orientation) were

used. Since the response of the pole and the foundation are coupled, lateral acceleration measurements were also taken at the 18 ft position as well as at ground level on a 36 in long, 24 in wide, and 3 in thick concrete slab nearby the pole.

4.6 Retrofits

Possible retrofits for high-mast structures fall into two categories: aerodynamic dampers that are applied to the surface of the pole and change the structure's aerodynamic characteristics, and tuned-mass dampers that oppose the motion of the pole and need only be located at one point (typically the top). Aerodynamic dampers have the benefit of preventing the flow separation that causes vortex shedding and therefore prevent vibrations in all modes. Tuned-mass dampers can only be tuned to one particular frequency and consequently will only prevent vibrations in one mode. This work is focused solely on aerodynamic retrofits.

4.6.1 Aerodynamic Dampers

The literature discusses numerous types of aerodynamic dampers that are currently being used, primarily on metal chimneys and in underwater applications. Several retrofits were tested for their ability to prevent vortex-induced vibrations in a high-mast light pole.

The dampers were selected for ease of fabrication and based on physical limitations in attaching them to the pole. Since the retrofits needed to be applied in the area of the upper antinode for Mode 3 (located at 97 ft), a 125 ft boom lift was rented for their installation. The lift rental was approximately \$1500 per day, significantly more costly than the materials required for the construction of the retrofits, given in Table 10. In addition, because of the soft soil conditions on the site, the lift could only be used during cold winter months when the ground was frozen solid.

Table 10. Retrofit costs

| Retrofit | Cost |
|-------------------|-------------|
| Ribbons | \$23 |
| Helical Strakes | \$98 |
| Perforated Shroud | \$81 |
| Surface Roughness | \$189 |

4.6.1.1 Ribbons

The ribbon dampers (Figure 50) were designed using the guidelines provided in *Passive Control of Vortex-Induced Vibrations: An Overview* (Kumar, Sohn, & Gowda, 2008). Since the pole is tapered, the average diameter of the top section (10 in) was used to determine ribbon dimensions. The length was recommended to be six to ten times the diameter, so a length a 5 ft was used. The suggested width was one to two times the diameter; thus a width of 11 in was

used. The spacing of the ribbons was selected to be 3 ft. The material used is a woven plastic with a ten by ten weave per square inch and a thickness of 5.1 mil.

The ribbons were attached to strings of heavy duty twisted nylon twine using strips of duct tape. Ten ribbons were evenly spaced along the first 40 ft of cord, and an additional length of cord was provided so that it could be attached to an accessible portion of the pole when the luminaire was at the top. Three strings of ten ribbons each were fastened to the luminaire ring, separated by 120°. The luminaire was raised, and three cords were rotated 360° to prevent them from separating from the pole. The cords were then tightly secured to the pole at a height of 56 ft.



Figure 50. Ribbon retrofit on top 40 ft of high-mast pole

4.6.1.2 Helical Strakes

Helical strakes (Figure 51) were created by wrapping three rubber hoses around the pole in a spiral pattern. Three rubber hoses 16 ft in length with a 1 in outer diameter were secured to the pole at 105 ft spaced 120° apart from each other. The hoses were each wrapped around the pole once to achieve a pitch of approximately 15 times the flat-to-flat distance of the pole, and the lower ends were attached to the pole at a height of 89 ft. This retrofit covers the length of the pole with diameters in the range of the critical diameter $\pm 10\%$.

Rubber hose was selected for the strakes because of its ability to compress and then regain its original shape. Its elastic properties would allow the lowering device to easily pass over the retrofit, if necessary.



Figure 51. Helical strakes installed on high-mast pole

4.6.1.3 Perforated Shroud

The design of the perforated shroud is roughly based upon guidelines given in *Passive Control of Vortex-Induced Vibrations: An Overview* (Kumar, Sohn, & Gowda, 2008). The material is a rigid high density polyethylene net with 0.275 in square holes. The open area of the HDPE net is 45% of the total area. The shroud is 16 ft long and covers the pole from a height of 89 ft to 105 ft. This covers the length of the pole with diameters in the range of the critical diameter $\pm 10\%$. For constructability, the shroud was formed into cylinders in 48 in strips on site. The cylinders decrease in diameter to match the taper of the pole. Each segment of the shroud has a diameter that is 1.25 times the average diameter of the section of the pole that it covers. Table 11 gives the circumference of each segment of the perforated shroud.

A 125 ft boom lift was required for the installation of the perforated shroud. Figure 52 shows the installation and the completed retrofit.

Table 11. Perforated shroud specifications

| Height (ft) | C _{pole} (in) | C _{shroud} (in) |
|-------------|------------------------|--------------------------|
| 91 | 33.8 | 42 |
| 95 | 32.0 | 40 |
| 99 | 30.3 | 38 |
| 103 | 28.5 | 36 |



Figure 52. Perforated shroud installed on high-mast pole

4.6.1.4 Surface Roughness

Increased surface roughness has been observed to weaken vortex-induced vibrations; however, there are no available studies upon which to base the use of surface roughness for aerodynamic damping of a high-mast pole.

The use of surface roughness is appealing for this application as it provides a simple solution that could either be used as a retrofit or become part of the manufacturing process for new high-mast poles. Since it requires only the application of a texture to the pole's surface, it does not interfere with the operation of the luminaire's lowering device. If incorporated into the design of the pole prior to construction, this damper could simply be a knurled pattern rolled into the steel at the mill or a coating sprayed on after manufacturing.

The subject high-mast light pole was sheathed in a rubber floor covering (Figure 53). The material is 0.125 in thick with a raised diamond pattern. As shown in Figure 54, the base material is 0.0625 in thick, and the diamonds have a height of 0.0625 in and measure 0.25 in along the diagonal. The material was adhered to the pole with a double-sided tape, and all-weather cable ties were attached at the top and bottom to further secure it. The textured area is 16 ft long and covers the pole from 89 ft to 105 ft (Figure 55) in order to cover the length of the pole with diameters in the range of the critical diameter $\pm 10\%$.

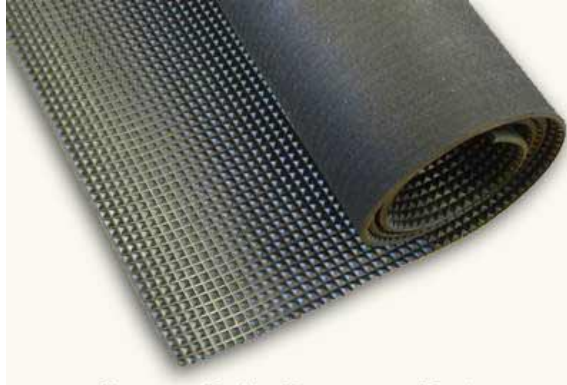


Figure 53. Diamond-textured rubber material

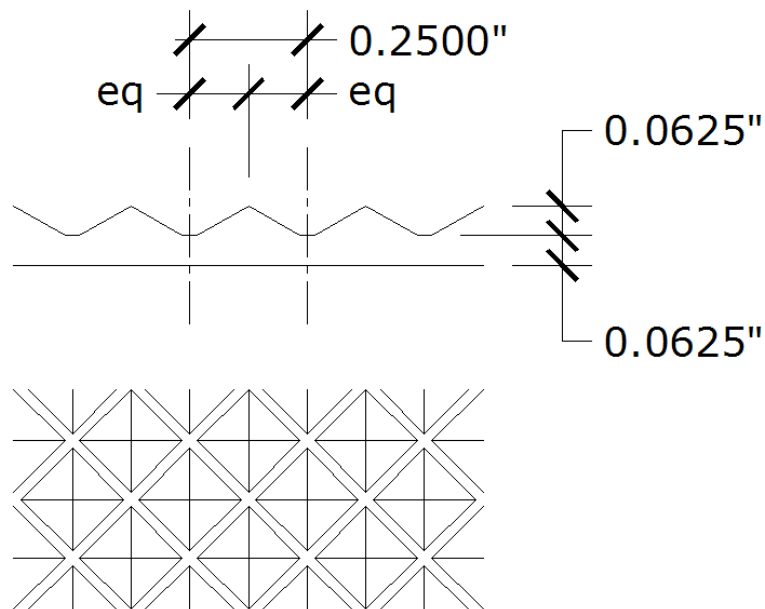


Figure 54. Detail of surface roughness material



Figure 55. Surface roughness installed on high-mast pole

4.6.2 Advantages and Disadvantages

Many aerodynamic damper retrofits are relatively easy and inexpensive to fabricate. They are designed to prevent flow separation and vortex formation, which eliminates excitation due to vortex shedding. Since the devices weaken or prevent vortex shedding, they do not need to be “tuned” to a particular natural frequency.

While some dampers decrease drag, an unfortunate side effect of others is that they can increase drag on the pole. When using such aerodynamic dampers the base connection and foundation may need to increase in size. For these types of structures, however, fatigue typically controls the tube size and weld details.

In addition, since aerodynamic dampers must be located along the length of the high-mast pole, they may interfere with the operation of the lowering device. Even if they are oriented such that the wheels on the lowering device avoid them, the lowering ring sometimes behaves erratically and may rotate as the light fixture is lowered down the pole. This could result in the damage of either the retrofit or the lowering device itself.

If an in-service pole is to be retrofitted with aerodynamic dampers, there is additional difficulty and expense associated with attaching them to the pole. However, some dampers could easily be incorporated into the design and manufacturing process of high-mast poles.

5 RESULTS

5.1 Dynamic Characteristics

5.1.1 Natural Frequencies

Fast Fourier Transform analyses were performed with the strain and acceleration data acquired from the pluck test (Figure 56) to determine the first four natural frequencies. Table 12 shows the natural frequencies derived from the pluck test data (which also agree with modal frequencies found by performing FFT analysis of other pole data) and those determined by analyzing a numerical model. The frequencies determined by FFT analysis match those found using the Prony method and were consistent throughout all testing.

The SAP2000 frequencies are all approximately ten percent higher than the natural frequencies determined using the pole data. This indicates that the SAP model is “stiffer” than the actual structure. The higher stiffness may be due to the fact that the base of the SAP model was fully fixed, whereas in the real structure some rotation can occur at the base.

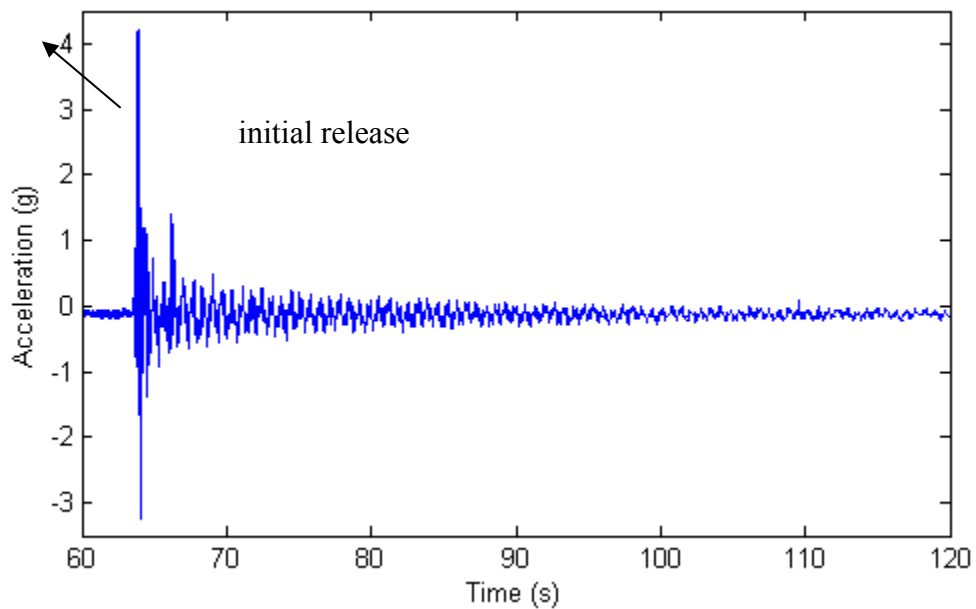


Figure 56. Pluck test acceleration data

Table 12. Natural frequencies

| Mode | 1 | 2 | 3 | 4 |
|--------------------------|-------|------|------|------|
| SAP Natural Freq (Hz) | 0.385 | 1.64 | 4.22 | 8.27 |
| Actual Natural Freq (Hz) | 0.35 | 1.5 | 3.8 | 7.5 |
| % Difference | 9.0% | 8.6% | 9.9% | 9.3% |

5.1.2 Damping Ratios

Prony analysis was performed on the acceleration and strain data collected during the pluck test in order to determine the first three damping ratios of the structure. (Mode 4 was not sufficiently excited to allow for the determination of the fourth modal damping ratio.)

Table 13. Damping ratios

| Mode | 1 | 2 | 3 |
|--------------------|-----|-----|-----|
| Damping Ratios (%) | 0.5 | 0.3 | 0.1 |

Prony analysis assumes linear damping. Since the pole has nonlinear damping, values determined using Prony varied depending on what part of a data set was being examined. When Prony analysis was performed on data collected soon after the cable was released the damping values were larger than those calculated from data collected after the vibrations had lessened. The damping was higher when the oscillations were larger presumably because of aerodynamic effects.

The values taken to be the damping ratios for the structure (given in Table 13) were determined from acceleration data in the range of accelerations observed when the pole was in lock-in.

5.2 Unretrofitted Pole Behavior

Thirty-three sets of data were logged with the unretrofitted pole (Pole 3) at mean wind speeds varying from 2.7 to 19 mph. Twenty of the 33 data sets were found to contain one or more instances of Mode 3 lock-in. One data set was observed to contain a case of Mode 2 lock-in.

It is important to note a significant limitation of the data acquisition system. Data were not collected continuously, but rather were collected for discrete time periods (typically 8.5 min long). The main focus of this research is Mode 3 vibrations, since the subject pole has the lowest damping in third mode and also because the calculated critical velocity for Mode 3 is very near the mean wind speed for Laramie. Hence, the highest amplitude vibrations the pole experienced are merely the highest that happened to be recorded and likely do not reflect the highest accelerations the unretrofitted pole underwent during the three month period during which data were collected.

Figure 57 plots the maximum acceleration for a 30-second window of time versus the mean wind speed for the same time period for all of the data collected from the unretrofitted pole. A 30-s time frame was used to provide a sufficient number of data points while taking into account the fact that the pole's behavior is dependent upon the trend in wind speed and not the instantaneous velocity.

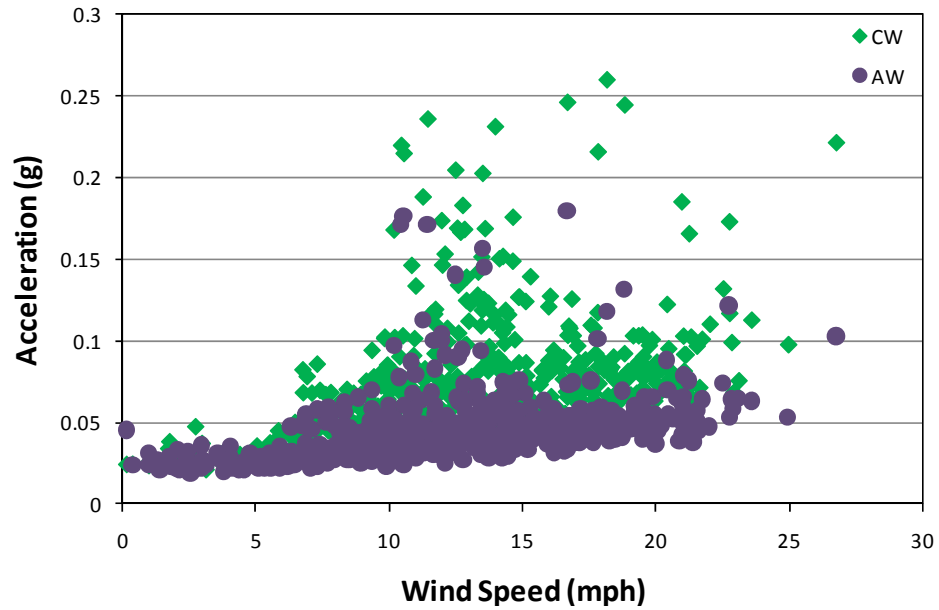


Figure 57. Maximum acceleration vs. 30s mean wind speed

Figure 58 plots the same crosswind data as Figure 57 but divides the wind speed into 2-mph bins and shows the average of the 30s maximum accelerations with error bars. This analysis reveals that many of the 30s maximum accelerations in the Mode 3 lock-in range are not amplified, which causes the mean to be relatively low (mostly less than 0.1g), but the standard deviation is high because of the instances of amplified oscillations.

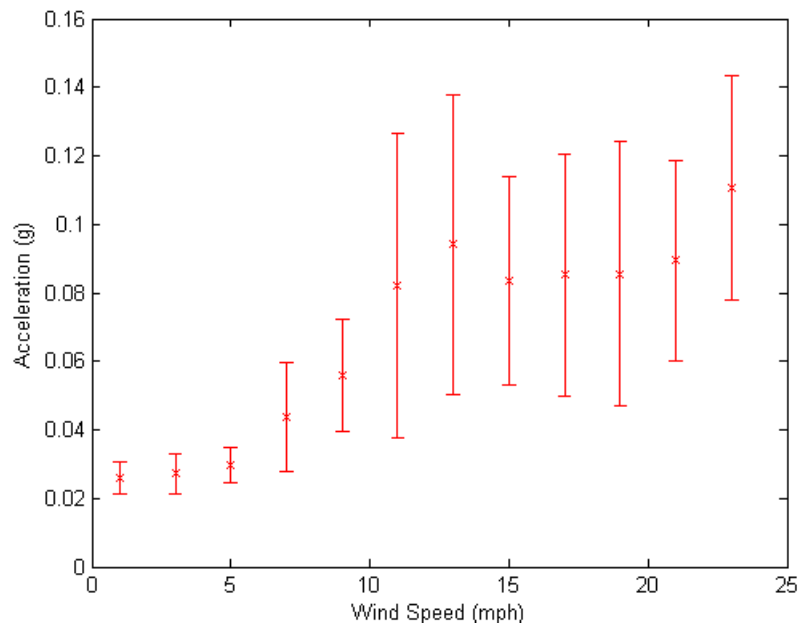


Figure 58. Average maximum crosswind acceleration vs. 30s mean wind speed

Using FFT analysis of the data, Mode 3 lock-in was determined to occur at a wide range of wind speeds between 10.4 and 18.8 mph. (The theoretical critical velocity for Mode 3 was calculated to be 11.8 mph at a height of 33 ft.) The maximum acceleration observed for the unretrofitted pole was 0.26 g and occurred at a 30s mean wind speed of 18.1 mph (6.3 mph higher than the calculated critical velocity).

The deflection corresponding to the maximum acceleration is 0.18 in at the height of the accelerometer (56 ft). The mode shapes were used to determine that the maximum deflection for the pole (at the upper antinode for Mode 3) is 0.29 in.

Strain data corresponding to the maximum oscillations observed in the unretrofitted pole were not available due to a malfunction of the strain channels in the V-link node.

A one-minute record of wind and acceleration data containing the largest acceleration observed for the unretrofitted pole is provided in Figure 59 - Figure 61 below. The mean wind speed is 18.7 mph. Note the relatively constant amplitude oscillations that occur for the entire one minute time frame, despite the significant fluctuations in wind speed. Also, note the relatively constant wind direction.

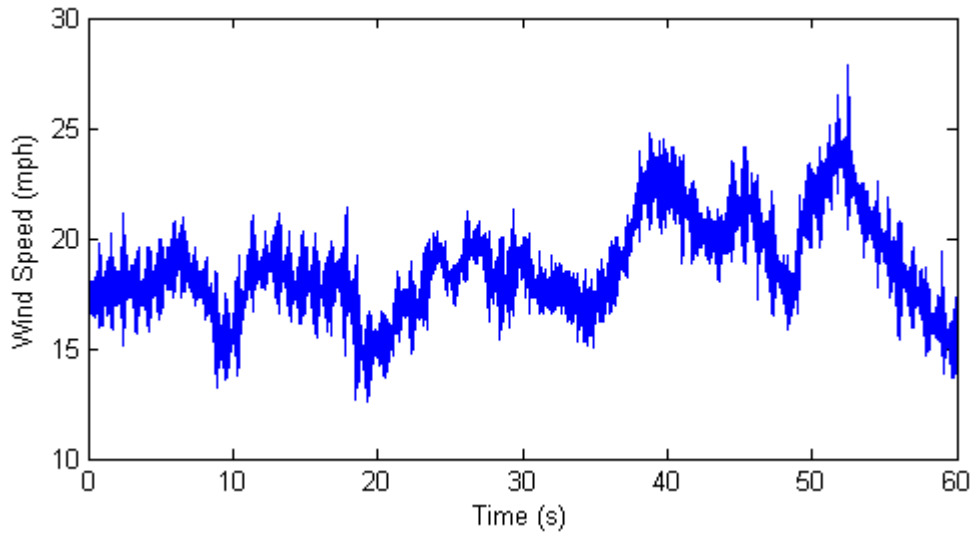


Figure 59. Wind speed vs. time

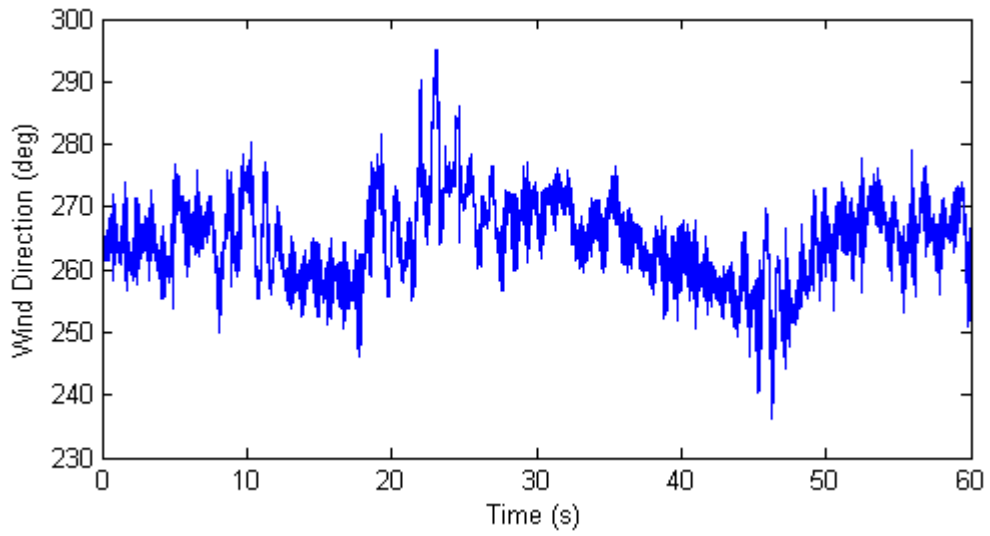


Figure 60. Wind direction vs. time

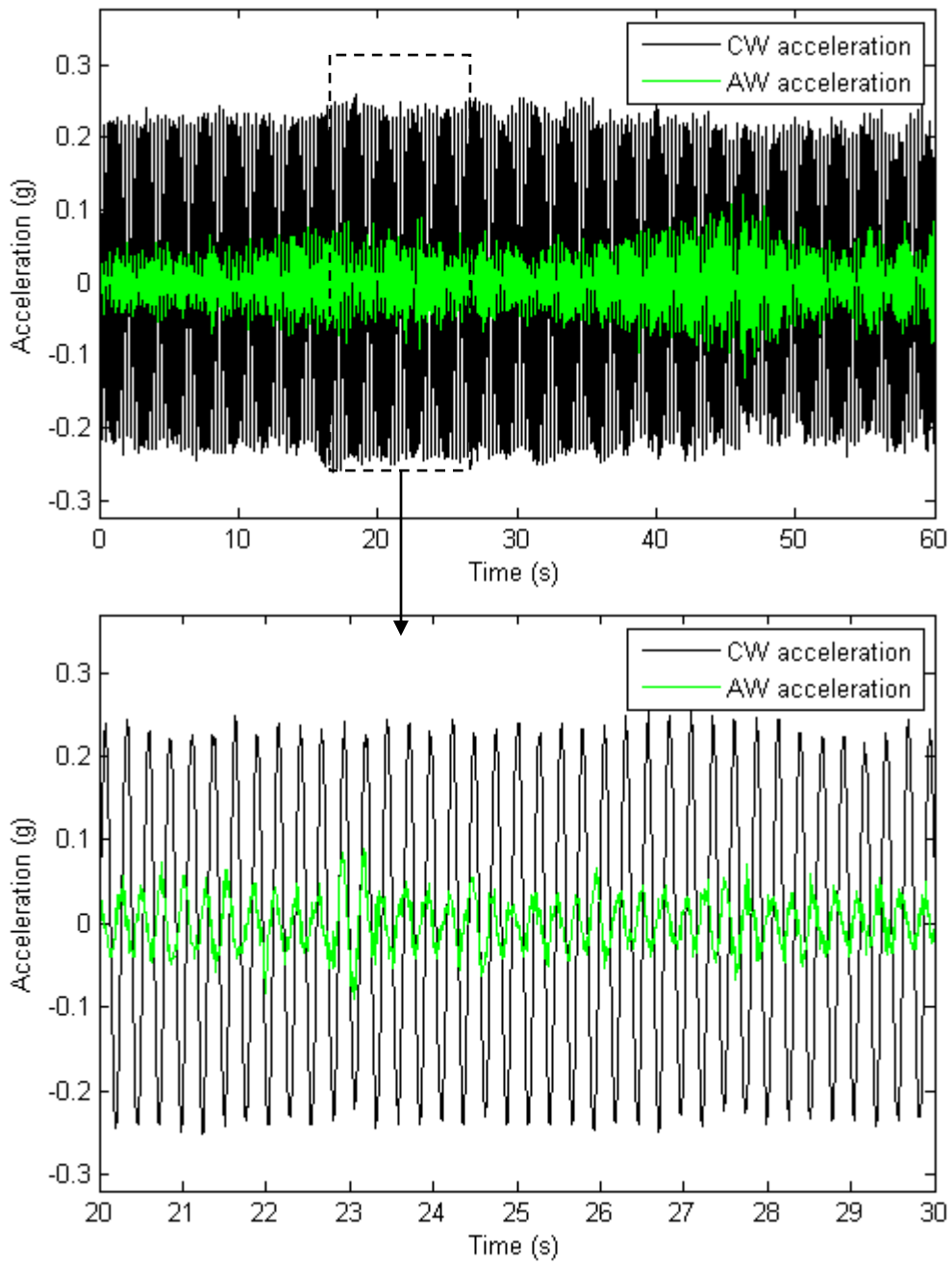


Figure 61. Acceleration vs. time at a mean wind speed of 18.7 mph (Node 464)

(a) (b)

Figure 62 shows the amplitude spectrum for the one minute of data. Note that the high-mast pole is vibrating at 3.8 Hz in both the crosswind and the alongwind directions.

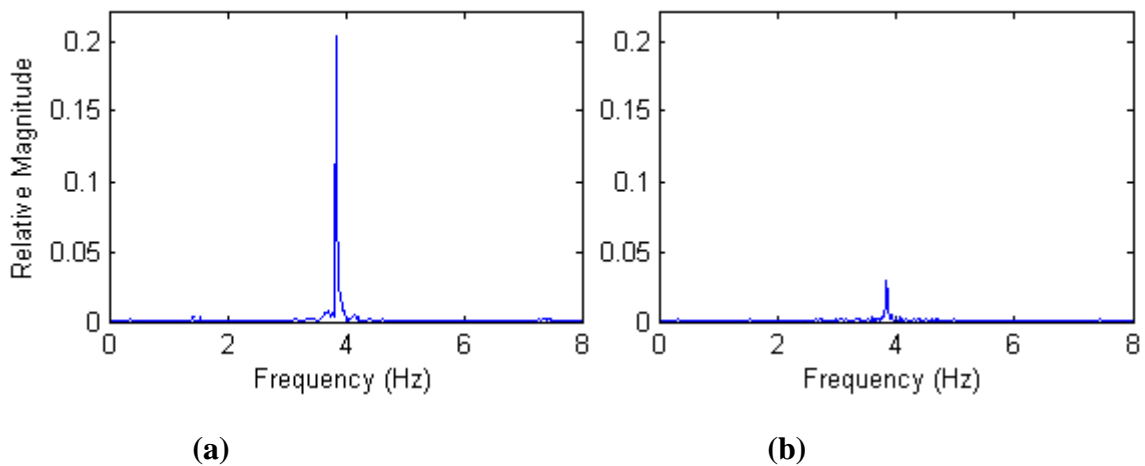


Figure 62. FFT of (a) crosswind and (b) alongwind accelerations at a mean wind speed of 18.7 mph

5.3 Retrofits

Pole 3 was retrofitted with four different damping devices, and its response was recorded under a range of wind conditions.

5.3.1 Ribbons

Only two sets of data were logged with the ribbon retrofit on the pole at mean wind speeds of approximately 10 mph, but both contained instances of Mode 3 lock-in. A limited amount of data were collected with this retrofit as the strings of ribbons separated from the pole soon after their installation, and consequently the retrofit was not configured according to its design.

A one minute record of wind and acceleration data containing the largest acceleration observed for the pole retrofitted with ribbons (0.17 g) is provided in Figure 63 - Figure 65 below. The mean wind speed is 11.9 mph.

The deflection corresponding to the maximum acceleration is 0.12 in at the height of the accelerometer (41 ft). The mode shapes were used to determine that the maximum deflection for the pole (at the upper antinode for Mode 3) is 0.17 in.

FFT analysis of the wind data (Figure 66) shows that the pole with the ribbon dampers was locked in to Mode 3 at a frequency of 3.8 Hz.

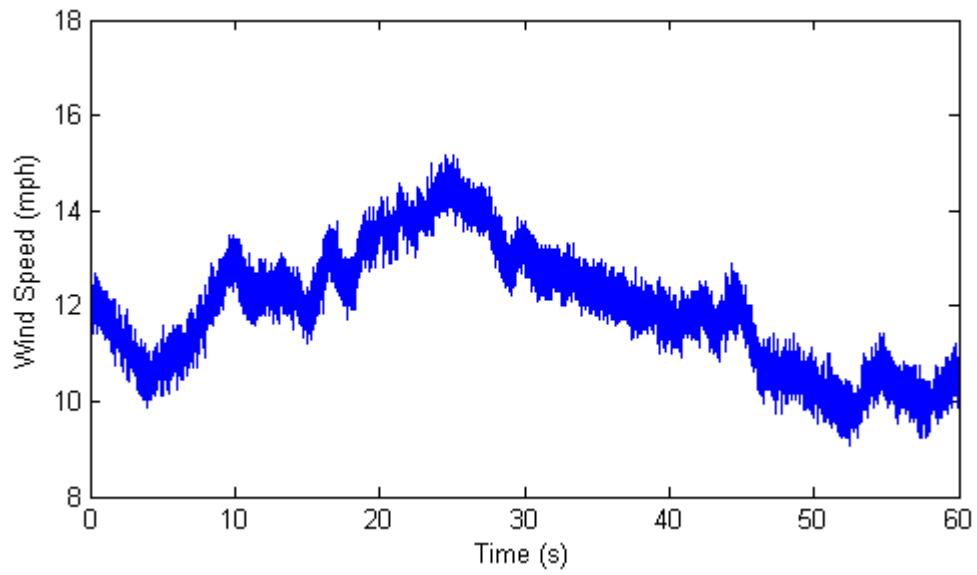


Figure 63. Wind speed vs. time

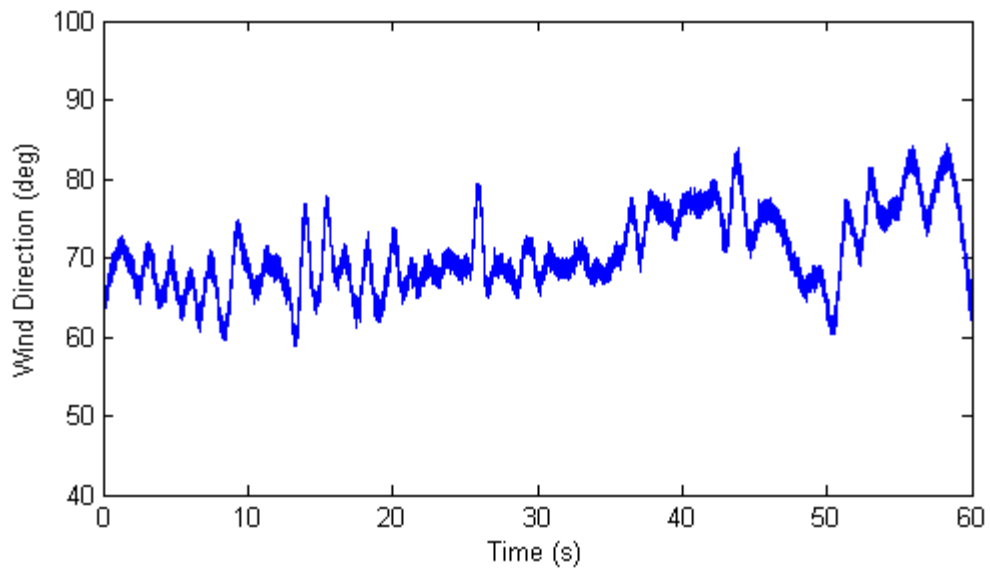


Figure 64. Wind direction vs. time

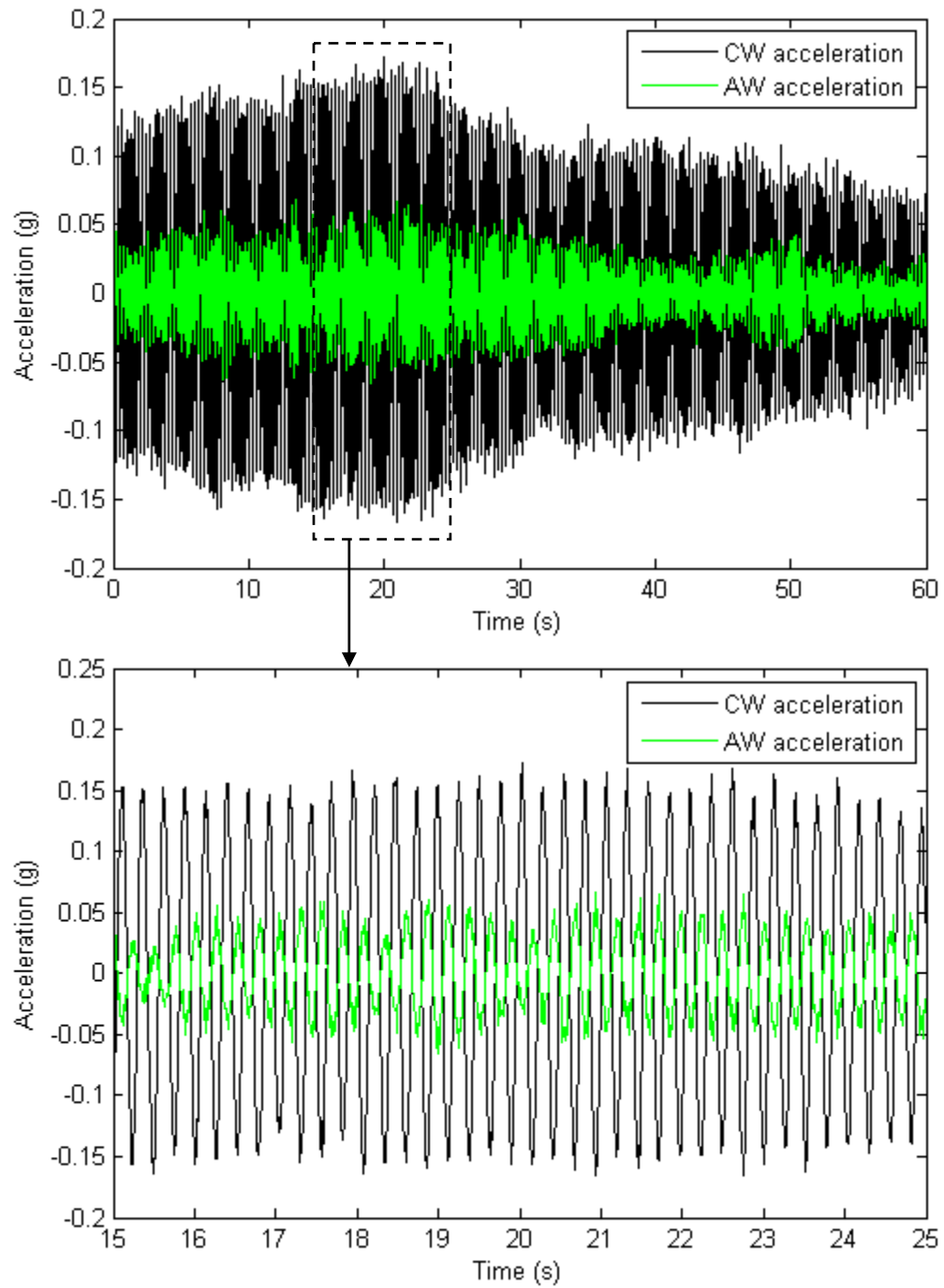


Figure 65. Acceleration vs. time at a mean wind speed of 11.9 mph (Node 467)

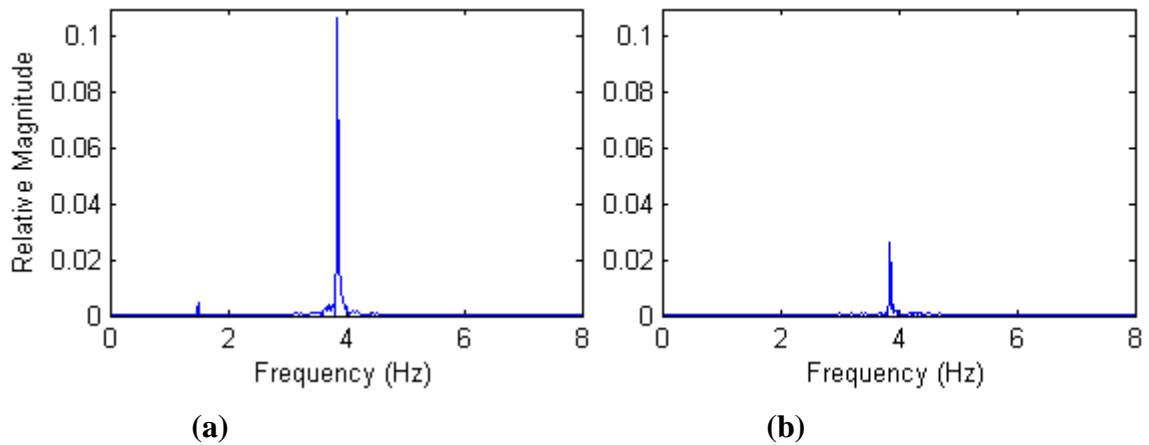


Figure 66. FFT of (a) crosswind and (b) alongwind accelerations at a mean wind speed of 11.9 mph

5.3.2 Helical Strakes

Twelve sets of data were logged with the pole retrofitted with helical strakes at mean wind speeds varying from 10.3 to 19.8 mph. Six of the twelve data sets were determined to contain one or more instances of Mode 3 lock-in.

Figure 67 compares the crosswind response of the unretrofitted pole with that of the pole retrofitted with helical strakes. Note from the plot that, although the retrofitted pole experienced fewer instances of amplified accelerations, it experienced higher crosswind accelerations than the unretrofitted pole. The maximum acceleration recorded with the helical strakes was 0.36g, while accelerations for the unretrofitted pole peaked at 0.26g (28% less than the pole with helical strakes). Since accelerations were not recorded continuously, this does not indicate that the strakes necessarily caused the pole's oscillations to increase, however, it is clear that the helical strakes did not eliminate vortex shedding.

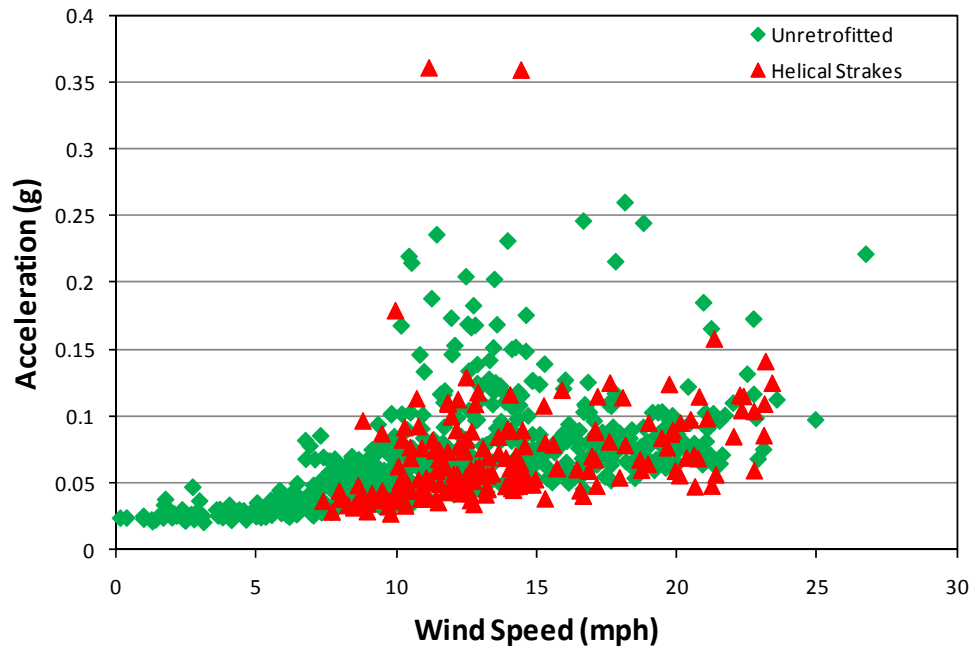


Figure 67. Maximum crosswind acceleration vs. 30s mean wind speed

Figure 68 plots the same crosswind data as Figure 67 but divides the wind speed into 2-mph bins and shows the average of the 30s maximum accelerations with error bars. The 10 to 12 and 14 to 16-mph bins have significantly larger standard deviations due to the two outliers seen in Figure 67; however, the averages are similar to those recorded with the unretrofitted pole. More data would need to be collected to determine if the helical strakes reduce the incidence of lock-in or amplified accelerations.

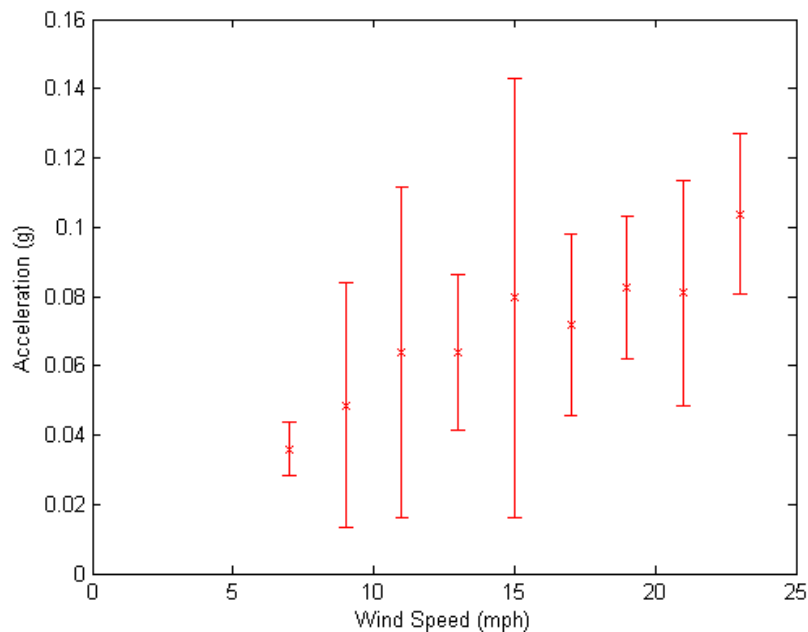


Figure 68. Average maximum CW acceleration vs. 30s mean wind speed (helical strakes)

The deflection corresponding to the maximum acceleration is 0.24 in at the height of the accelerometer (56 ft). The mode shapes for the pole were used to determine that the maximum deflection for the pole (at the upper antinode for Mode 3) is 0.41 in.

A maximum stress range of 2.4 ksi was observed at a mean wind speed of 12.8 mph.

A one-minute record of wind and acceleration data containing the largest acceleration observed for the pole retrofitted with helical strakes is provided in Figure 69 - Figure 71 below. The mean wind speed is 12.8 mph.

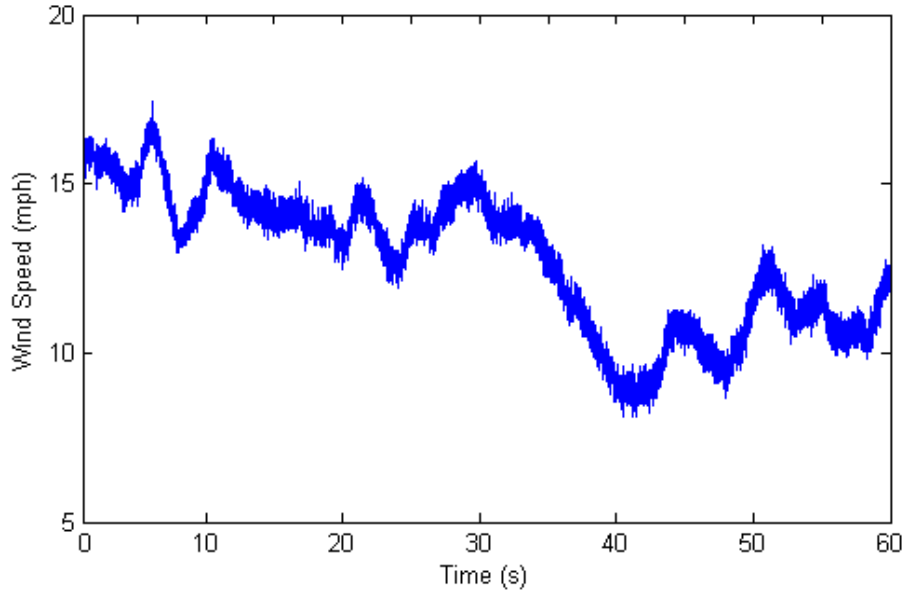


Figure 69. Wind speed vs. time

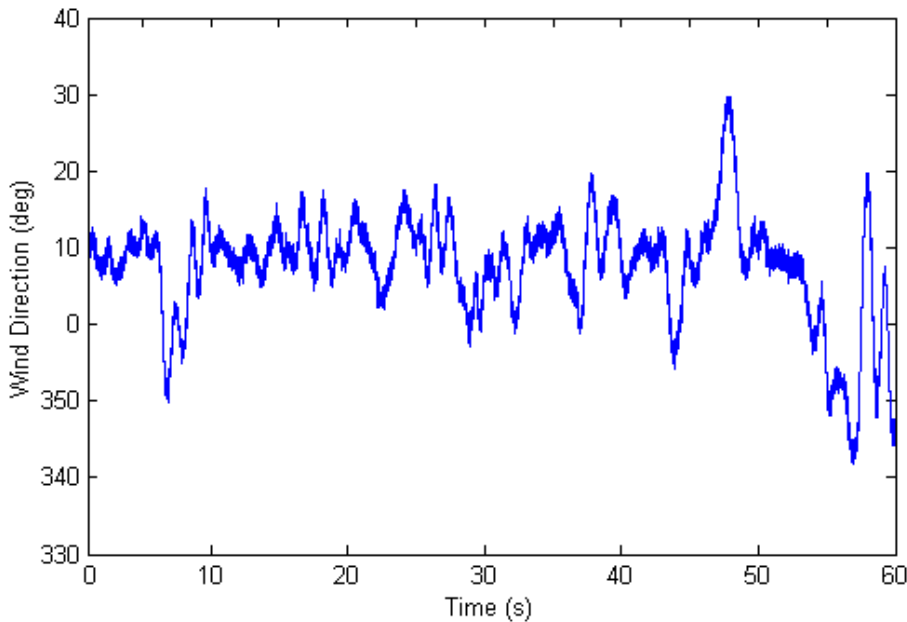


Figure 70. Wind direction vs. time

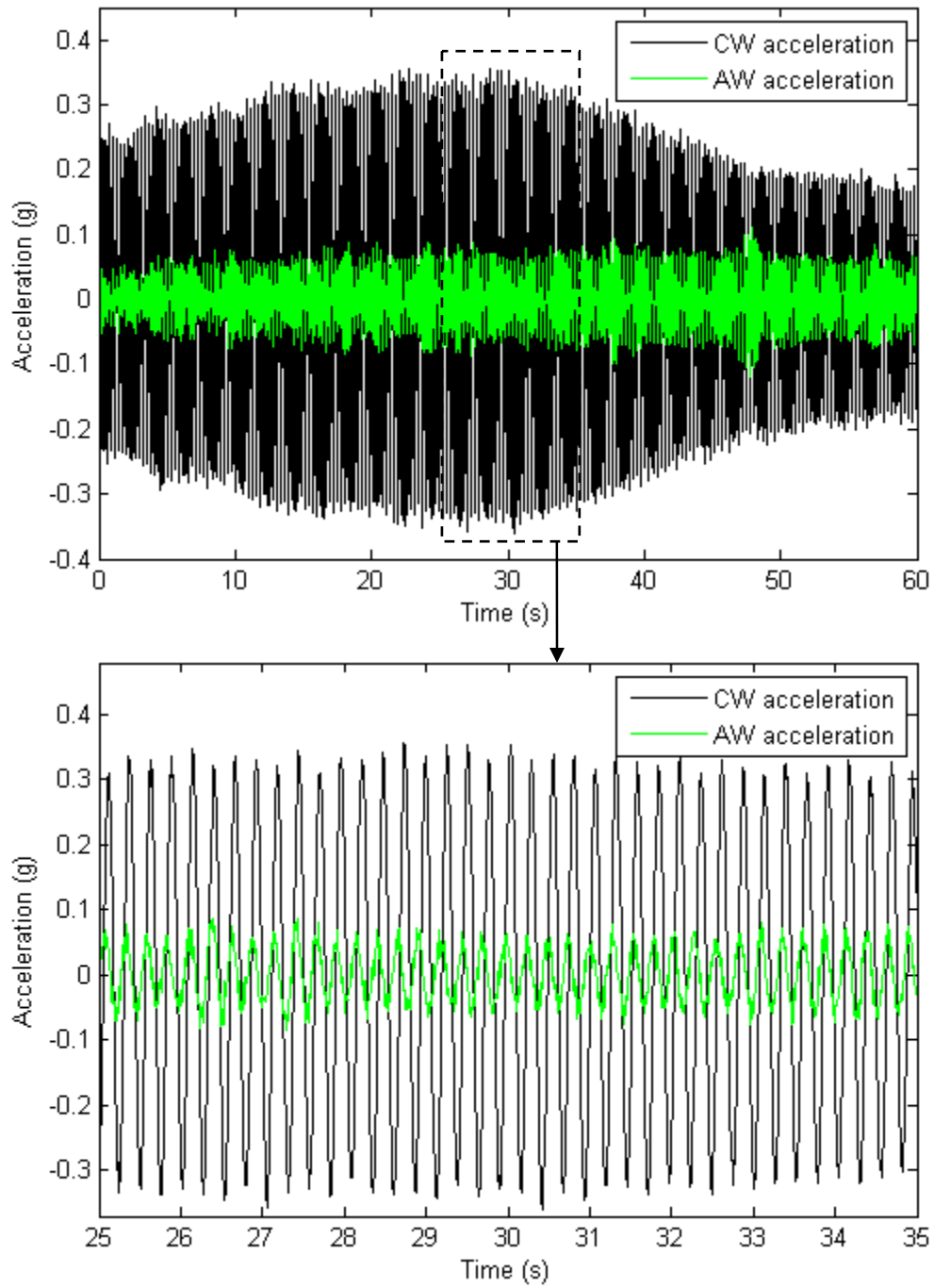


Figure 71. Acceleration vs. time at a mean wind speed of 12.8 mph (Node 464)

FFT analysis of the wind data (Figure 72) shows that the pole retrofitted with helical strakes was locked in to Mode 3 at 3.8 Hz.

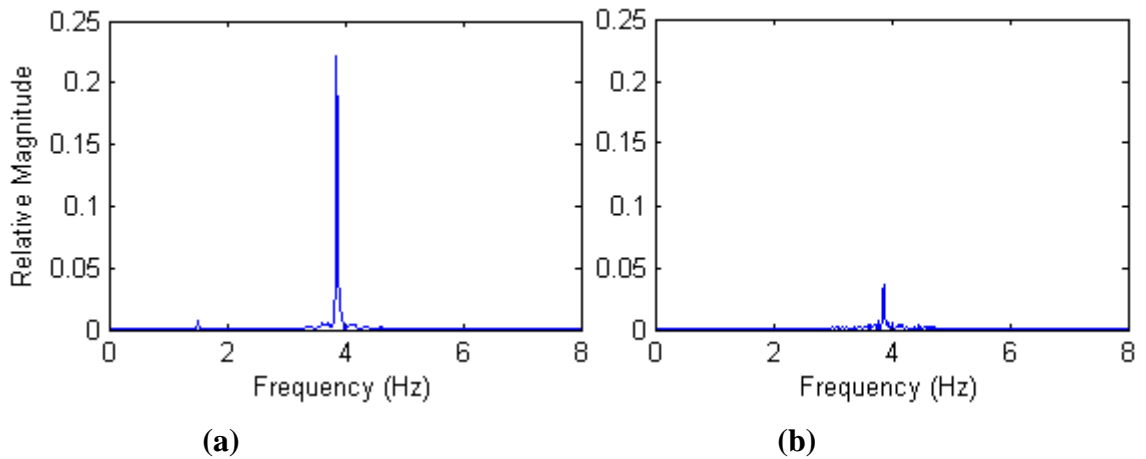


Figure 72. FFT of (a) crosswind and (b) alongwind accelerations at a mean wind speed of 12.8 mph

Figure 73 illustrates a one-minute record of stress data corresponding to the wind acceleration data provided above. The maximum stress range coincides with the maximum acceleration.

Figure 74 shows acceleration vs. stress range using a selection of data collected with the helical strakes. (The data were selected to include the full range of accelerations up to the maximum of 0.36g.) The graph clearly displays a correlation exists between acceleration and stress range.

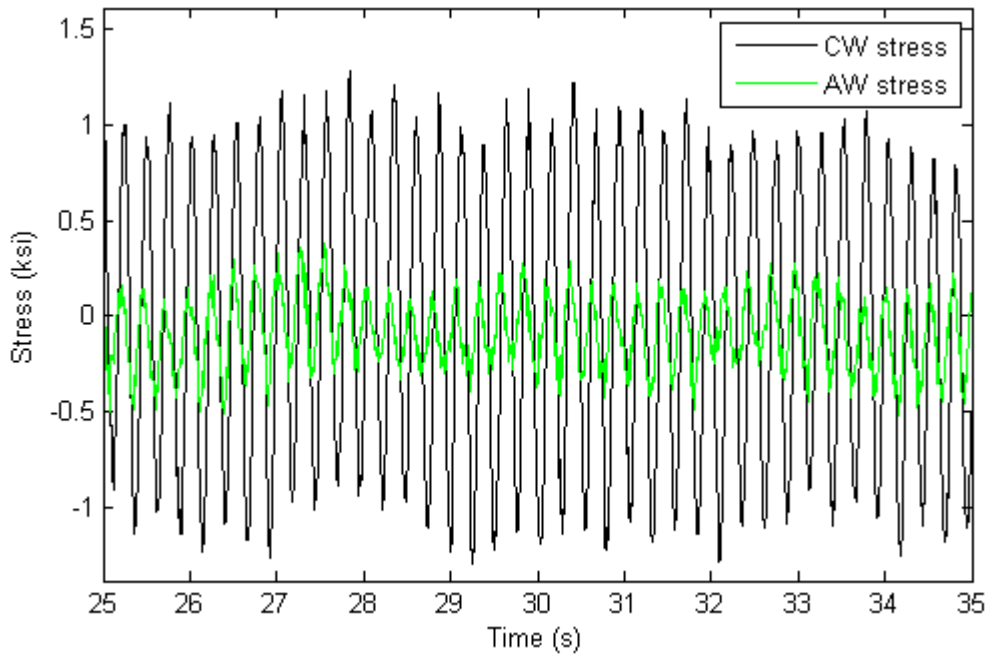


Figure 73. Stress vs. time at a mean wind speed of 12.8 mph

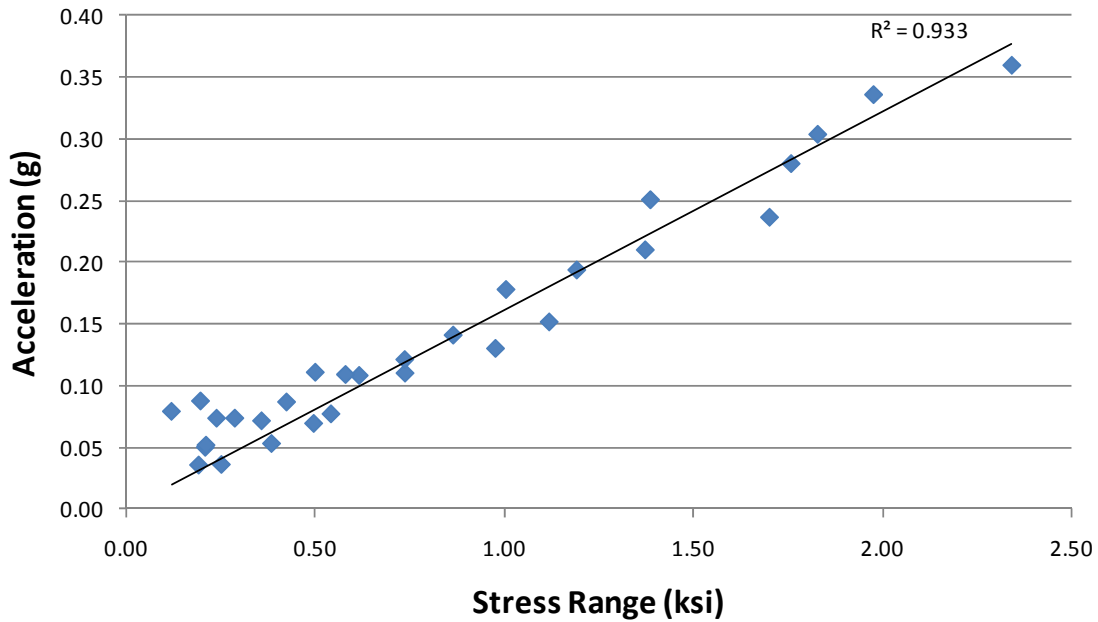


Figure 74. Maximum acceleration vs. stress range

Since there is a correlation between acceleration and stress range, where strain data are not available the stress range (in ksi) at 60 in can be estimated by multiplying the peak acceleration at 56 ft (in g) by a factor of 6.2. Using the modal analysis and the pole’s geometry it can be determined that the stress at the base is approximately 17% higher than that at 60 in when the pole is vibrating in Mode 3. (This is a conservative estimate for Modes 1 and 2, where the ratio of the stress at the base to the stress at 60 in is less than that in Mode 3.) Therefore, multiplying the acceleration at 56 ft (in g) by a factor of 7.3 will yield an approximation for the stress range at the base.

5.3.3 Perforated Shroud

Fourteen sets of data were logged with the perforated shroud retrofit at mean wind speeds varying from 6.7 to 18 mph. These data sets were not found to contain a single instance of lock-in at any mode. Typically, the first three to five modal frequencies were present in the data, depending on the mean wind speed.

Figure 75 compares the crosswind response of the unretrofitted pole with that of the pole retrofitted with the perforated shroud. The retrofitted pole’s accelerations never became amplified over the range of wind speeds that excite Mode 3 in the unretrofitted pole.

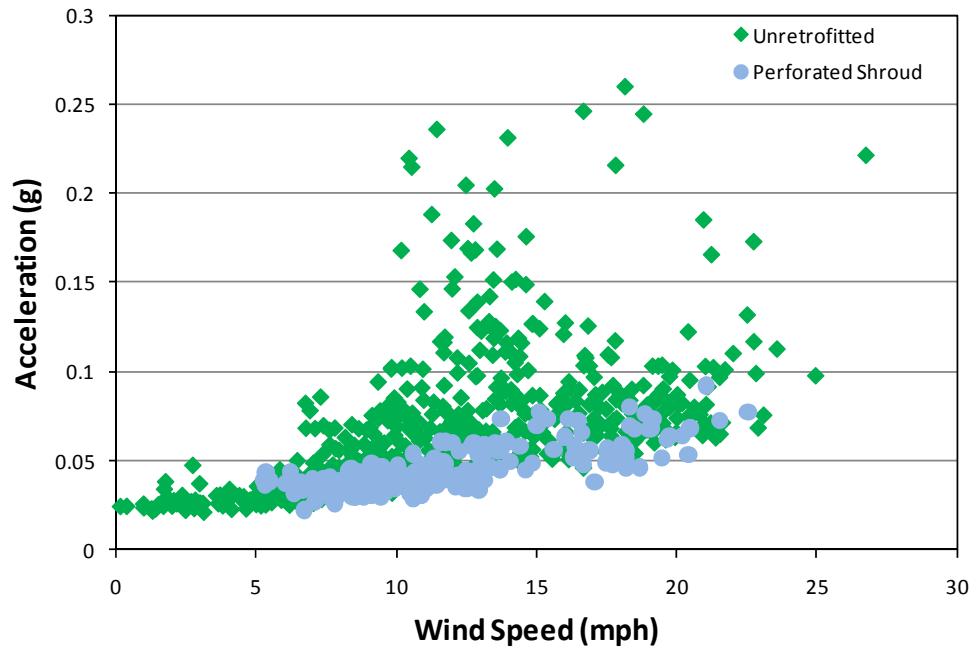


Figure 75. Maximum crosswind acceleration vs. 30s mean wind speed

A one minute record of wind and acceleration data for the pole retrofitted with the perforated shroud (Figure 76 - Figure 78) is compared to the data set containing the largest oscillations for the unretrofitted pole (Figure 59 - Figure 61).

Figure 79 compares the wind speed records for the two scenarios. Both have a mean wind speed of 18.7 mph, and it can be seen from the histogram that the distributions of wind velocities are similar. The wind speed data for the unretrofitted pole have a standard deviation of $\sigma = 2.2$, while $\sigma = 2.0$ for the wind speed data with the perforated shroud. The wind direction record for the retrofitted pole is more constant than that of the unretrofitted pole, as can be seen in Figure 80. Therefore, the wind conditions with the perforated shroud were more ideal for the occurrence of vortex shedding vibrations.

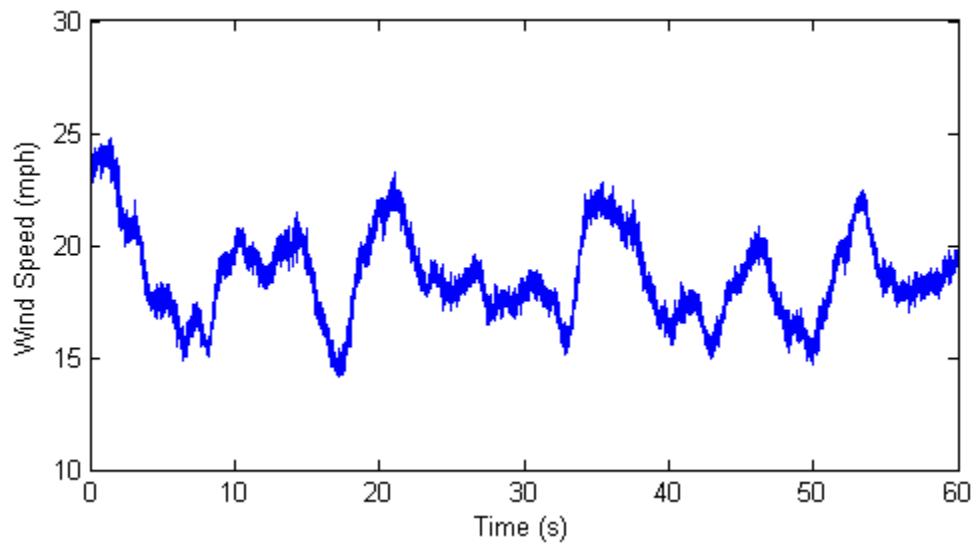


Figure 76. Wind speed vs. time

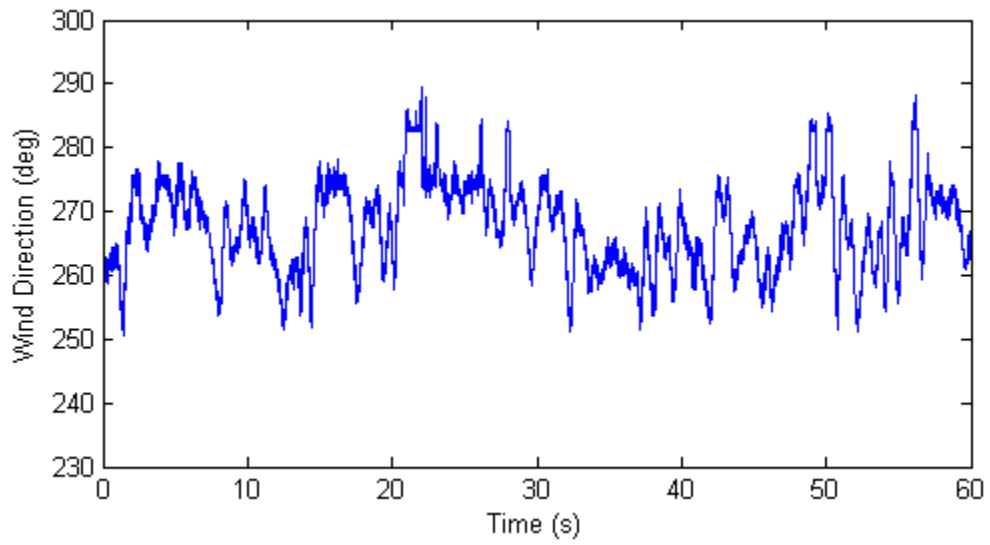


Figure 77. Wind direction vs. time

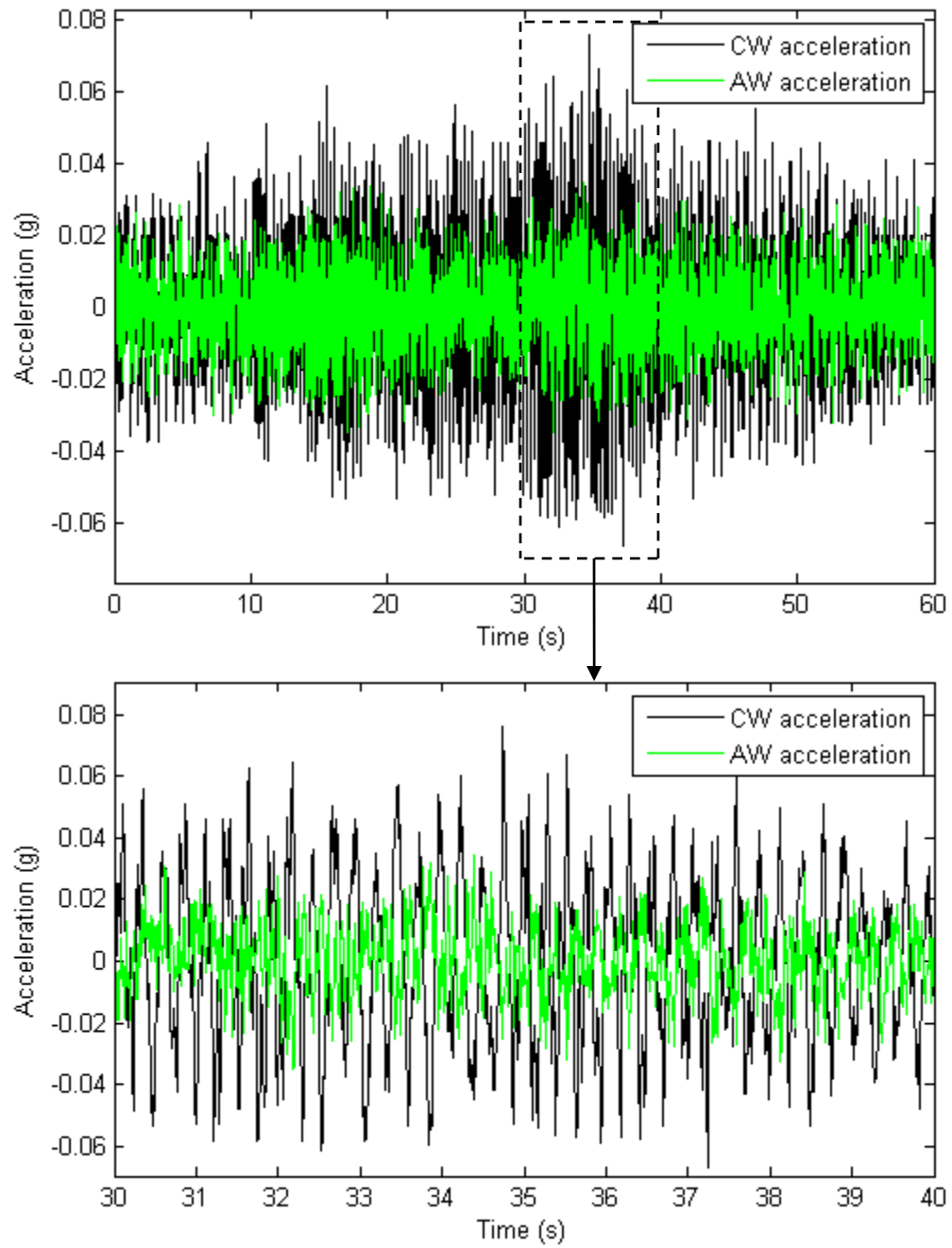


Figure 78. Acceleration vs. time at a mean wind speed of 18.7 mph (Node 464)

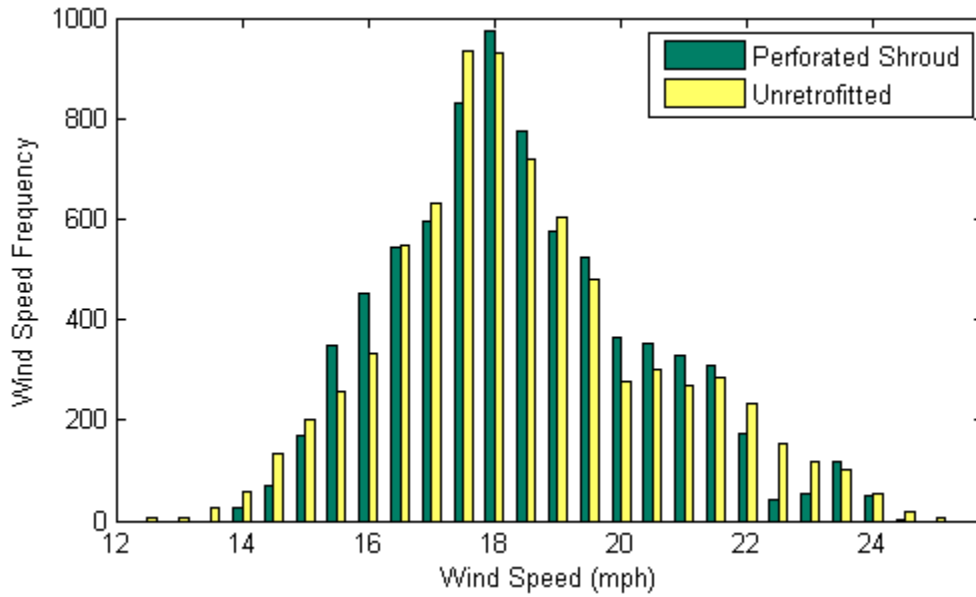


Figure 79. Comparison of wind speed records for unretrofitted pole and perforated shroud

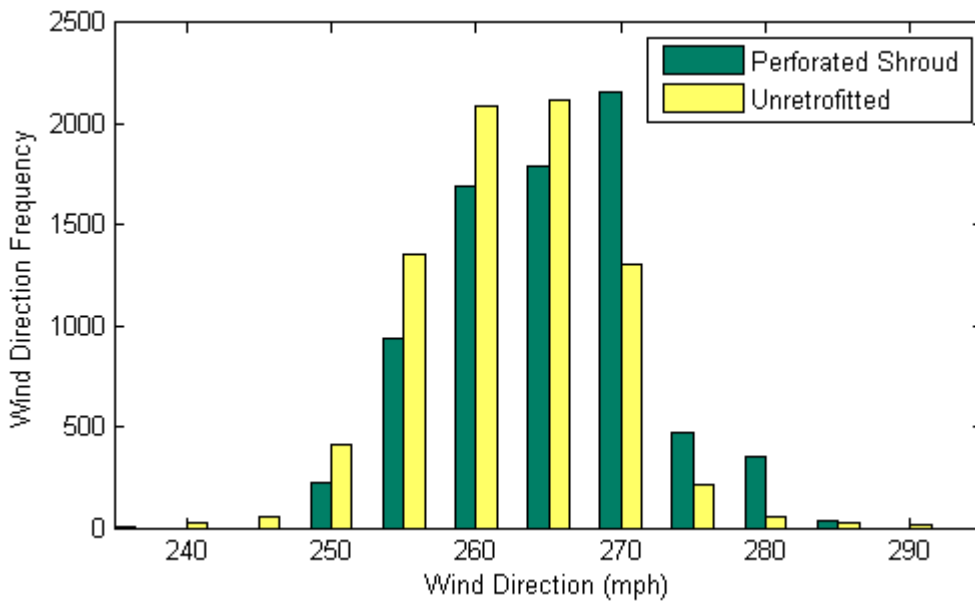


Figure 80. Comparison of wind direction records for unretrofitted pole and perforated shroud

The maximum acceleration observed for the pole retrofitted with the perforated shroud was 0.076g, while the acceleration for the unretrofitted pole peaked at 0.26g. Therefore, when the unretrofitted and retrofitted poles were experiencing similar loading, the accelerations in the unretrofitted pole were 3.4 times higher than those of the pole retrofitted with the perforated shroud.

The maximum stress range observed for the pole retrofitted with the perforated shroud was 0.33 ksi.

FFT analysis of the two data sets also shows that while the unretrofitted pole was locked in to Mode 3 (Figure 62), the pole with the perforated shroud was vibrating at frequencies characteristic of Modes 1 – 5 (Figure 81).

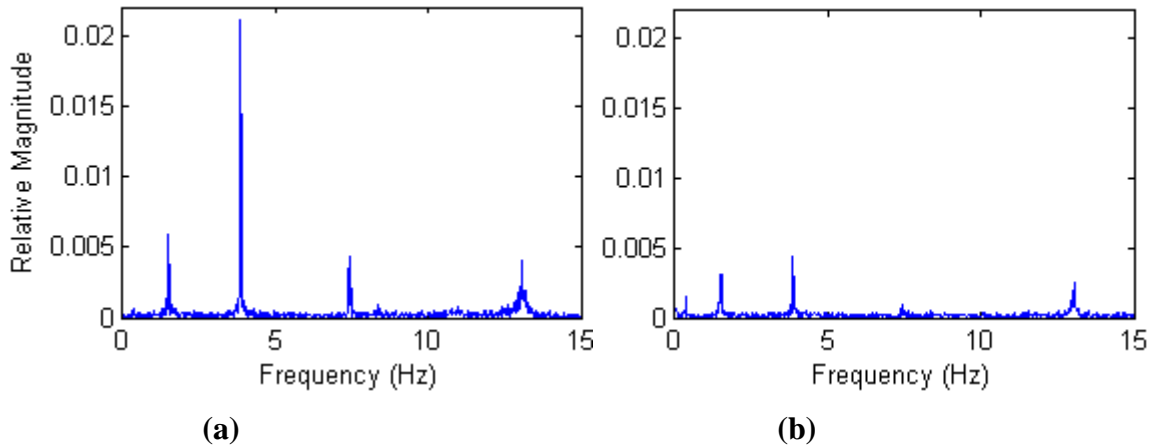


Figure 81. FFT of (a) crosswind and (b) alongwind accelerations at a mean wind speed of 18.7 mph

5.3.4 Surface Roughness

Thirteen sets of data were logged with the pole retrofitted with surface roughness at mean wind speeds varying from 9.9 to 15.4 mph. Four of the 13 data sets were found to contain one or more instances of Mode 3 lock-in.

Figure 82 compares the crosswind response of the unretrofitted pole with that of the pole retrofitted with surface roughness. Note there is very little difference between the pole with the surface roughness and the unretrofitted pole. The maximum acceleration recorded for the pole with surface roughness was 0.22g, while accelerations for the unretrofitted pole peaked at 0.26g (18% higher than the pole with surface roughness).

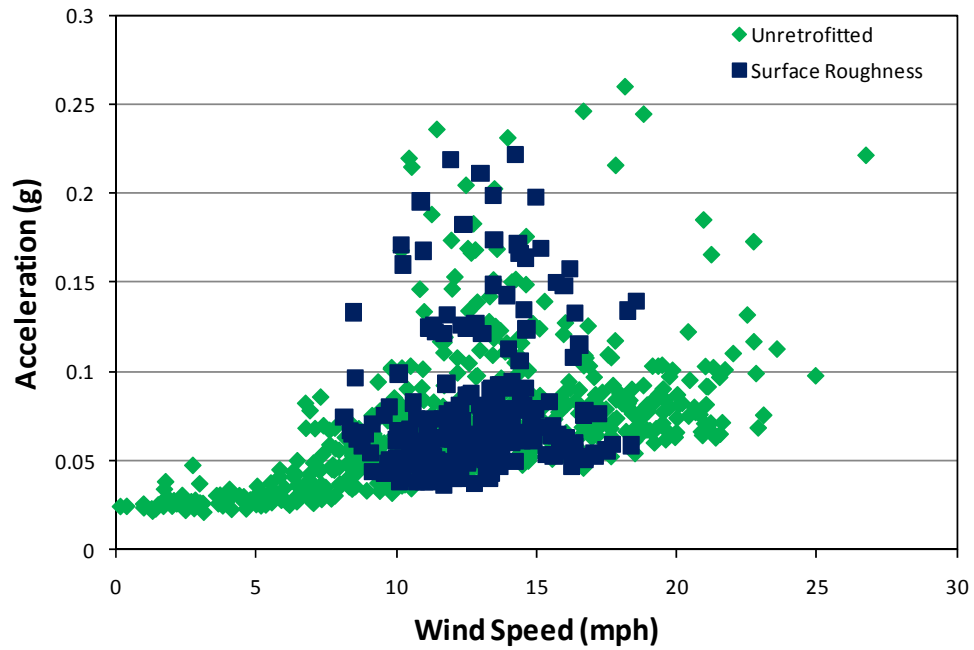


Figure 82. Maximum crosswind acceleration vs. 30s mean wind speed

It is clear from Figure 82 that this particular application of surface roughness did not eliminate or even reduce vortex shedding loads under the given conditions.

The deflection corresponding to the maximum acceleration is 0.15 in at the height of the accelerometer (56 ft). The mode shapes were used to determine that the maximum deflection for the pole (at the upper antinode for Mode 3) is 0.25 in.

The maximum stress range observed for the pole with surface roughness was 1.1 ksi.

A one minute record of wind and acceleration data containing the largest acceleration observed for the pole retrofitted with surface roughness is provided in Figure 83 - Figure 85 below. The mean wind speed is 12.2 mph.

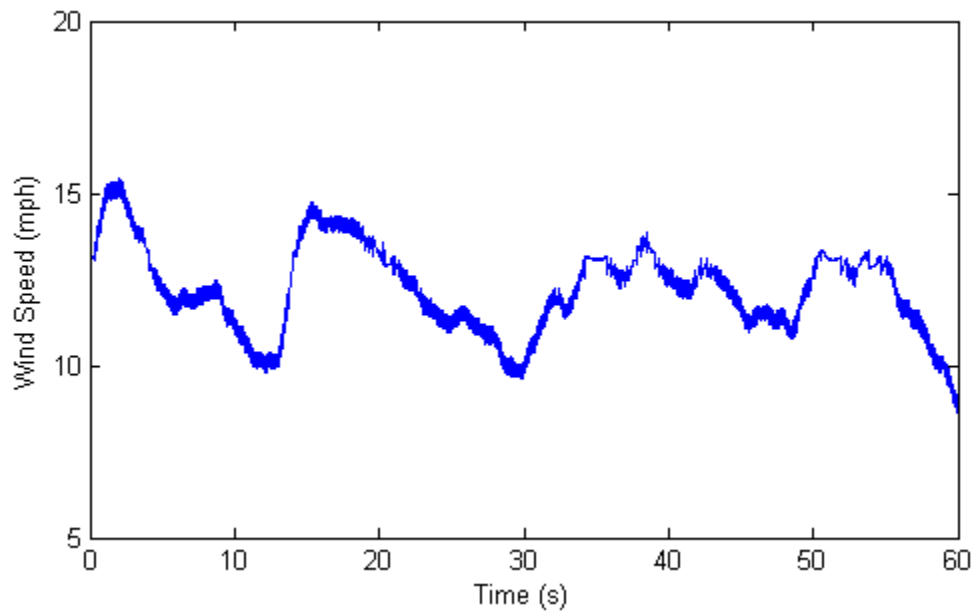


Figure 83. Wind speed vs. time

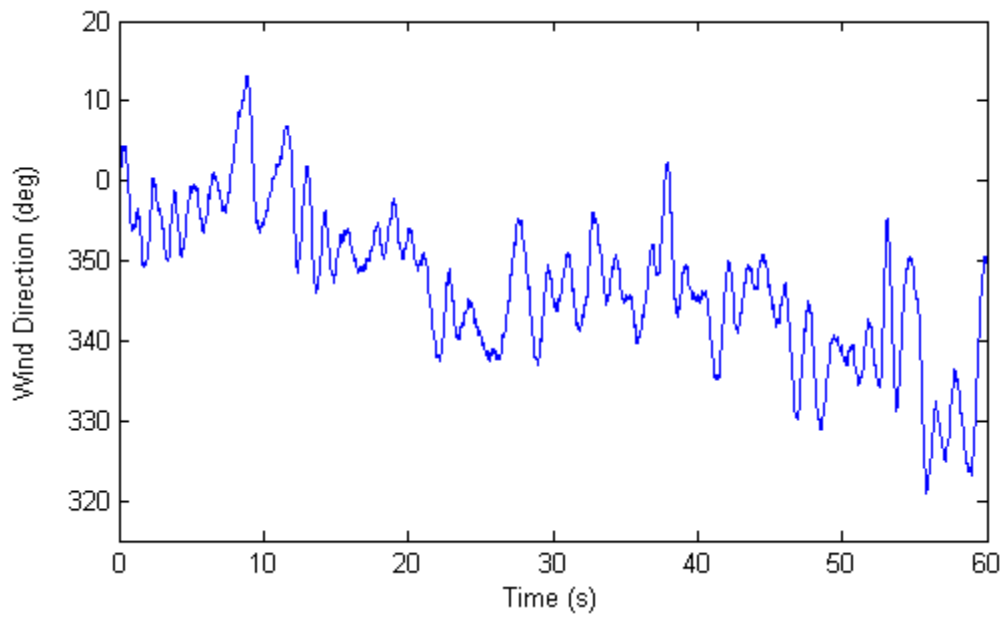


Figure 84. Wind direction vs. time

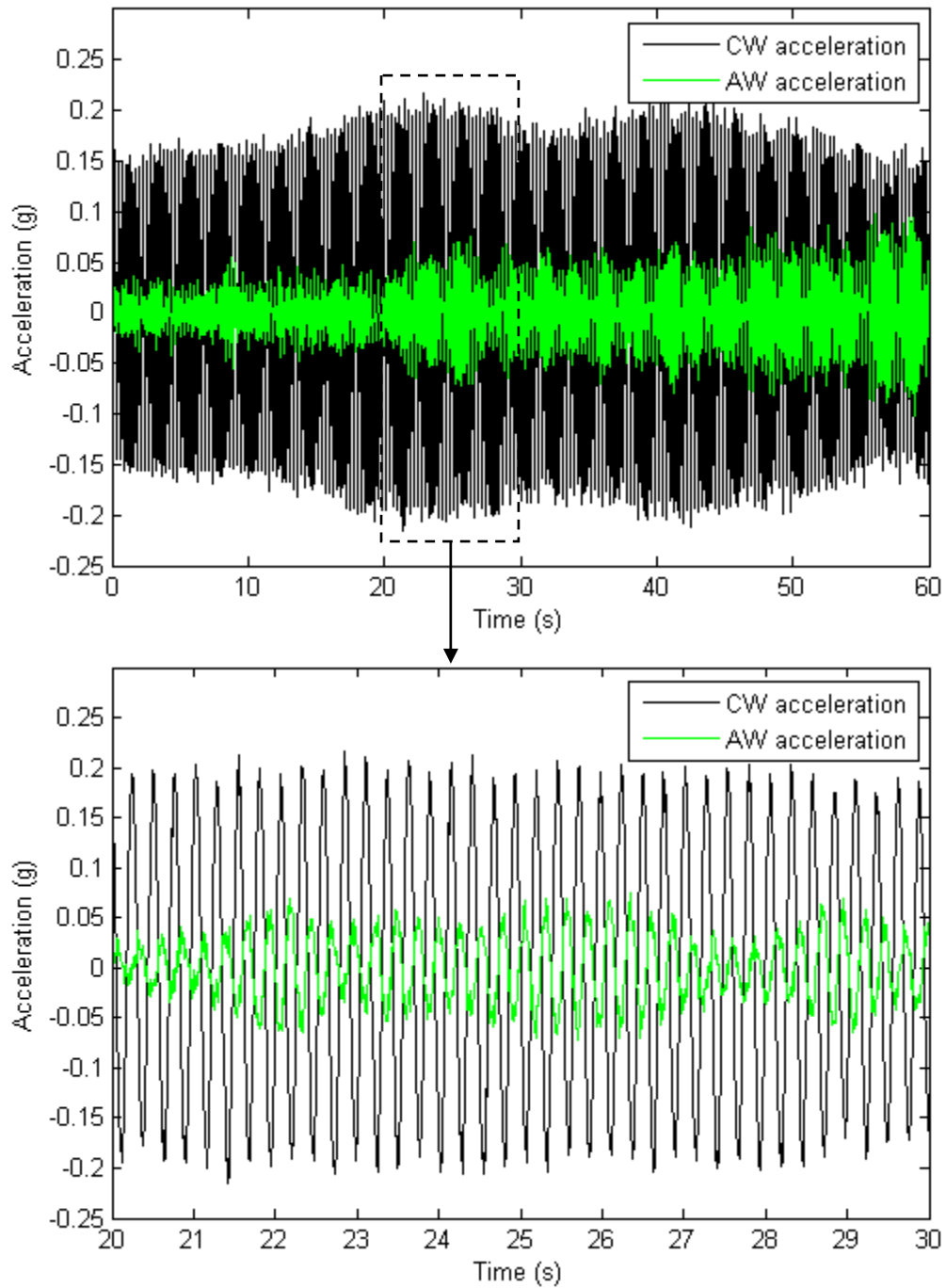


Figure 85. Acceleration vs. time at a mean wind speed of 12.2 mph (Node 464)

FFT analysis of the wind data (Figure 86) shows that the pole was locked in to Mode 3 at a frequency of 3.8 Hz.

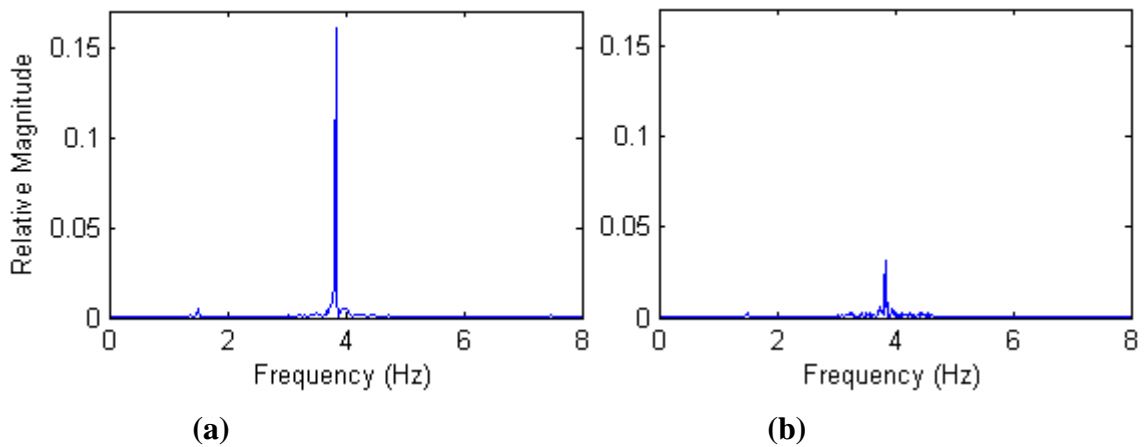


Figure 86. FFT of (a) CW and (b) AW accelerations at a mean wind speed of 12.2 mph

5.4 Summary

Acceleration and strain data were collected from the unretrofitted pole and with four different aerodynamic dampers. Technical problems with the voltage node that collected strain data caused much of it to be unusable. A correlation between acceleration and stress range was determined, which allows one to predict the stress range where strain data are not available. Maximum deflections were also calculated using the maximum accelerations, the modal frequency, and the mode shapes.

Table 14 summarizes the findings. The high-mast pole was frequently observed to achieve Mode 3 lock-in when retrofitted and with each of the aerodynamic dampers, with the exception of the perforated shroud. The pole retrofitted with the perforated shroud never locked in at any mode. Maximum accelerations (and consequently deflections and stress ranges) were observed to occur when the pole was vibrating in Mode 3 for the unretrofitted pole, ribbons, helical strakes, and surface roughness. The maximum deflections for the pole are d_{97ft} . Maximum deflection with the perforated shroud was not calculated because it was never vibrating in a single mode. The maximum stress ranges (at 60 in) are $\Delta\sigma_{max}$. Data were not collected continuously, so the maxima are the highest oscillations recorded and not necessarily the highest the pole underwent during the testing period.

Table 14 Maximum accelerations and deflections

| | $a_{CW,max}$ (g) | U_{30s} (mph) | Mode | f (Hz) | d_{97ft} (in) | $\Delta\sigma_{max}$ (ksi) |
|--------------------------|------------------|-----------------|------|--------|-----------------|----------------------------|
| Unretrofitted | 0.26 | 18.1 | 3 | 3.8 | 0.29 | 1.6 |
| Ribbons | 0.17 | 12.1 | 3 | 3.8 | 0.17 | 0.93 |
| Helical Strakes | 0.36 | 11.2 | 3 | 3.8 | 0.41 | 2.4* |
| Perforated Shroud | 0.09 | 21.1 | -- | -- | -- | 0.33* |
| Surface Roughness | 0.22 | 14.2 | 3 | 3.8 | 0.25 | 1.1* |

Note: * indicates measured stress range. Other stress ranges were estimated based on accelerations.

The correlation between acceleration and stress range can also be used to determine that the acceleration at 56 ft would be approximately 0.6g when the CAFL of 4.5 ksi is reached at the base. Assuming the pole was locked in to Mode 3, this would correspond to a maximum deflection of just 0.7 in at 97 ft.

6 TRAFFIC VIBRATIONS

This research initially assumed that two identical high-mast structures located less than 600 ft apart in open terrain would be exposed to approximately the same wind speeds and directions, and consequently would have similar dynamic responses. Preliminary acceleration data negated this assumption. While Pole 3 achieved Mode 3 (the critical mode) lock-in on twenty occasions (out of thirty-three sets of data recorded), Pole 4 was never observed to lock-in for more than a few seconds at a time. Pole 3 was observed to visibly oscillate when in Mode 3 lock-in, but visible oscillations were never observed on Pole 4.

Figure 87 shows two sets of acceleration data recorded simultaneously on Poles 3 and 4 at a mean wind speed of 15 mph. Pole 3 acceleration peaks at 0.26g, while the maximum acceleration for Pole 4 is only 0.05g. In addition, FFT analysis of these data (Figure 88) showed Pole 3 to be vibrating at 3.8 Hz (Mode 3) while Pole 4 was vibrating at frequencies corresponding to several different modes. Note that the scale of the FFT plot for Pole 4 is ten times as great as that for Pole 3.

The maximum acceleration recorded during testing of Pole 4 was 0.16g (at 41 ft) and occurred during a brief instance of Mode 3 lock-in (at $V_{mean} = 13.4$ mph). Mode 4 lock-in was also observed on Pole 4. This indicates that the pole is capable of lock-in but some factor is interfering with resonance.

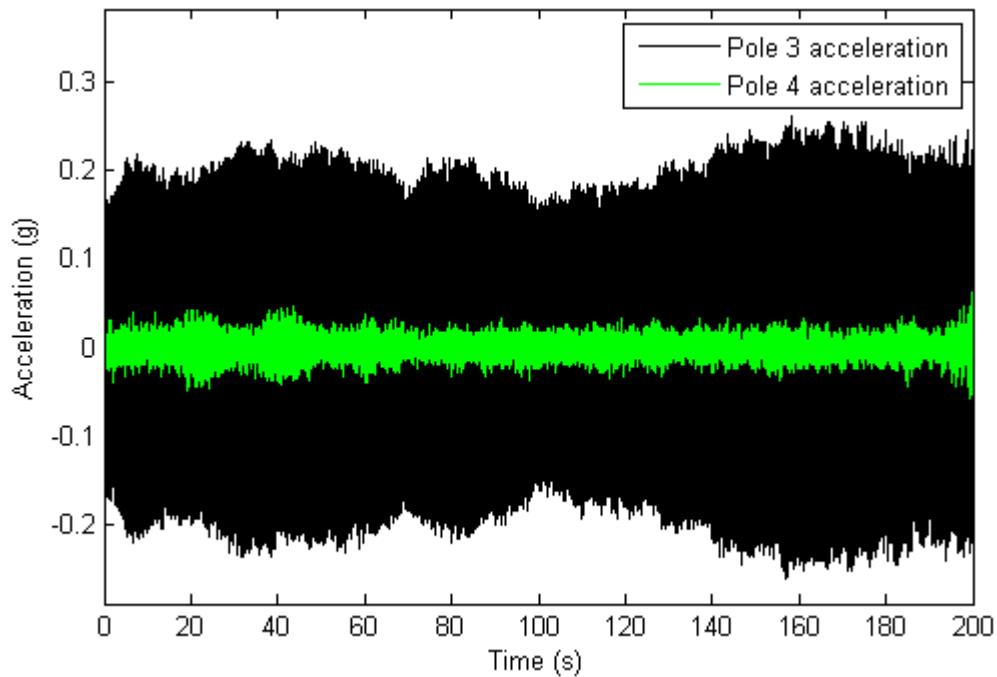


Figure 87. Crosswind acceleration vs. time at 56 ft for Pole 3 and Pole 4

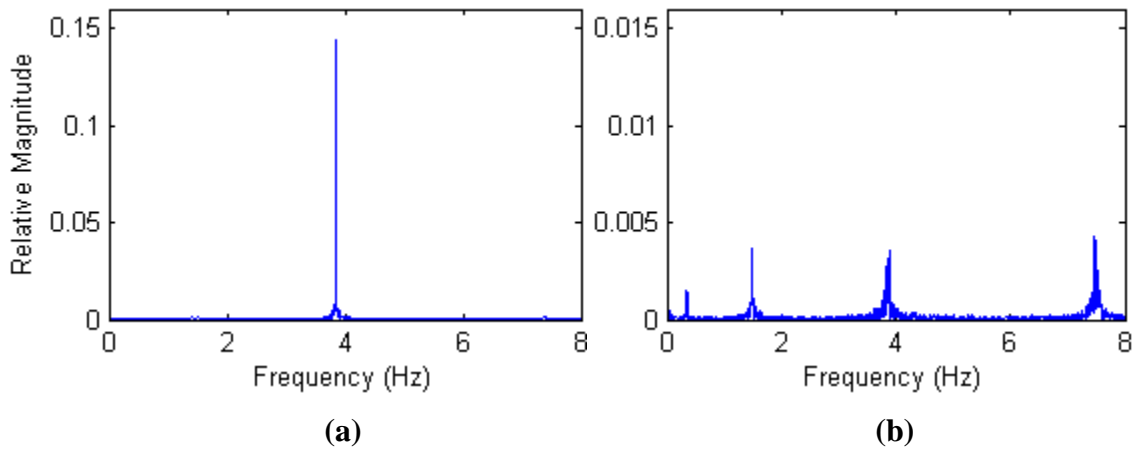


Figure 88. FFT analysis of (a) Pole 3 and (b) Pole 4 crosswind accelerations

Pole 4 vibrations were studied more closely using extremely sensitive BDI accelerometers and particular attention was paid to the pole’s response when large vehicles passed. Data were logged under three wind conditions: calm (mean wind speed of 0.04 mph), Mode 2 critical velocity (mean wind speed of 7.1 mph), and Mode 3 critical velocity (mean wind speed of 12.1 mph).

6.1 Test 20 - Calm Conditions

Data were recorded at Pole 4 under calm wind conditions, meaning the only source of excitation was traffic vibrations. Figure 89 shows the accelerations recorded in the north-south, east-west, and vertical directions. The largest response is in the north-south direction, or approximately perpendicular to the direction of travel on the interstate highway. An anemometer located at 33 ft on the south side of the pole did not register wind speed from the vehicle gusts.

Figure 90, Figure 91, and Figure 92 show the amplitude spectra for each of the sets of data. It is apparent from the FFT analysis of the north-south accelerations that the dominant frequency of the pole excited by the traffic vibrations is 19.5 Hz. The secondary and tertiary frequencies are 12.9 and 7.5 Hz, respectively. The first three modes of vibration (0.35 Hz, 1.5 Hz, and 3.8 Hz) are essentially non-existent in the traffic vibrations. Analysis of the vertical accelerations shows that there are no dominant frequencies, and therefore traffic vibrations traveling through the ground do not excite the pole vertically.

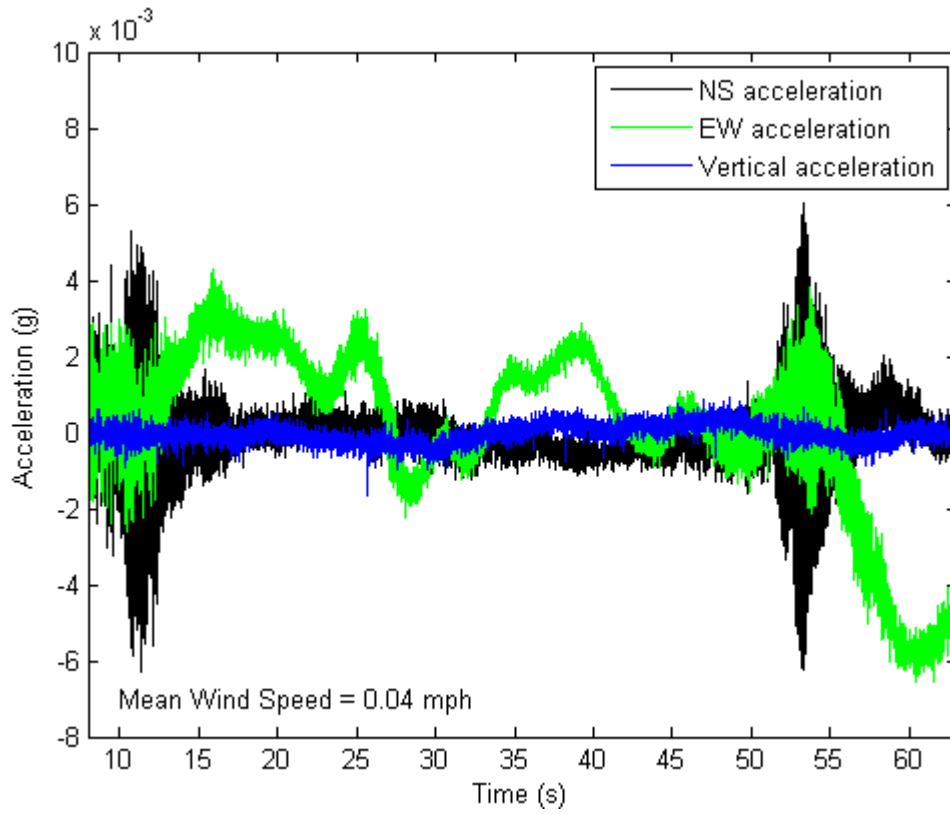


Figure 89. Acceleration vs. time under calm conditions

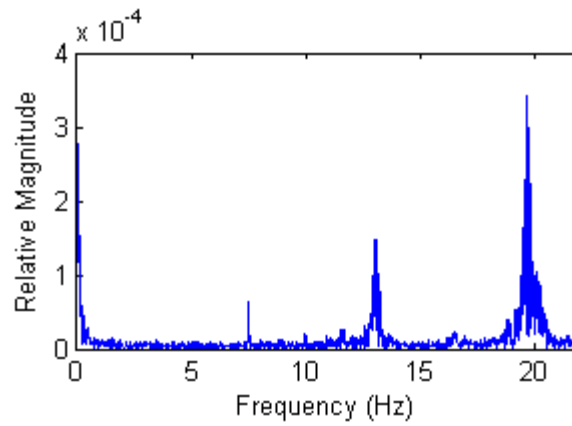


Figure 90. FFT amplitude spectrum for NS accelerations under calm conditions

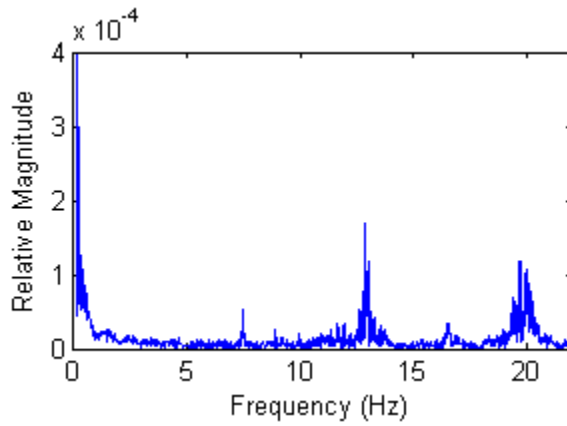


Figure 91. FFT amplitude spectrum for EW accelerations under calm conditions

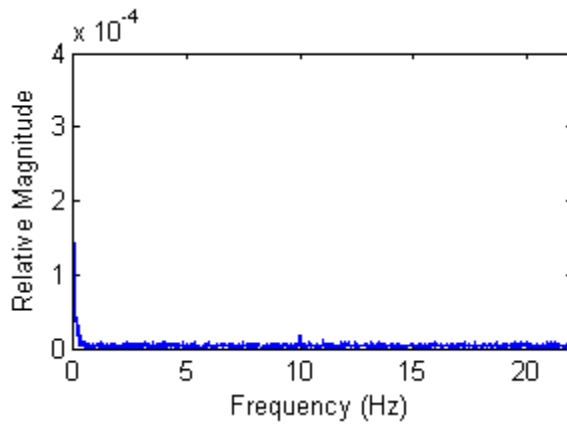


Figure 92. FFT amplitude spectrum for vertical accelerations under calm conditions

Closer inspection of the pole's accelerations under calm wind conditions when there was no heavy vehicle traffic (Figure 93) shows that there is little to no excitation. The peak acceleration during this time period is 0.0008g. There is also little frequency content in the accelerations under calm conditions. There is a small peak in the north-south acceleration data at 12.9 Hz (Figure 94), but this is likely due to vibrations from smaller vehicles passing.

Figure 96 gives a closer look at the traffic excitation. The peak acceleration resulting from traffic vibrations is 0.006g. FFT analysis of the truck gust alone (Figure 97 and Figure 98) again shows 19.5 Hz to be the dominant frequency excited by the traffic vibrations.

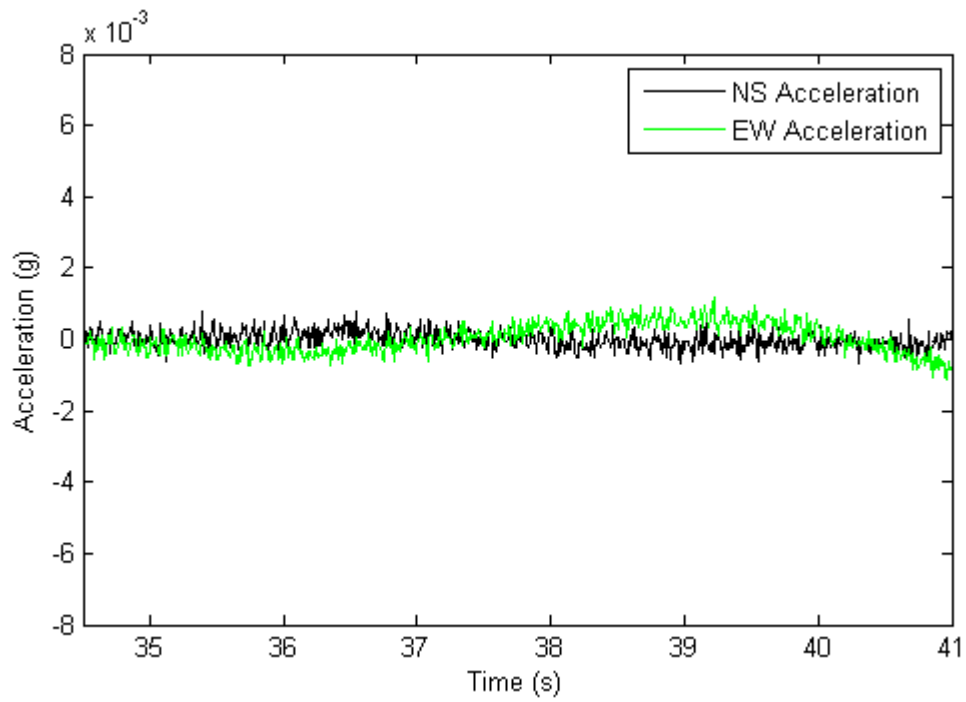


Figure 93. Acceleration vs. time with natural wind (calm conditions)

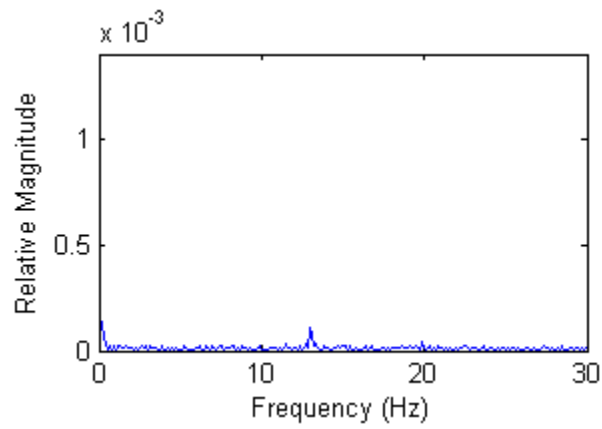


Figure 94. FFT analysis of NS accelerations with natural wind (calm conditions)

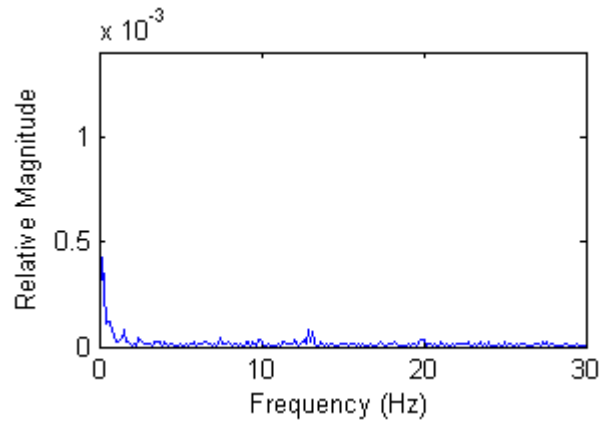


Figure 95. FFT analysis of EW accelerations with natural wind (calm conditions)

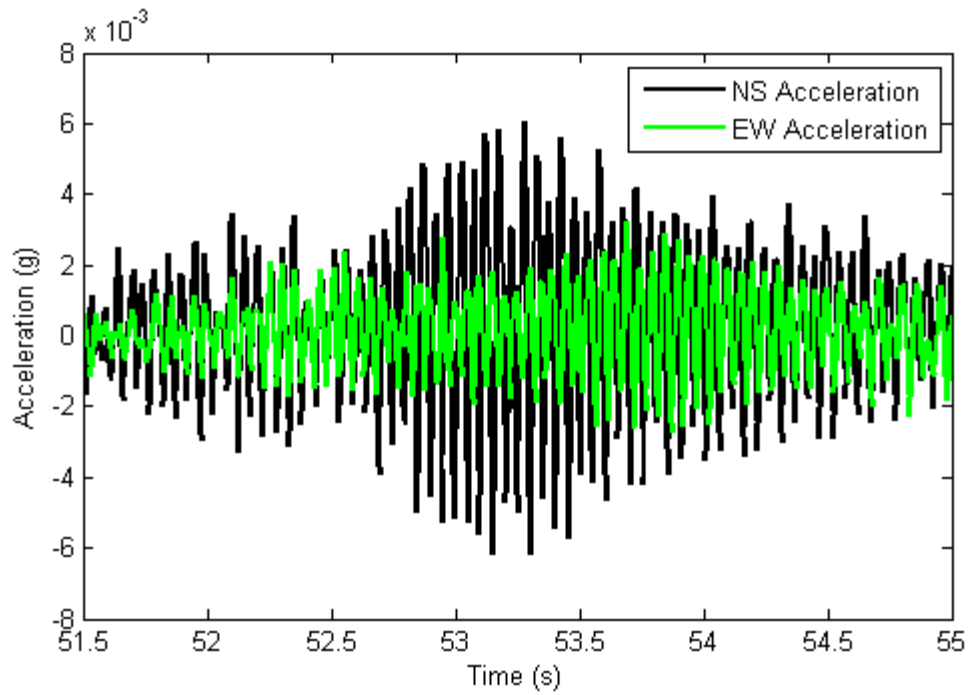


Figure 96. Acceleration vs. time with traffic excitation

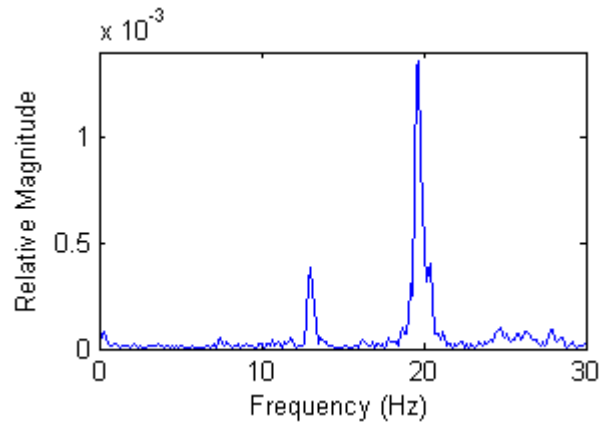


Figure 97. FFT analysis of NS accelerations with traffic excitation

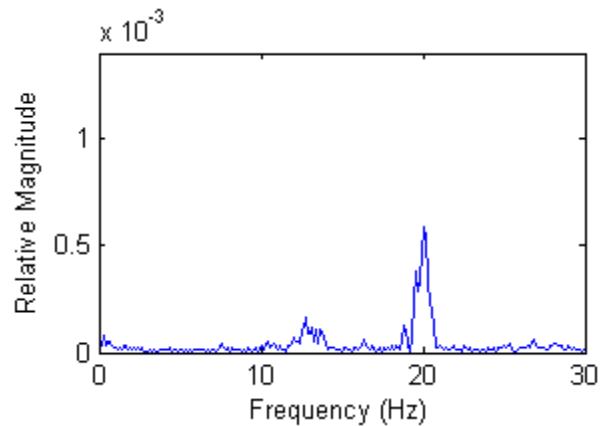


Figure 98. FFT analysis of EW accelerations with traffic excitation

6.2 Test 15 - Mode 2

Data were also collected at a mean wind speed of 7.1 mph (Figure 99). Though the wind was near the critical velocity for Mode 2 and vortex shedding excitation is evident in the data, truck vibrations are apparent as well.

Figure 100 and Figure 101 show that while Mode 2 excitation is dominant (at a frequency of 1.5 Hz), higher modes of vibration are present as well. Vertical accelerations are again negligible (Figure 102).

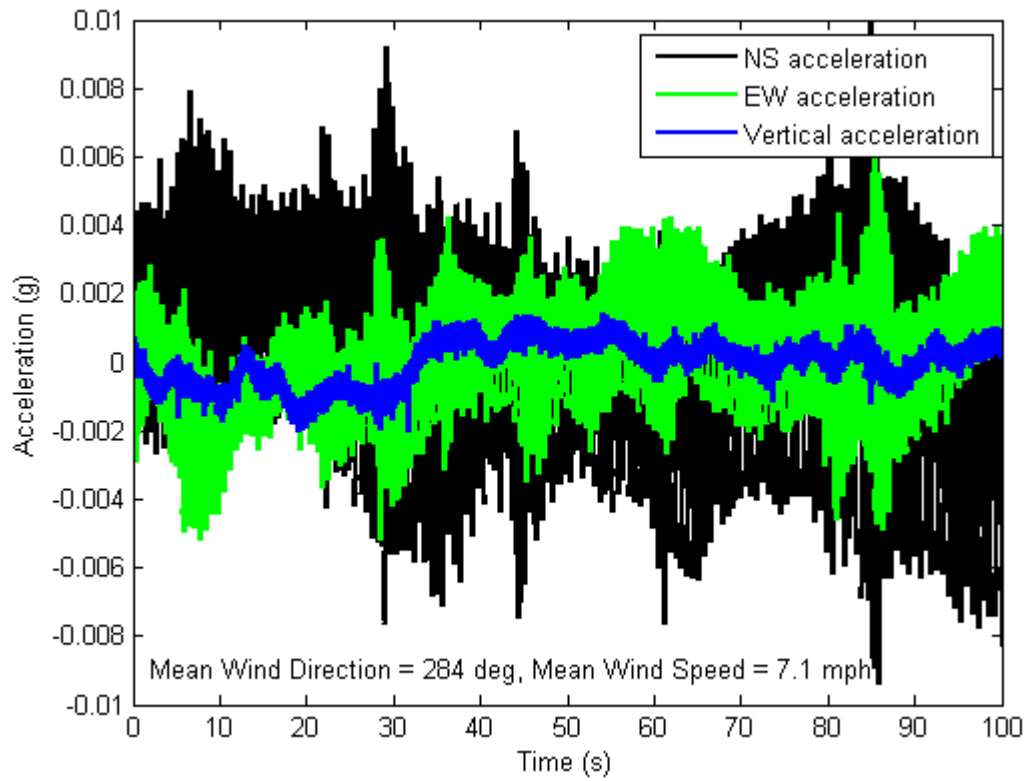


Figure 99. Acceleration vs. time at a mean wind speed of 7.1 mph

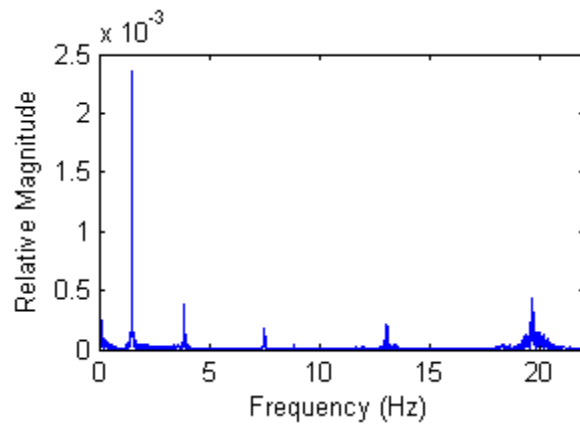


Figure 100. FFT amplitude spectrum for NS accelerations at a mean wind speed of 7.1 mph

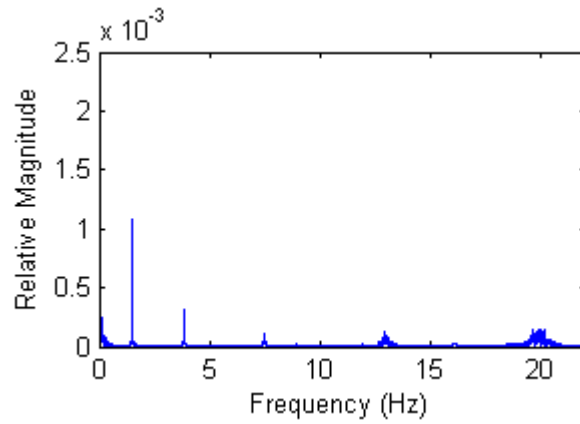


Figure 101. FFT amplitude spectrum for EW accelerations at a mean wind speed of 7.1 mph

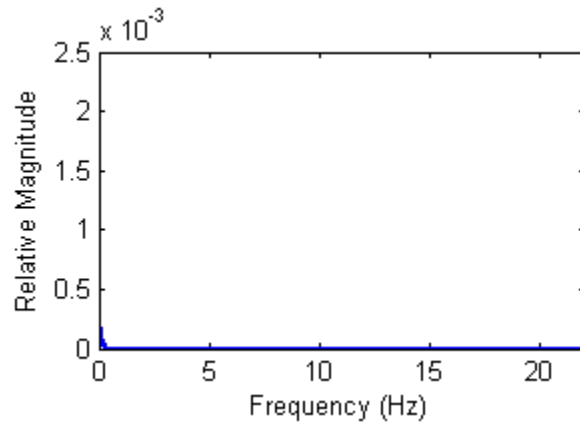


Figure 102. FFT amplitude spectrum for vertical accelerations at a mean wind speed of 7.1 mph

Sinusoidal oscillations (Figure 103) at a frequency of 1.5 Hz were seen when the wind dropped to approximately 6.2 mph (the critical velocity for Mode 2) indicating the presence of vortex shedding. When a tractor trailer truck passed, however, higher frequency vibrations were introduced, and the Mode 2 oscillations were disrupted. A semi passed the pole at approximately 44s (as indicated in Figure 103). It is apparent that the vibrations from the passing vehicle and the turbulence that followed it disrupted the periodic oscillations in the pole, as the wind speed remained essentially constant. The truck passing at an estimated speed of 75 mph disrupted the vortex-induced vibrations for approximately 4s.

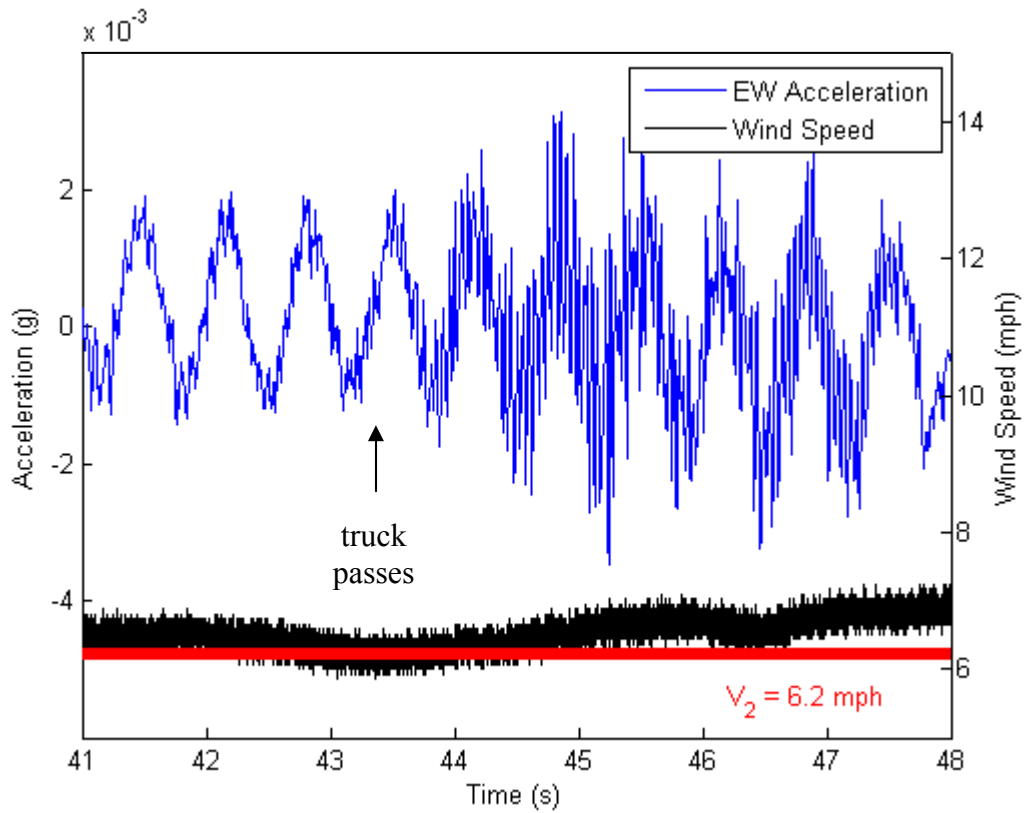


Figure 103. Acceleration vs. time at near-constant wind speed close to Mode 2 critical velocity

Figure 104 is an excerpt of the acceleration data collected at a mean wind speed of 7.1 mph (Figure 99). These data were collected when there was a lull in the traffic, and the pole was only subject to wind loading. Further investigation of the pole's behavior under natural wind loading alone shows that the pole is locked in to Mode 2 at 1.5 Hz in both the north-south and east-west directions (Figure 105, Figure 106).

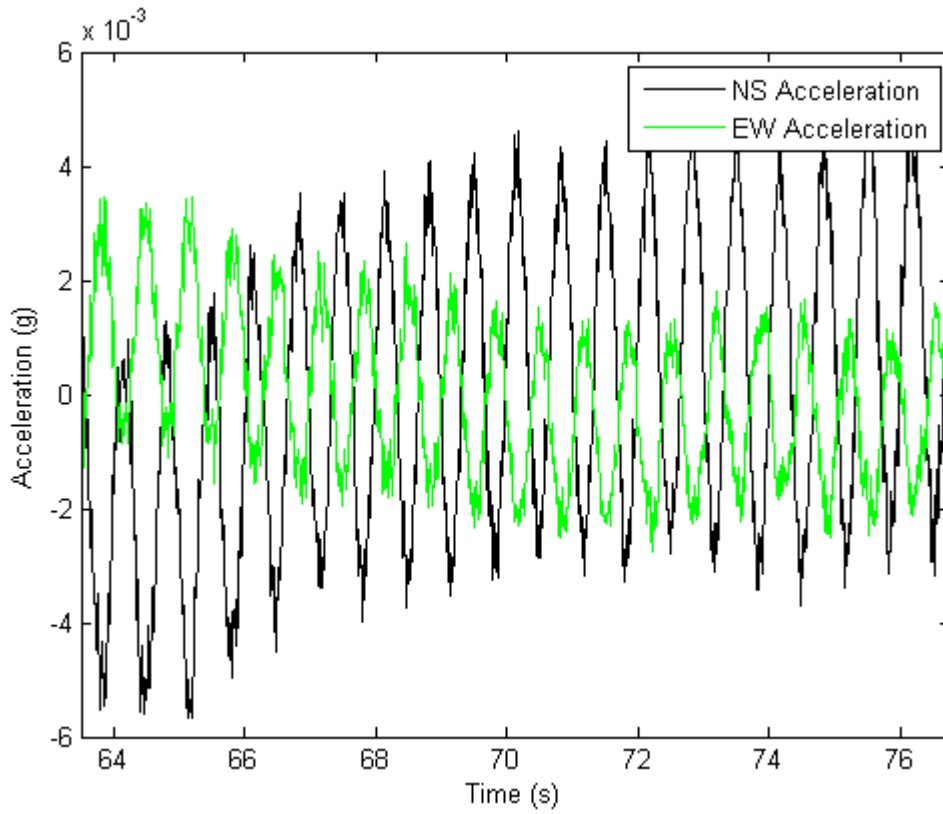


Figure 104. Acceleration vs. time with natural wind (near Mode 2 critical velocity)

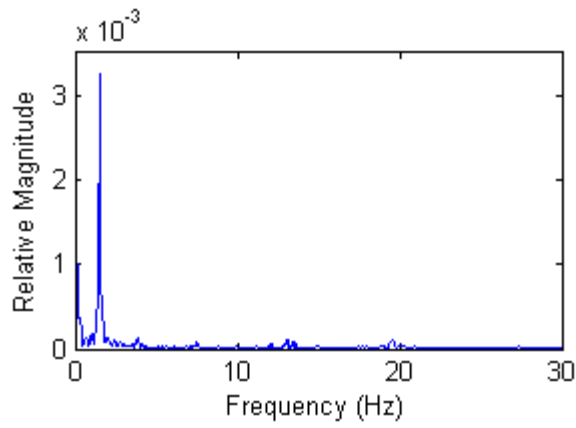


Figure 105. FFT analysis of NS accelerations with natural wind (near Mode 2 critical velocity)

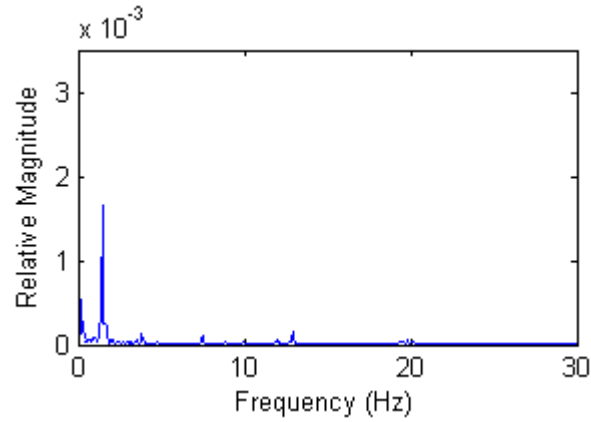


Figure 106. FFT analysis of EW accelerations with natural wind (near Mode 2 critical velocity)

Figure 107 shows another excerpt from the acceleration data collected near the Mode 2 critical velocity. These data were collected during and after the passing of a tractor-trailer truck. FFT analysis of the data (Figure 108, Figure 109) demonstrates that the higher-mode vibrations at 19.5 Hz (introduced by passing vehicles) are dominant despite the Mode 2 excitation resulting from vortex shedding. The first seven modes of the pole are excited by the combination of vortex shedding loading and traffic excitation.

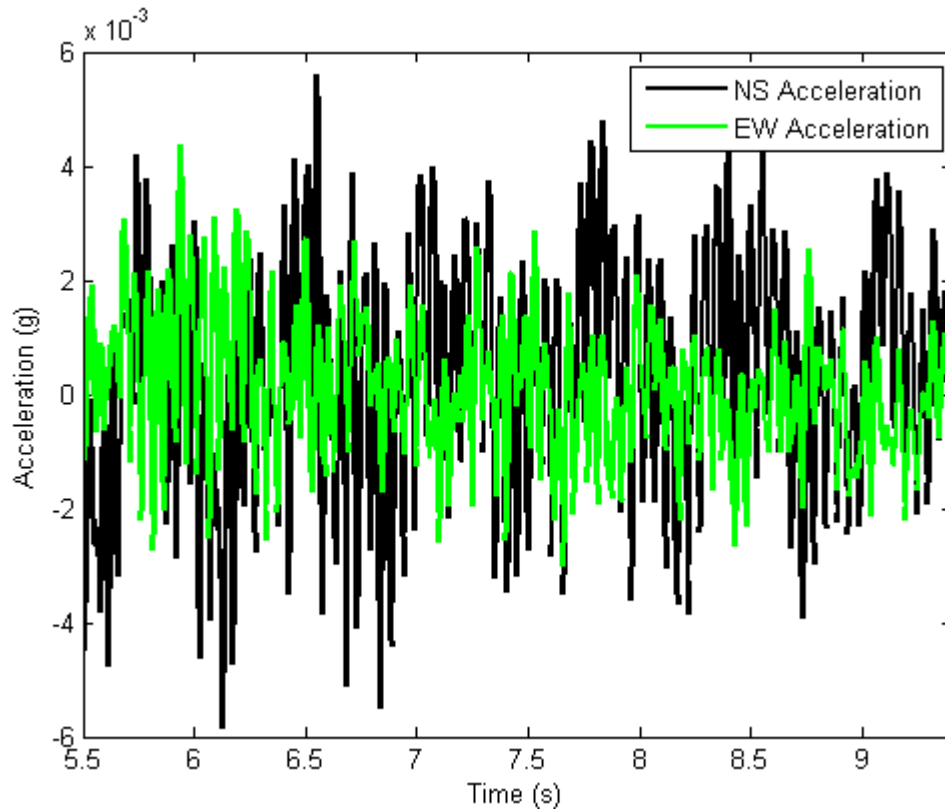


Figure 107. Acceleration vs. time with traffic excitation

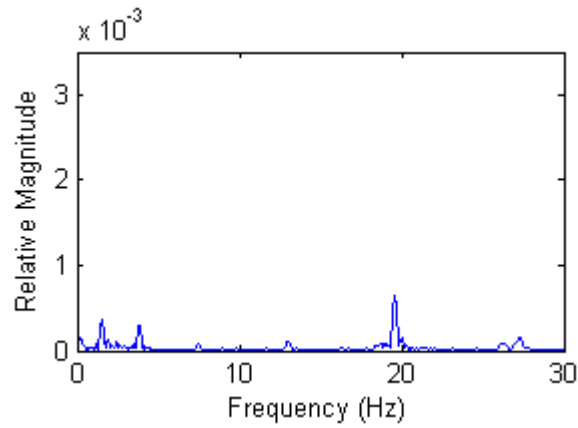


Figure 108. FFT analysis of NS accelerations with traffic excitation

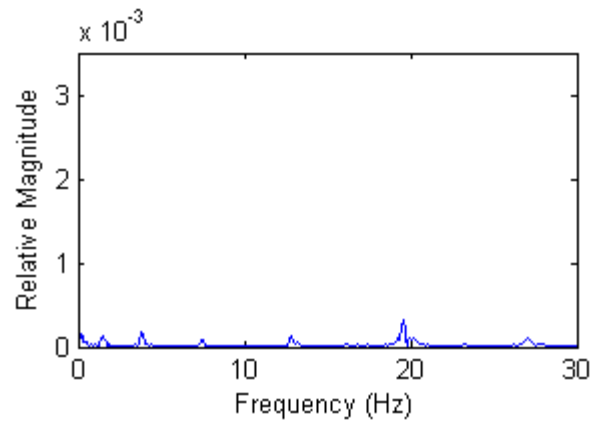


Figure 109. FFT analysis of EW accelerations with traffic excitation

6.3 Test 27 - Mode 3

Data were collected at a mean wind speed of 12.1 mph (Figure 110). FFT analyses of the data (Figure 111, Figure 112) show that Mode 3 is dominant in the north-south and east-west directions at a frequency of 3.8 Hz, but higher and lower frequencies are also present. Mode 3 vibrations are also evident in the FFT analysis of the vertical data (Figure 113), suggesting that the larger amplitude oscillations are flexing the pole and causing vertical motion at the base plate. (Note the difference in scale between the frequency spectra for the NS and EW direction and the vertical direction. The vertical accelerations are approximately two orders of magnitude smaller than those in the NS and EW directions.) There is virtually no higher frequency content in the vertical acceleration data, indicating that these vibrations are not the result of traffic excitation.

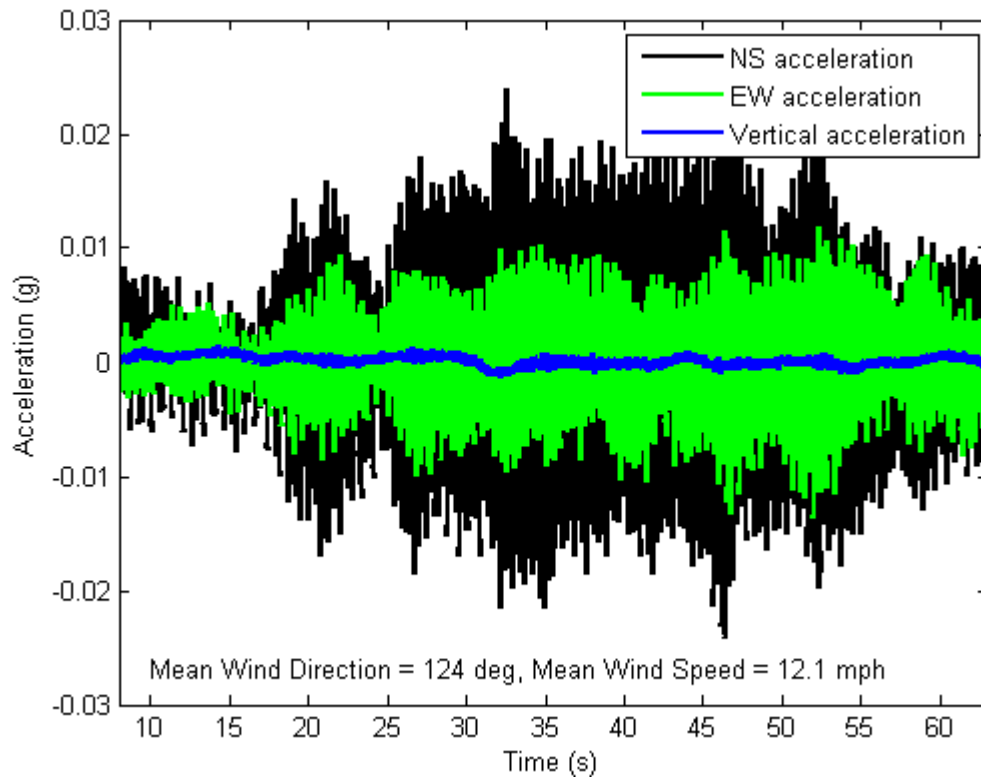


Figure 110. Acceleration vs. time at a mean wind speed of 12.1 mph

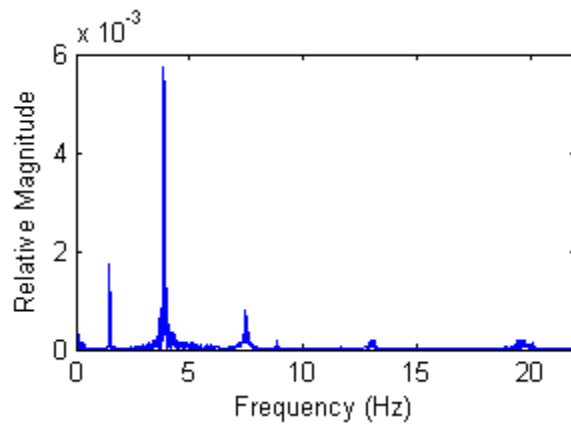


Figure 111. FFT amplitude spectrum for NS accelerations at a mean wind speed of 12.1 mph

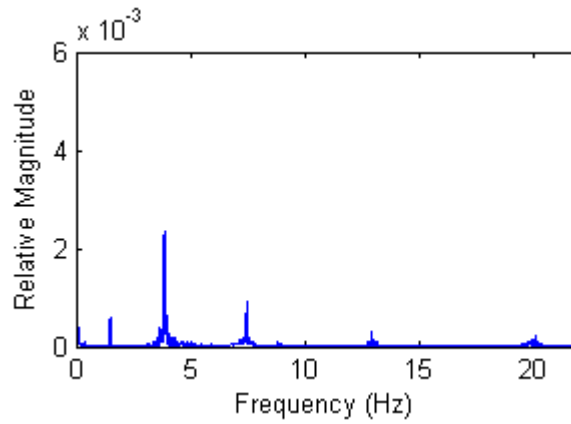


Figure 112. FFT amplitude spectrum for EW accelerations at a mean wind speed of 12.1 mph

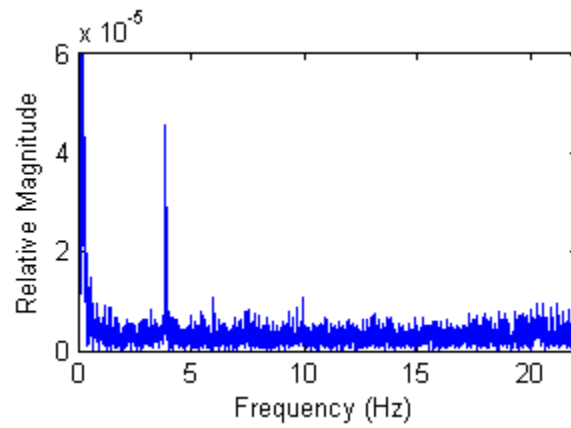


Figure 113. FFT amplitude spectrum for vertical accelerations at a mean wind speed of 12.1 mph

Mode 3 vortex shedding vibrations are clearly observed in the acceleration data, but higher frequency vibrations introduced by passing traffic break up the sinusoidal oscillations (Figure 114).

Closer inspection of acceleration data logged under natural wind loading only (Figure 115) shows the pole very close to Mode 3 lock-in (Figure 116, Figure 117).

Acceleration data logged under the same wind conditions but with additional traffic excitation (Figure 118) shows a reduction in the amplitude of accelerations when a vehicle passed. FFT analyses of the traffic excitation data (Figure 119, Figure 120) show that 3.8 Hz is still the dominant frequency, but even small amplitude vibrations at 19.5 Hz prevent the pole from resonating.

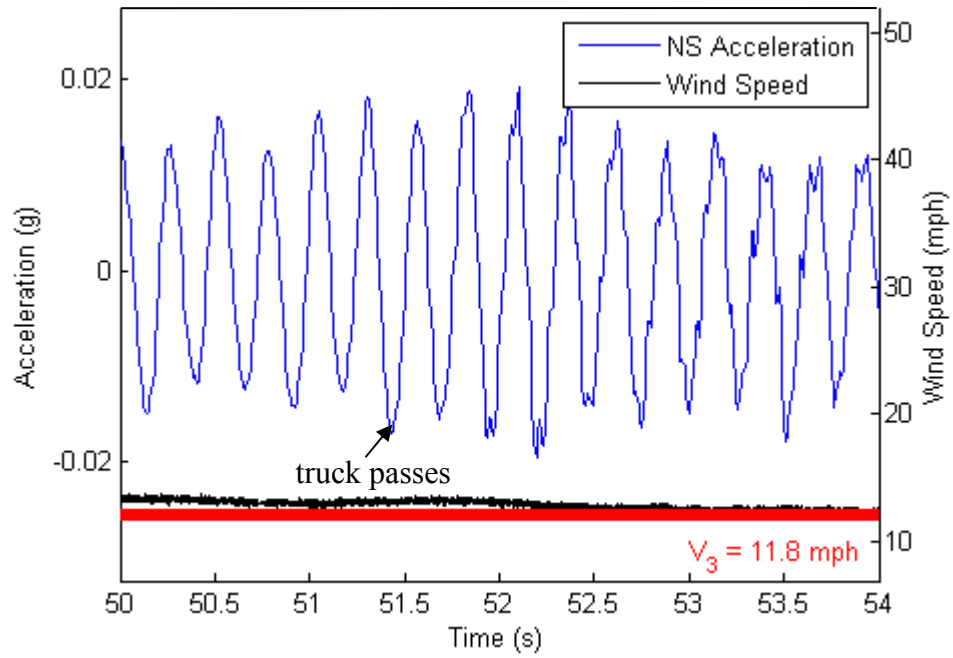


Figure 114. Acceleration vs. time at constant wind speed close to Mode 3 critical velocity

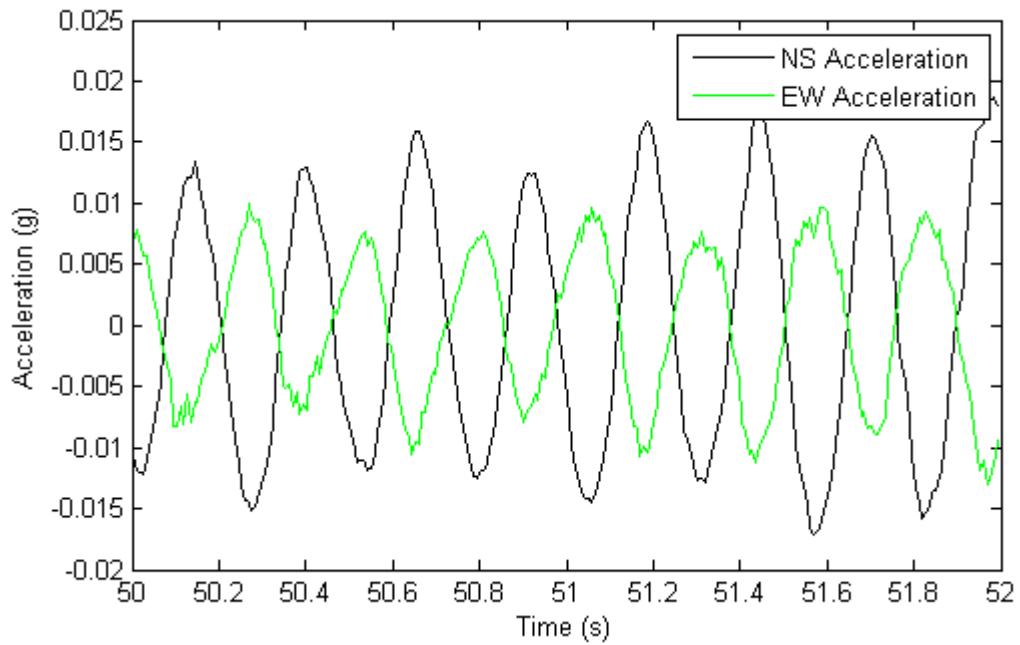


Figure 115. Acceleration vs. time with natural wind (near Mode 3 critical velocity)

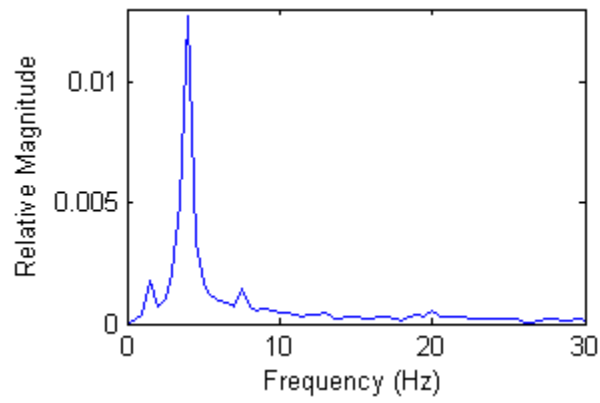


Figure 116. FFT analysis of NS accelerations with natural wind (near Mode 3 critical velocity)

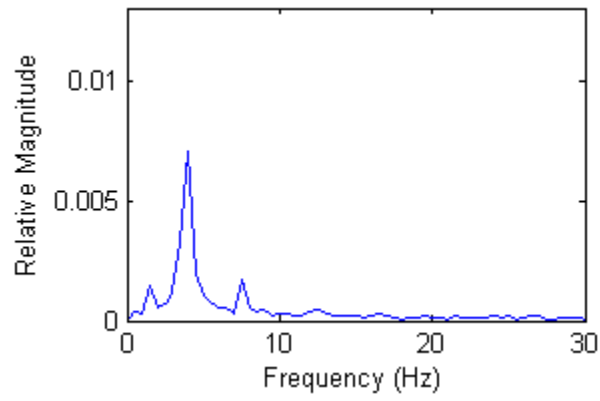


Figure 117. FFT analysis of EW accelerations with natural wind (near Mode 3 critical velocity)

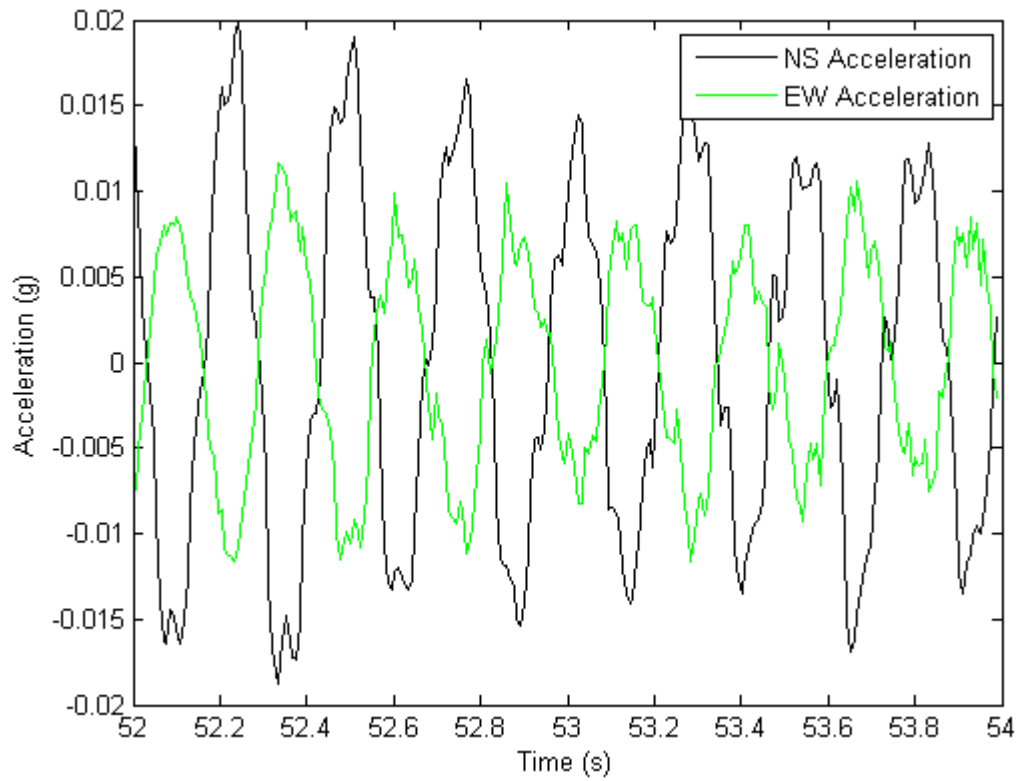


Figure 118. Acceleration vs. time with traffic excitation

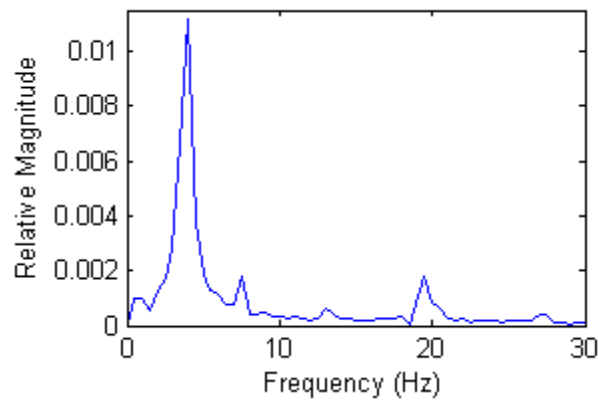


Figure 119. FFT analysis of NS accelerations with traffic excitation

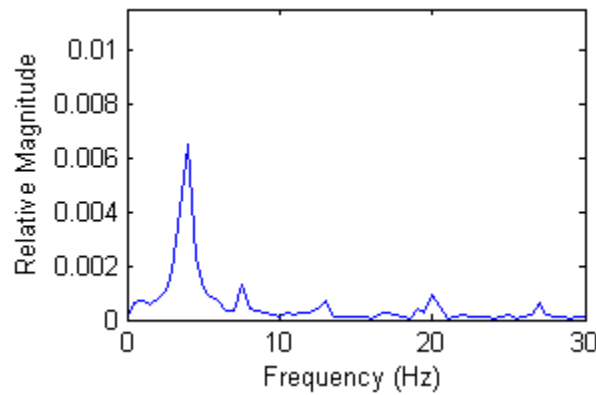


Figure 120. FFT analysis of EW accelerations with traffic excitation

6.4 Summary

The accelerations resulting from truck gusts alone measured by accelerometers located on the pole were observed to be quite small. The highest accelerations were approximately 0.006g and most were somewhat smaller. It appears, however, that these small perturbations are significant enough to prevent the amplified oscillations of lock-in from occurring. That is, when truck traffic is constant, lock-in is not allowed to occur for long enough for self-excitation to commence. Though vortex-shedding is still occurring at the pole, traffic vibrations prevent the pole from resonating. Lock-in is a very delicate process and it is easily disrupted by the introduction of relatively small oscillations at frequencies different from the modal frequency.

6.5 Test 29 - Lateral Ground Vibrations

Data were logged simultaneously using the north-south accelerometer on the pole and a second accelerometer mounted on a small concrete slab to detect lateral ground vibrations. Figure 121 shows 100s of data that contains two instances of large truck excitation at approximately 45s (Truck 1) and 83 s (Truck 2).

Further inspection of Truck 1 data shows ground excitation and pole excitation coinciding with one another (Figure 122). FFT analysis shows pole excitation (Figure 123) at 1.5 Hz (wind excitation) and 12.9, 19.5, and 26.4 Hz (traffic excitation). Ground excitation (Figure 124) is primarily in the 15 to 25 Hz range, with peaks at 17.9 and 24.2 Hz.

Truck 2 data are provided in Figure 125. FFT analysis of the Truck 2 pole data (Figure 126) reveals dominant frequencies similar to those found in the Truck 1 pole data. However, the ground data under Truck 2 excitation has no discernible frequency content (Figure 127). This indicates that while a truck induced a 0.006g acceleration in the pole, no significant ground vibrations were present, suggesting that the pole excitation was due to airborne traffic vibrations and not a result of waves propagating through the ground.

Vehicle ground vibrations are largely a function of the load being carried by the vehicle. Airborne vibrations, however, are a function of the size and shape of the vehicle. Therefore, two similar trucks could displace approximately the same amount of air causing similar gusts that excite the pole, but if one is carrying a heavy load and the other is empty (or carrying a light

load) the ground vibrations they cause could be significantly different. This is a possible explanation for the difference between Figure 124 and Figure 127. It also suggests that truck gusts, and not ground vibrations, are critical for pole excitation.

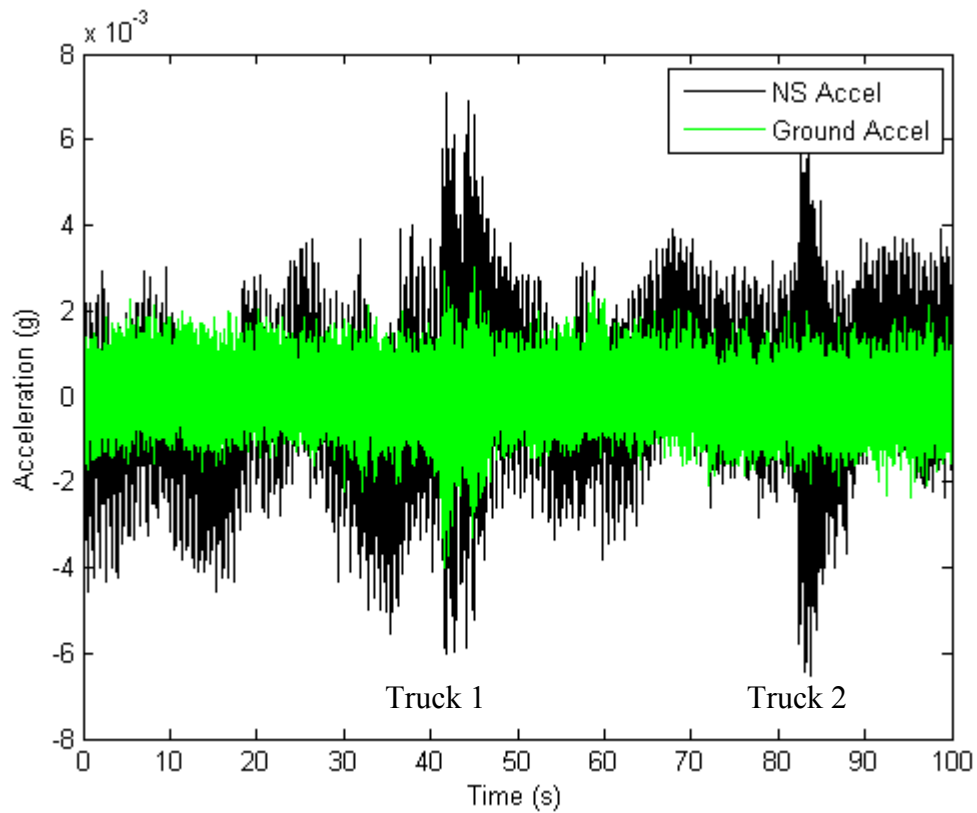


Figure 121. Acceleration vs. time

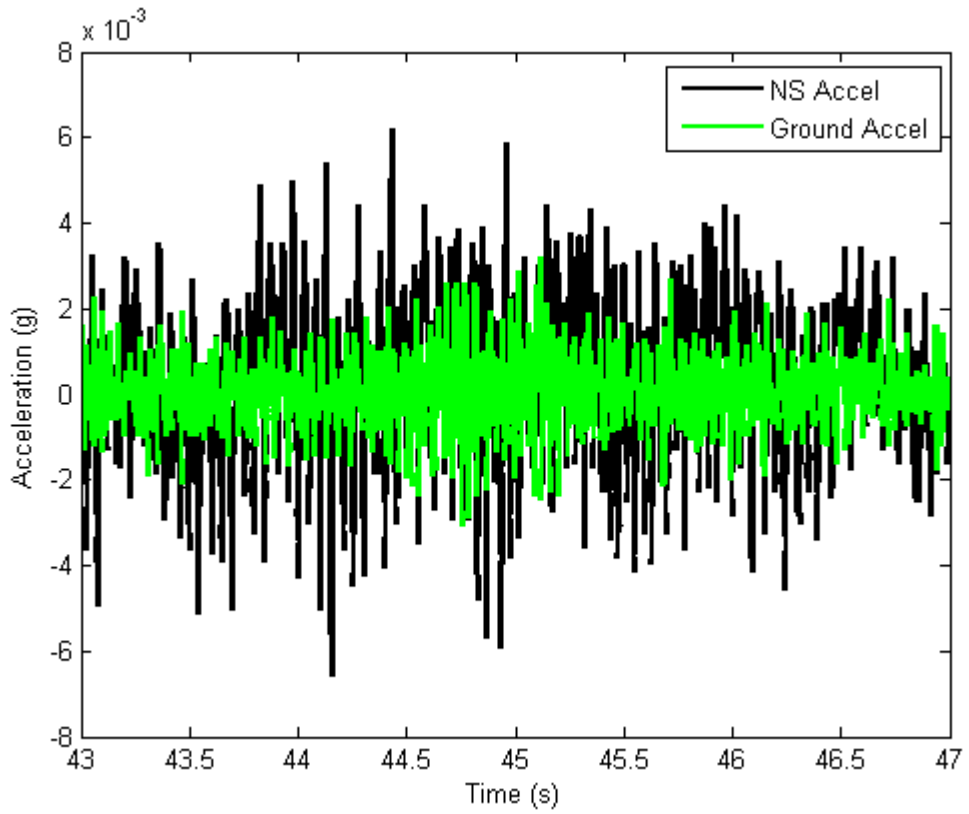


Figure 122. Acceleration vs. time (Truck 1)

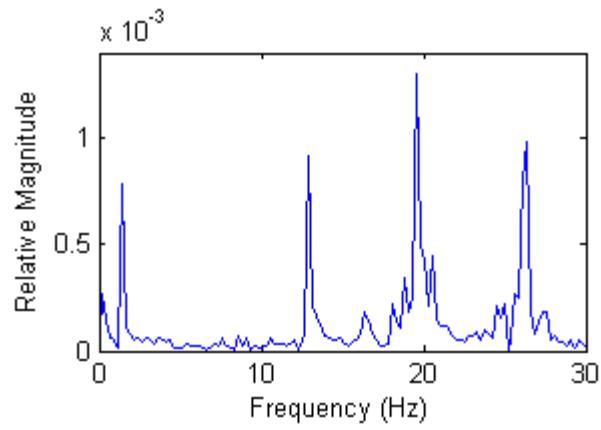


Figure 123. FFT analysis of NS accelerations (Truck 1)

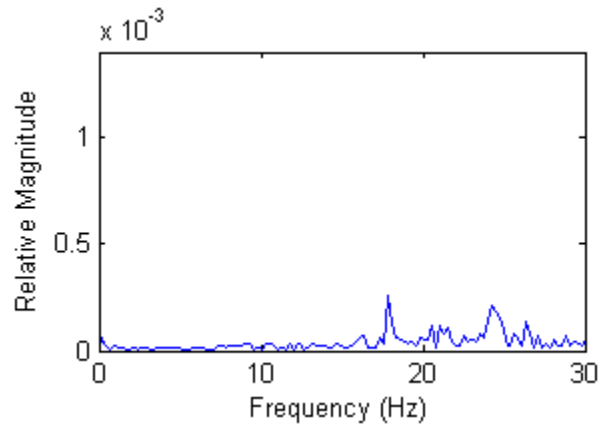


Figure 124. FFT analysis of ground accelerations (Truck 1)

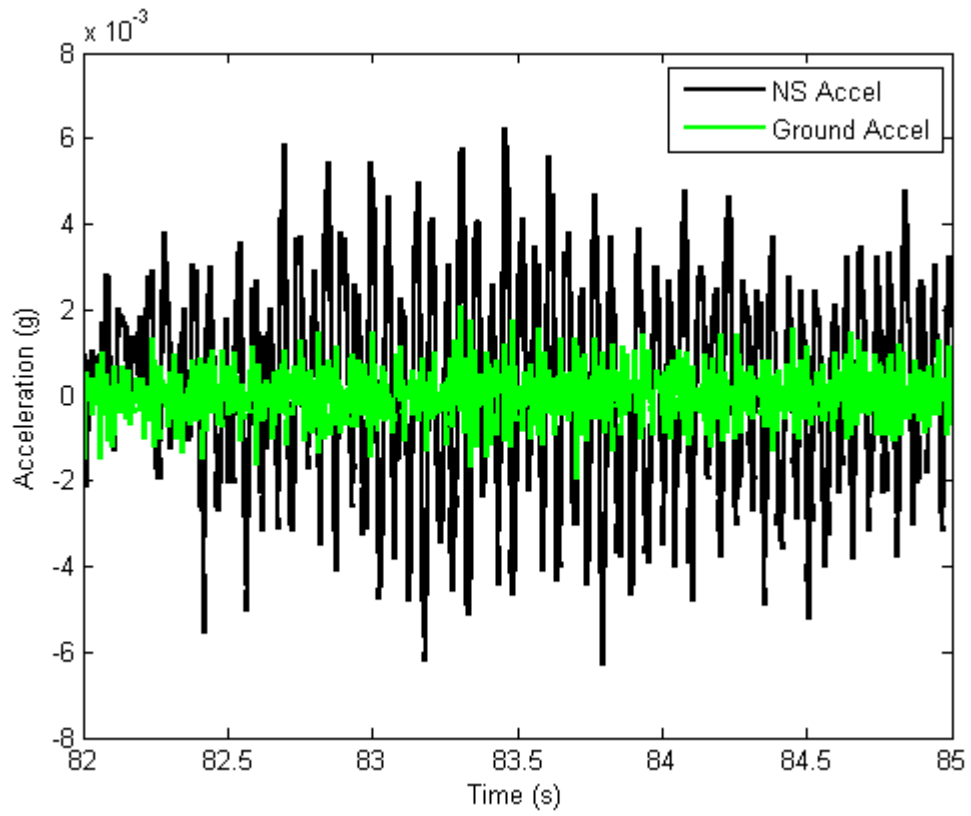


Figure 125. Acceleration vs. time (Truck 2)

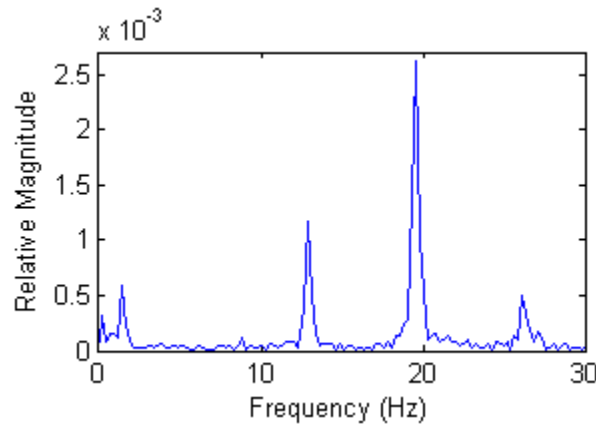


Figure 126. FFT analysis of NS accelerations (Truck 2)

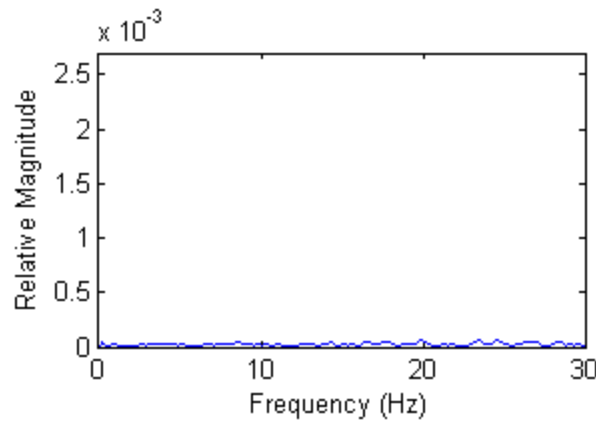


Figure 127. FFT analysis of ground accelerations (Truck 2)

6.6 Sensor Event Driven Trigger

A “Sensor Event Driven Trigger” (SEDT) was set on each of the MicroStrain G-Link nodes on Pole 4 to determine whether the structure ever achieves lock-in. A ceiling value of 0.15g was used on Channel 3 (north-south) of the upper accelerometer and Channel 2 (east-west) of the lower accelerometer. The ceiling value was chosen because lock-in accelerations on Pole 3 typically exceed 0.15g. The north-south and east-west directions were used because the wind direction varies.

In 14 weeks with the SEDT enabled, the nodes did not record a single instance of lock-in. A number of data sets were logged as the result of wind gusting, but none showed the pole locked in to a single mode of vibration.

7 CONCLUSIONS

7.1 Findings

The following conclusions can be made based on the research presented herein:

- Mode 3 is critical for the subject high-mast light poles and occurs at wind speeds between 10 and 19 mph.
- Damping ratios for the first three modes are all less than 0.5%.
- Constant wind direction is more critical than constant wind speed for the occurrence of lock-in.
- The pole's response is dependent upon more than just the instantaneous wind velocity or the mean 30s wind velocity. It is affected by the pole's complex interaction with the airflow and subtle fluctuations in the wind speed and direction which are beyond the scope of this project.
- When the pole is locked in to a given mode, it vibrates at the modal frequency in both the crosswind and alongwind direction.
- There is a correlation between acceleration and stress range for the subject pole. Where strain data are not available, the stress range (in ksi) at the base can be estimated by multiplying the peak acceleration at 56 ft (in g) by a factor of 7.3. According to this model, Mode 3 vibrations would cause the CAFL of 4.5 ksi to be reached when the acceleration at 56 ft was 0.6g and the maximum deflection (at 97 ft) was just 0.7 in.
- A 16-ft perforated shroud centered on the pole's upper antinode for Mode 3 (covering 13% of the structure) successfully eliminates vortex shedding that causes Mode 3 vibrations.
- It was observed that lock-in is a delicate process, and it is easily disrupted by the introduction of relatively small oscillations at frequencies different from the modal frequency. Small vibrations ($< 0.005g$) at frequencies different from the vortex shedding frequency prevented lock-in from occurring in Pole 4.
- The pole's response due to traffic vibrations has the greatest magnitude and longest duration transverse to the vehicles' direction of travel.
- No wind speed was recorded in association with traffic vibrations. Vibrations can be attributed to eddies caused by the vehicle displacing a large volume of air, as well as engine and road noise.
- The pole's response was affected by vehicles travelling in the westbound lane (adjacent to the structure) as well as the eastbound lane.
- Traffic vibrations propagating through the air and not the ground were observed to excite the high-mast pole.

7.2 Suggested future work

Based on the above results, the following recommendations are made:

- Further investigation is recommended to test the perforated shroud continuously in a larger range of wind speeds and to develop a shroud design that is compatible with the lowering device.
- Because surface roughness potentially offers such a simple and elegant solution to the problem of vortex-induced vibration, further research is recommended to determine the amount of roughness required to eliminate vortex shedding.
- Additional research is suggested to determine whether the incidence of cracking is higher for poles away from highways than it is for poles located near busy, high-speed roadways.

8 REFERENCES

- Achenbach, E., & Heinecke, E. (1981). On vortex shedding from smooth and rough cylinders in the range of Reynolds numbers 6,000 to 5,000,000. *J. Fluid Mech.* , 239-251.
- American Association of State Highway and Transportation Officials. (2009). *Standard Specifications for Structural Supports for Highway Signs, Luminaires, and Traffic Signals, Fifth Edition*. Washington, D.C.
- Blevins, R. D. (1990). *Flow-Induced Vibration*. New York: Van Nostrand Reinhold.
- Chakroun, W., Rahman, A. A., & Quadri, M. (1997). The Effect of Surface Roughness on Flow Around a Circular Cylinder. *Wind Engineering* , 1-12.
- Chang, B. (2009). Personal communication.
- Chang, B., Phares, B. M., Sarkar, P. P., & Wipf, T. J. (2009). Development of a procedure for fatigue design of slender support structures subjected to wind induced vibration. *TRB 2009 Annual Meeting CD-ROM*.
- Dexter, R. J., & Ricker, P. E. (2002). *NCHRP Report 469: Fatigue-Resistant Design of Cantilevered Signal, Sign, and Light Supports*. Washington, D.C.: National Academy Press.
- Durgesh, V. a. (2006). Detailed Experimental Investigation of the Base Drag Reduction Phenomena on a Wedge Model. *3rd AIAA Flow Control Conference*. San Francisco, CA: American Institute of Aeronautics and Astronautics, Inc.
- Fredrick, G. (2009). Personal communication.
- Goode, J. S., & van de Lindt, J. W. (2007). Development of a Semiprescriptive Selection Procedure for Reliability-Based Fatigue Design of High-Mast Lighting Structural Supports. *Journal of Performance of Constructed Facilities* , 193-206.
- Hao, H., Ang, T., & Shen, J. (2001). Building vibration to traffic-induced ground motion. *Building and Environment* , 321-336.
- Holmes, J. D. (n.d.). *Towers, chimneys, and masts*. Retrieved March 19, 2010, from Louisiana State University: www.hurricaneengineering.lsu.edu/CourseMat/03Lect21Towers.ppt
- Holmes, J. D. (2001). *Wind Loading of Structures*. London: Spon Press.
- Hunaidi, O. (2000, June 1). *Traffic Vibrations in Buildings*. Retrieved September 3, 2009, from National Research Council Canada: <http://www.nrc-cnrc.gc.ca/eng/ibp/irc/ctus/ctus-n39.html>
- Kumar, R. A., Sohn, C.-H., & Gowda, B. H. (2008). Passive Control of Vortex-Induced Vibrations: An Overview. *Recent Patents on Mechanical Engineering* , 1-11.
- Kwon, S., Cho, J., Park, J., & Choi, H. (2002). The effects of drag reduction by ribbons attached to cylindrical pipes. *Ocean Engineering* , 1945-1958.
- Lienhard, J. H. (1966). Synopsis of Lift, Drag and Vortex Frequency Data for Rigid Circular Cylinders. *Washington State University, College of Engineering, Research Division Bulletin 300* .
- Lombaert, G., Degrande, G., & Clouteau, D. (2000). Numerical modelling of free field traffic-induced vibrations. *Soil Dynamics and Earthquake Engineering* , 473-488.

- Minimum Design Loads for Buildings and Other Structures*. (2005). Reston, VA: American Society of Civil Engineers.
- Naughton, J. (2009). Personal communication.
- Pagnini, L. C., & Solari, G. (2001). Damping measurements of steel poles and tubular towers. *Engineering Structures* , 1085-1095.
- Parish, T. R. (2009). Personal communication.
- Parsons Brinckerhoff in association with PB Consult. (2008). *Interstate 80 Tolling Feasibility Study*. Wyoming Department of Transportation.
- Phares, B. M., Sarkar, P. P., Wipf, T. J., & Chang, B. (2007). *Development of Fatigue Design Procedures for Slender, Tapered Support Structures for Highway Signs, Luminaries, and Traffic Signals Subjected to Wind-Induced Excitation from Vortex-Shedding and Buffeting*. Ames, IA.
- Pierre, J. W. (2009). Prony Method Lecture Notes.
- Reid, S. (2008). *Wind Actions and Responses of Steel Chimneys*. Retrieved February 3, 2009, from Industrial Environmental Systems, Inc.: http://www.iesysinc.com/index.php?pr=Technical_Papers
- Simiu, E., & Scanlon, R. H. (1986). *Wind Effects on Structures*. New York: John Wiley & Sons.
- Van Dyke, M. (1982). *An Album of Fluid Motion*. Stanford, CA: Parabolic Press, Inc.
- Wyoming Department of Transportation. (1997). High Mast Lighting Standard Details.